A Multi-Wavelength Perspective of Flares on HR 1099: Four Years of Coordinated Campaigns

Rachel A. Osten[1]

National Radio Astronomy Observatory, Charlottesville, VA 22903

Alexander Brown, Thomas R. Ayres

Center for Astrophysics and Space Astronomy, University of Colorado, Boulder, CO 80309-0389

Stephen A. Drake

HEASARC, NASA/GSFC, Greenbelt, MD 20771

Elena Franciosini, Roberto Pallavicini

INAF/Osservatorio Astronomico di Palermo
Italy

Gianpiero Tagliaferri

INAF/Osservatorio Astronomico di Brera
Italy

Ron T. Stewart

Australia Telescope National Facility, Retired
Australia

Stephen L. Skinner

Center for Astrophysics and Space Astronomy, University of Colorado, Boulder, CO 80309-0389

Jeffrey L. Linsky

JILA, University of Colorado & NIST, Boulder, CO 80309-0440

ABSTRACT

[1]Jansky Fellow, National Radio Astronomy Observatory

We report on four years of multiple wavelength observations of the RS CVn system V711 Tau (HR 1099) from 1993, 1994, 1996 and 1998. This combination of radio, ultraviolet (UV), extreme ultraviolet (EUV), and X-ray observations allows us to view, in the most comprehensive manner currently possible, the coronal and upper atmospheric variability of this active binary system. We report on the changing activity state of the system as recorded in the EUV and radio across the four years of observations, and study the high energy variability using an assemblage of X-ray telescopes. We find:
(1) evidence for coherent emission at low radio frequencies ($\leq$ 3 GHz) which appears to be both highly time variable and persistent for several hours. Such phenomena are relatively common, occurring $\approx$ 30% of the time HR 1099 was observed at L-band. The measured polarizations of these bursts are left circularly polarized, in contrast with behavior at higher frequencies which has the opposite helicity. The polarizations are consistent with a variable source that is 100% left circularly polarized, along with a steady level of flux and polarization which is 0 or slightly right circularly polarized. There appears to be a low degree of correlation between bursts at 20 cm and higher frequency gyrosynchrotron flares, and also between 20 cm bursts and large EUV/soft X-ray (SXR) outbursts.
(2) Higher frequency (5–8 GHz) flares show an inverse relationship between flux and polarization levels as the flare evolves; this behavior is consistent with flare emission which is initially unpolarized. Large variations in spectral index are observed, suggesting changes in optical depths of the flaring plasma as the burst progresses. Quiescent polarization spectra show an increase of polarization with frequency, a pattern typically seen in active binary systems but still not understood.
(3) EUV observations reveal several large flares, in addition to numerous smaller enhancements. The total range of variability as gleaned from light curve variations is only a factor of 7, however. Observations in different years provide evidence of a change in the quiescent, not obviously flaring, luminosity, by a factor of up to 2. From an analysis of time-resolved spectral variations, we are able to infer evidence for the creation of high-temperature plasma during flare intervals compared with quiescent intervals. Interpretation of EUV spectral variations is hindered by the lack of ability to diagnose continuum levels and activity-related abundance changes, which are known from higher energy observations. Electron densities determined by line ratios of density-sensitive emission lines are high (10^{12}–10^{13} cm^{-3}) and there is no evidence for large density enhancements during flare intervals, compared with quiescent intervals.

(4) X-ray observations reveal several flares, and provide evidence of energy-dependent flare evolution: harder X-ray energies show faster temporal evolution than at softer energies. Time-resolved X-ray spectral analysis shows the presence of hot plasma, $T_e \sim 30$ MK, during flares compared to quiescent intervals, as well as evidence for changing abundances during flares. The abundance of iron (which is subsolar) shows an enhancement of a factor of three at the peak of a moderate flare seen by *ASCA* relative to the pre-flare level; abundances decrease during the flare decay. No hard (> 15 keV) emission is detected by either *RXTE* or *BeppoSAX*.
(5) The luminosity ratios L_{EUV}/L_R in quiescence determined from several time intervals during the four campaigns are consistent with previously determined ratios from a sample of active stars and solar flares. The range of L_{EUV}/L_R from three EUV/radio (3.6 cm) flares is the same as the values obtained during quiescence, which points to a common mechanism for producing both flaring and not flaring emission.
(6) Seventeen flares were observed in the EUV and/or SXR during the four campaigns; of the eight flares that had radio coverage, three show 3.6 cm radio flares, which are generally consistent with the Neupert effect. Five EUV/SXR flares had partial UV coverage; all show UV responses, particularly in the C IV transition. The UV flare enhancements can occur at the same time as the 3.6 cm radio flares, in two cases where radio, UV, and EUV/SXR flare coverage overlapped.
(7) For SXR flares, we find that the contrast between flare emission and quiescent emission increases as expected towards higher energies, making flare detections easier at harder X-ray energies. This is due to the creation of high temperature plasma during flares, which shows up predominantly in high energy continuum emission. We find a discrepancy between the implied flaring rate based on EUV observations, and higher energy observations; the lower energies tend to miss many of the flares, due to the lack of sufficient contrast with quiescent emission.

Subject headings: stars: activity — stars: coronae — stars: late-type — radio continuum: stars — X-rays: stars

1. Introduction

As a bright and variable system in almost all wavelength regions, HR 1099 (V711 Tau; HD 22468) has been the subject of many past observations from radio to X-ray wavelengths. HR 1099 is a short-period (P_{orb} = 2.83774 d) binary composed of a G5 dwarf and a K1 subgiant. The system lies at a Hipparcos distance of 29 pc (Perryman et al. 1997). The orbital and rotational periods of the stars are tidally synchronized. The mass ratio is 1.3, yet the K subgiant outsizes the G subgiant by a factor of three in radius. The orbital inclination is $\approx 33°$ (Strassmeier et al. 1993, and references therein) and there are no eclipses. Because of its spectroscopic characteristics and highly active chromospheric, transition region, and coronal emissions, HR 1099 is a member of the RS CVn class of binary systems. Many of the phenomena seen on RS CVn systems have solar counterparts, and invite the comparison between "hyper-active" stars such as these and less active stars like the Sun.

A schematic of the generally accepted model for solar flares proceeds as follows: A flare begins with a source of free energy, thought to originate from magnetic reconnection high in the solar corona. Some of this energy is used to accelerate electrons to moderately relativistic speeds. Electron beams can be generated, and propagate outward or into the atmosphere; the electron beams emit plasma radiation (type III bursts), whose frequencies trace the ambient plasma density the beams encounter as they propagate either outward or into the atmosphere (Aschwanden & Benz 1997). Downward-directed accelerated electrons can become magnetically trapped in the coronal loop or arcade, and emit gyrosynchrotron emission at microwave frequencies. As the electrons impact the denser regions of the lower atmosphere, they deposit their energy, emitting hard X-rays via nonthermal bremsstrahlung emission and white light continuum emission at the footpoints of the loops. The energy deposited by the electrons in the lower atmosphere heats plasma to coronal temperatures on a timescale short compared to the hydrodynamic expansion time, ablating material at 10^6–10^7 K up the coronal loops, where it emits soft X-ray radiation. As the coronal density increases coronal material can stop the energetic electrons higher up in the atmosphere thereby heating the corona directly. Once the nonthermal energy input has ceased, the material in the loop condenses into the chromosphere and the soft X-ray emission returns to its preflare state. This scenario implies a set of related and correlated variations that should be observable in different spectral regions.

Despite the relatively advanced state of understanding of multi-wavelength solar flare emissions, there is a paucity of observations on the stellar side. Part of this may result from the difficulties inherent in organizing such an observing campaign for stellar flares; but the potential benefits to understanding stellar flares must surely outweigh the enormous effort needed to coordinate such observations. Güdel & Benz (1993) showed that there existed an almost linear relationship between stellar quiescent radio and soft X-ray emission, suggesting that coronal heating and particle acceleration are closely linked in a way that may be similar to solar flares. In one of the earliest studies of multi-wavelength emission, Weiler et al. (1978) examined optical, UV, and radio observations of two RS CVn systems (one of them HR 1099) and said "there are suggestive coincidences between peak radio flux density and optical-UV emission activity from both systems." Other studies of multi-wavelength stellar flares have revealed a zoo of phenomena, leading to split opinions as to whether such correlations even exist. In one of the earliest simultaneous studies, Kundu et al. (1988) examined radio and X-ray observations of four flare stars. While they noted some X-ray bursts coincided in time or were preceded by 10–15 minutes by 20 cm radio flares, they still claimed the degree of correlation was low. Fox et al. (1994) observed the decay of a radio flare on the RS CVn system EI Eri but did not see an accompanying X-ray or EUV flare. Yet Stern et al. (1992) found UV and microwave flaring occuring during an X-ray outburst on the RS CVn system σ^2 CrB. Gagne et al. (1998) investigated the M dwarf binary system EQ Peg with radio, optical, EUV and X-ray wavelengths and found two populations of X-band (3.6 cm) flares: highly polarized flares with no counterparts at shorter wavelengths, and moderately polarized flares which do have shorter wavelength counterparts. Recently, Osten et al. (2000) established a correlation of radio flares with X-ray flares on σ^2 CrB, with X-ray flares peaking up to 1.4 hours before the radio peak. And most recently, Ayres et al. (2001a) conducted coordinated UV, EUV, X-ray and radio observations on HR 1099 and detected a large UV flare not seen in higher energy emissions.

The flare mechanism is a poorly understood phenomenon, even when considered in a single wavelength region (or on a very well-studied star like the Sun). Expectations that stellar flares mimic the behavior of solar flares can introduce biases into the interpretation of multi-wavelength studies. Also, it is necessary to recognize the importance of time delays between different wavelength regions when studying flares in a multi-wavelength context and the necessity of long exposure times to catch and observe flares in their entirety.

This paper describes the results of four campaigns which observed HR 1099 in multiple wavelength regions, in 1993, 1994, 1996, and 1998. A summary of these campaigns is given in Table 1. Section 2 summarizes previous observations of HR 1099; section 3 describes the observations and initital data reduction; Section 4 examines the wavelength regions individually across the time span of these four campaigns; § 5 investigates comparisons between the different wavelength regions investigated; and § 6 concludes.

2. Previous Studies

Much is known about the starspot distribution on HR 1099: The subgiant primary of HR 1099 is one of the brightest stars to show evidence for spots in its photosphere, and has been the subject of numerous photometric and Doppler imaging campaigns since 1975. Vogt et al. (1999) presented a study of 11 years of Doppler images of the stellar surface that display the long term stability of a cool polar spot and lower latitude spots that vary on less than one year timescales. The polar spot, together with a low degree of shearing and nearly solid body rotation of the other spots detected, led Vogt et al. to suggest the presence of a global multi-kilogauss dipolar magnetic field on the star. Donati et al. (1990) used the technique of Zeeman Doppler imaging to detect magnetic features, and deduced magnetic fields whose average strength was 985 G covering 8% of the total stellar surface. A longer term study of magnetic features by Donati (1999) found that a significant fraction of the magnetic flux comes from regions at photospheric temperatures; i.e., there was no spatial correlation between brightness and magnetic inhomogeneities. They determined variations in the orbital period with a period of 18 years, and deduced a magnetic activity cycle period of $\geq$ 12 years from a lack of polarity reversal during their 6 years of observations.

Other attempts to determine cycle periods from photometry have indicated similarly long timescales: Henry et al. (1995) from 18 years of photometry determined two periodicities in the mean V magnitudes from their spot solutions of 5.5 and 16 years. Oláh et al. (2000) used 22 years of monitoring and found a cycle period of 16.5 years along with a secondary period of 3.5 years. This second period is in agreement with Vogt et al. (1999)'s finding of a weak periodicity in the area of the polar spot of about 3 years. While there is a consensus that long-term cyclic behavior is at work on HR 1099, the lack of consensus on a timescale for this periodicity hampers any attempt to place our observations in the context of an activity trend.

Linsky et al. (1989) reported on *International Ultraviolet Explorer (IUE)* observations of a flare on HR 1099 in 1981, in which the Mg II k line profile displayed a broad component of 66 km s^{-1} and was redshifted by 90$\pm$30 km s^{-1}. The electron density at 10^4 K was a factor of 15 larger during the peak of the flare than in the quiescence preceding the flare. Wood et al. (1996) made an association between broad wings in ultraviolet (UV) emission lines as seen by the *Goddard High-Resolution Spectrograph (GHRS)* and micro-flaring in the chromosphere and transition region of HR 1099. Busà et al. (1999) used *IUE* observations from 1992 to investigate velocity variations in the Mg II h line which they attributed to emission from a localized region in the stellar chromosphere of the primary. In coordinated *IUE* and *GHRS* observations in 1993, Dempsey et al. (1996) saw several flare enhancements in UV line emission; one such enhancement lasted more than 24 hours as seen with *IUE*.

Barstow (1985) discussed a pointed EXOSAT observation of HR 1099 in 1981, in which a small flare with factor of two enhancement occurred. The light curve also displayed smaller amplitude variability on timescales of 500–1000 seconds, which van den Oord & Barstow (1988) explained as evidence of flare-like heating in the corona of HR 1099. From spectral fits to the data, Pasquini et al. (1989) found evidence for coronal temperatures of 3 and 25 MK. Drake et al. (1994) saw modulation in the light curve of *Extreme Ultraviolet Explorer (EUVE)* observations at the level of 40%, which they attributed to rotational modulation of a starspot. Contemporaneous optical photometry showed a light minimum which leads the extreme ultraviolet (EUV) maximum by 90 degrees in phase.

Feldman et al. (1978) presented radio data featuring several large flares on HR 1099 in 1978 with flux densities reaching up to 1 Jy at 10.5 GHz. Lestrade et al. (1984) performed 8.4 GHz Very Long Baseline Interferometry (VLBI) observations and found radio emission from a source comparable in size to that between the surfaces of the two stars in the binary system (0.9 mas) during a large radio outburst of 400 mJy. Jones et al. (1996) modeled Very Large Array (VLA) and Australia Telescope Compact Array (ATCA) quiescent observations and determined from gyrosynchrotron model fits that a highly organized magnetic field was necessary to explain the data. Trigilio et al. (1993) reported on VLBI 5 GHz observations during a large flare whose source size increased to a size comparable to the entire binary system. Umana et al. (1995) report the results of a radio monitoring campaign at 5 GHz from 1990–1993 which detected several large flares with flux densities of up to 800 mJy. Trigilio et al. (2000) performed a 5 GHz European VLBI Network (EVN) observation of HR 1099 simultaneously with our observing campaign in 1998. They found an overall size of the radio source, during quiescence, comparable to the angular diameter of the active K star and thus much smaller than the active period radio source previously observed by Trigilio et al. (1993). More recently, Richards et al. (2003) presented results from five years of radio monitoring at 2.3 and 8 GHz with the Green Bank Interferometer, and found periodicities of flaring cycles at ~ 120 days, and a weaker period of ~ 81 days, with 8.3 GHz flare fluxes reaching a peak of 1.44 Jy. In a related note, Schmitt et al (2003) now have succeeded in spatially resolving an X-ray limb flare on the magnetically active star in Algol, so we may soon see the first image of a flare on HR 1099.

Finally, quiescent and flaring X-ray emission from HR 1099 has been recently observed with *Chandra* and *XMM-Newton* (Brinkman et al. 2001; Audard et al. 2001; Drake et al. 2001; Ayres et al. 2001a; Ness et al. 2002; Audard et al. 2003) with emphasis on high-resolution grating spectroscopy (see § 4.4.1 for a discussion).

3. Observations and Data Reduction

Since the nature of this study is to investigate both short- and long-term variability in this active binary system, the number of individual observations that comprise the whole study is large and spans many years. Such a collaborative effort involves numerous people, and several papers have been written analyzing individual datasets within this large study. The current investigation does present a reanalysis of several datasets which have been considered by others. Papers and conference proceedings describing the radio datasets are: Jones et al. (1996); Brown et al. (1994, 1996, 1997, 1998). For the radio datasets, the 1993 and 1994 data (previously published in Jones et al. 1996; Brown et al. 1994) are reanalyzed along with the 1996 (presented only at conferences) and 1998 datasets for a uniform and consistent analysis. The UV data has been discussed in Dempsey et al. (1996); Brown et al. (1994, 1996), and is presented here for multi-wavelength comparisons. The *EUVE* data (lightcurves and spectra) have been discussed in a number of papers, including: Osten & Brown (1999); Griffiths & Jordan (1998); Sanz-Forcada et al. (2002). The context of the *EUVE* analysis in the present paper is to examine the light curve and spectral variability on a flare-to-flare basis, which was not the focus of previous investigations. Preliminary analysis of the various X-ray datasets has been provided in Brown et al. (1996); Brown & Skinner (1996); Brown et al. (1994, 1997, 1998); Pallavicini (2001). The current analysis of the X-ray datasets is a detailed examination of both spectral and light curve changes. We discuss the observations in order of decreasing wavelength. A summary of all the observations appears in Table 1.

3.1. *VLA* Observations

HR 1099 was observed with the NRAO[2] VLA[3] radio array for all four of the campaigns. The observations were performed in two subarrays, in order to obtain simultaneous multi-frequency observations. Typically one subarray observed at 3.6 cm, while the other switched between 6 and 20 cm. Sparse coverage at 2 cm was included to extend frequency coverage for spectral index determinations, but only general information on activity levels at 2 cm can be gleaned. The flux calibrator for all frequencies for all VLA observations was 0137+331, with a flux density of 1.81 Jy at 2 cm, 3.29 Jy at 3.6 cm, 5.52 Jy at 6 cm, and 15.97 Jy at 20 cm. The phase calibrator for all frequencies for all the VLA observations was 0323+055,

[2]The National Radio Astronomy Observatory is a facility of the National Science Foundation operated under cooperative agreement by Associated Universities, Inc.

[3]For more information on the VLA, see http://www.vla.nrao.edu

with measured flux densities at 2 cm of 0.22 Jy, 3.6 cm of 0.43 Jy, 6 cm of 0.83 Jy, and 20 cm of 2.79 Jy. The 1993 VLA data were obtained at 3.6, 6, and 20 cm (8.41, 4.89, 1.46 GHz), while the remaining three years of observations were at 2, 3.6, 6, and 20 cm (14.96, 8.41, 4.89, 1.46 GHz). In 1993, the observations were taken in DnC array on September 13.6–18.4; with 45.8 hours of time on source at 3.6 and 6 cm. Observations at 20 cm were compromised due to radio frequency interference. The 1994 observations were obtained on August 25.3–28.6, in the B array. Time spent on source at 2, 3.6, 6, and 20 cm was 1.3, 30.1, 13.1, and 13.4 hours, respectively. During the 1996 campaign on September 2.3–7.7, the VLA was in D array; time spent on the source at 2, 3.6, 6, and 20 cm was 0.75, 48.9, 13.2, and 22.6 hours, respectively. The 1998 VLA observations were collected on September 7.3–11.7, in the B array. Time spent on the source at 2, 3.6, 6, and 20 cm was 1.7, 41, 16.9, and 18.5 hours, respectively. Data were calibrated and reduced using AIPS; light curve generation was performed using the DFTPL task.

3.2. *ATCA* Observations

Observations using the ATCA[4] were obtained during all four years of the campaigns, in 1993, 1994, 1996, and 1998. The data comprise four wavelengths: 3.6, 6, 13, and 20 cm (8.64, 4.8, 2.378, and 1.38 GHz, respectively). In 1993, 1994, and 1996 the phase calibrator at all four frequencies was 0336-019; while in 1998 the phase calibrator for all four frequencies was 0323+055. The primary flux calibrator was 1934-638, with a flux density of 2.84 Jy at 3.6 cm, 5.83 Jy at 6 cm, 11.152 Jy at 13 cm, and 14.95 Jy at 20 cm. In 1993, 44 hours of data were collected on September 14.5–17.9. The 1994 observations were obtained on August 23.7–27.0, and 38 hours of data were collected. In 1996, ATCA observations spanned September 2.6–7.0 for a total of 63 hours on source. In 1998, 93 hours of data were collected on September 8.6–12.9 on the source. The description of the 1993 and 1994 datasets are given in Jones et al. (1996); the 1996 ATCA dataset was reduced similarly. The 1998 data was reduced and calibrated using MIRIAD, and light curve generation was performed using the *uvfit* task. The nominal flux density of 1934-638 was revised in 1994 August, and all observations prior to this time used a slightly different flux scale, which was changed to provide better agreement with flux scales used at the VLA. The changes are $< 10\%$, and we apply a multiplicative scaling to the ATCA light curves in 1993 to account for this.

---

[4]For more information on the ATCA, see http://www.atnf.csiro.au

3.3. *IUE* Observations

In 1993 and 1994, *IUE* (Boggess et al. 1978a,b) observed HR 1099 with multiple exposures. Spectra from 1150–1980 Å and 1900–3100 Å were collected (on 1993 September 16.4–19.2, and on 1994 August 23.5–28.7). The reduction is described more fully in Brown et al. (1994) and Dempsey et al. (1996).

3.4. *GHRS* Observations

Observations with the HST GHRS instrument (Brandt et al. 1994; Heap et al. 1995) occurred on 1993 September 15.0–19.7. They are comprised mostly of G160M and Echelle-B observations of the Ly α (1216 Å), Mg II h and k lines (2803 and 2795 Å, respectively), C IV (1548 and 1550 Å), and C III] 1909 Å and Si III] 1892 Å lines. These data have been reduced and analyzed by Dempsey et al. (1996); and further description of the observations can be found in that paper. We use the time variation of the extracted fluxes in § 5.

3.5. *EUVE* Observations

EUVE observations were obtained on 1993 September 16.4–21.6, 1994 August 24.0–28.0, 1996 September 1.5–11.1, and 1998 September 3.0–11.7. Total exposure times for the four observations were 135, 102, 250, and 226 ks, respectively. For more information on the *EUVE* satellite, see Malina & Bowyer (1991). The Lexan/boron filter on the Deep Survey/Spectrometer (DS/S) is sensitive over the range 80–150 Å. Initial reduction and processing were performed using the standard *EUVE* General Observer (EGO) software in IRAF[5]. Corrections were made for detector "primbsching" and dead time. The primbsch algorithm distributes telemetry equally to operating detectors to maximize scientific gain. Losses from primbsching can occur from observations of bright sources when there is a high background rate in any detector (Miller-Bagwell & Abbott 1995[6]). The 1998 observation suffered from extremely high background due to increased solar radiation as the Sun approached a maximum in its cycle. Good time intervals were generated based on filtering times of high background and large deadtime and primbsch corrections, and the exposure

[5]IRAF is distributed by the National Optical Astronomy Observatories, which is operated by the Association of Universities for Research in Astronomy, Inc., under contract to the National Science Foundation (USA).

[6]Also online at http://archive.stsci.edu/euve/data_product.html.

time for the spectrometer data were corrected for these effects by dividing by the correction factors.

Spectral extraction of the short wavelength (SW; 80–180 Å) and medium wavelength (MW; 180–380 Å) spectrometer data followed the procedures used in Osten et al. (2000) and references therein. There was no preset distinction between quiescent and flaring times based on flux levels. Rather, the attempt was made to investigate flares on an individual basis. Flares can have a range in peak luminosity, as is known from solar and other stellar studies (Kucera et al. 1987; Pallavicini et al. 1990), and the "quiescent" level can also vary, so a cut-off based on count rate or luminosity would miss the early and late stages of a flare, or miss a flare with a small enhancement above quiescence entirely. Light curves were examined and the beginning and ending of flares were identified based on a smooth increase to peak and smooth decrease from peak. This allows us to examine low-level flares as well as larger events, attempt to characterize them, and compare and contrast derived properties. This is more subjective that using a threshold, but allows for a more nuanced approach to studying coronal variability. We divided the observations into segments according to activity state. We then summed time segments to provide spectra with decent statistics while still being able to discriminate between times of varying activity.

In addition to performing the time-resolved spectroscopy, we used the segments from across the four years to build up spectra that represent a composite of the different activity states of the system. We also used DS/S pointed observations of the system in 1992 October and 1999 September to boost the signal to noise. We summed all the quiescent spectra to obtain a high-quality spectrum of quiescence. In the same way we summed all the flare spectra to obtain a high-quality composite spectrum of flaring. In this way we can determine gross differences between quiescence and flaring, and compare these to differences that may arise from flare to flare.

3.6. *ASCA* Observations

Advanced Satellite for Cosmology and Astrophysics (ASCA) observations of HR 1099 in 1994 August covered 0.9 days, with an exposure time of 37.7 ks. For more information on the *ASCA* satellite, refer to Tanaka et al. (1994). The SIS detectors are sensitive over the range 0.6–10 keV, while the GIS detectors are sensitive to energies 0.8–12 keV. The observations with the SIS detectors were performed in 1-CCD mode, while the GIS detectors were operated in PH mode.

The raw data were processed using the HEASOFT 5.0 software package, creating final output light curves and spectra. Standard screening was applied to the data. Source spectra were extracted using a circular extraction region around the star with radius 3.9' for SIS0, 3.3' for SIS1, 16.8' for GIS2, and 17' for GIS3, excluding off-chip areas on the SIS detectors. Blank-sky background spectra were obtained from the *ASCA* Guest Observer Facility and were matched to the values of the standard screening parameters adopted here. Light curves for all detectors showed the same features. A small flare occurred during the observation, so we extracted spectra in time slices corresponding to different levels of activity.

3.7. *RXTE* Observations

Observations with the *Rossi X-ray Timing Explorer (RXTE)* (see Bradt et al. 1990) were obtained on 1996 September 2.8–6.2 and 1998 September 7.6–11.2. The exposure times in 1996 and 1998 were 38 and 72 ks. The Proportional Counter Array (PCA) uses five identical Xe/methane multi-anode proportional counters to collect photons over the energy range 2–100 keV with peak effective area $\approx$ 7,000 cm^2 around 10 keV. Each Proportional Counter Unit (PCU) has six Xenon layers and one propane layer. Due to the soft nature of HR 1099 compared to more typical *RXTE* X-ray sources, the majority of photons were collected in the outer, most sensitive Xe layer. The energy resolution is $\sim$18% at 6 keV for the Xenon layer. We examined data from the PCA only; the High Energy X-ray Timing Experiment (HEXTE), sensitive from 20 – 250 keV, did not detect the source. Processing of the data was performed at the *RXTE* Guest Observer Facility (GOF), using standard FTOOLS (version 4.1) software. Only data collected during times of the satellite orbit when elevation of the target above the Earth's limb was $> 10°$ were used; data taken during South Atlantic Anomaly (SAA) passes (and for 30 minutes after passage) were discarded, due to the large increase in background during such time intervals. Screening also was performed based on contamination from magnetospheric/solar flare electrons, which also cause an increase in the background at low energies. The 1996 observations were performed with all five PCUs on; during the 1998 observation, PCUs number 3 and 4 turned off at different times. Science data taken with different numbers of PCUs must be analyzed separately. However, for the 1998 observation the amount of time operated in 3 PCU-mode was small compared to the time operated in 5 PCU-mode, so we restricted our analysis to the 5 PCU-mode observations. We also extracted light curves in the 2–5 keV and 5–12 keV energy ranges. Based on a two temperature MEKAL fit in XSPEC (Arnaud 1996) to the extracted 5 PCU spectrum we estimated an energy conversion factor (ECF) for the PCA using the model folded through the PCA response; the ECF was 3.02 10^{29} erg count^{-1} in 1996 and 3.27 10^{29} erg count^{-1} in 1998. The spectral sensitivity was not sufficient to justify extraction of pulse-height spectra for the flaring and quiescent intervals; since *RXTE* is primarily a timing instrument, we concentrate on the observed light curve.

3.8. *BeppoSAX* Observations

HR 1099 was observed with *BeppoSAX* in 1998 September, from day 6.9 to 10.0 (i.e. slightly more than one orbital period), using the LECS (0.1–10 keV), MECS (1.6–10 keV) and PDS (15–300 keV) detectors. For more information on the *BeppoSAX* satellite refer to Boella et al. (1997). The effective exposure times were 63, 131 and 122 ks in the LECS, MECS and PDS, respectively. The lower exposure times in the LECS are due to the instrument being operated only in Earth shadow, thus reducing its observing efficiency.

The LECS and MECS data analysis was based on the linearized and cleaned event files obtained from the *BeppoSAX* Science Data Center (SDC) on-line archive. Spectra and light curves were accumulated using the HEASOFT 5.0 software package, using a circular extraction region of 8' for the LECS and 4' for the MECS. LECS and MECS background spectra accumulated from blank field exposures and available at the SDC were used for spectral analysis. The response matrices released in 2000 January and in 1997 September were used for the LECS and MECS, respectively. For the PDS, both the light curve and the spectrum were retrieved from the SDC on-line archive. The LECS and MECS light curves show significant variability, with a few small flares. We therefore extracted separate spectra for the flares and the quiescent emission. No significant emission was detected by the PDS instrument: the count rate oscillated around zero with a standard deviation of ~ 0.01 cts s^{-1}.

In § 4.4.3 we will present the results of the spectral analysis. We will use the flux variations from the MECS detector in § 5 for multi-wavelength comparisons.

4. Analysis and Results

The following sections describe in detail the analysis of the large body of data comprising these campaigns. One of the main goals of the campaigns was to study flaring, and so it is necessary to describe the means by which flares are identified. "Flaring" can be defined objectively, such as the level where the count rate exceeds the average count rate by some factor. However, solar (and stellar) flares can exist in a range of luminosities such that small light curve modulations could be evidence of the lower end of the flare luminosity distribution; this would hinder our efforts to perform time-resolved spectral analysis of differences between "flares" and "quiescence". For the purposes of this study, we will use a more subjective way of identifying flares. Flares are large to moderate variations of the count rate above the surrounding count rates that appear to be systematic in time, i.e. display a rise, peak, and decay of count rates.

4.1. Radio Observations

Radio observations with the VLA and ATCA are a core component of the multi-wavelength observations. Data taken with the two arrays offers multi-frequency coverage of the nonthermal emission from the system during the campaigns and extends the temporal coverage compared with use of only one of the arrays. In these sections we discuss the observed patterns of radio flux (I) and circular polarization (π_c) in light of what we can learn about the emitting properties of HR 1099. These two quantities can be expressed as

$$\pi_c(\%) = \frac{V}{I} \times 100 = \frac{RR - LL}{RR + LL} \times 100 \quad , \tag{4-1}$$

where V and I are the Stokes parameters for circular polarization and total intensity, respectively, and RR and LL are the two components of circular polarization: right circularly polarized (RCP) and left circularly polarized (LCP) emission, respectively. In radio terminology, X-band refers to a wavelength of 3.6 cm (frequency of 8 GHz), C-band refers to a wavelength of 6 cm (frequency of 5 GHz), and L-band refers to a wavelength of 20 cm (frequency of 1.4 GHz).

4.1.1. Light Curve Variability

Figures 1a through 4b show the light curves of flux and polarization variations for the different frequencies in the four years of observation. Variations are most obvious at 3.6 and 20 cm, although they are also evident at other frequencies. The polarizations of 2, 3.6, and 6 cm data are generally positive, i.e., right circularly polarized. In contrast, the polarizations at 13 and 20 cm can be RCP, but during some flares the polarization becomes highly negatively (left) polarized. We term this behavior, which exhibits large levels of circular polarization and generally chaotic flux variations with time, as a burst, to distinguish it from flaring behavior seen at higher radio frequencies. During two highly polarized events at 13 and 20 cm, the 6 cm emission is also left circularly polarized. There is a general trend of declining flux and activity in later observing campaigns — the 1993 observations had the largest 3.6 cm flux levels and several large flares, but by 1998 the 3.6 cm flux levels are generally much smaller and there are few to no flares at 3.6 cm. These trends can be seen in the average flux and circular polarization values for the four years at 3.6 cm, listed in Table 2. The average flux declines and the average polarization increases, from 1993 to 1998; also evident is the decrease in the standard deviation of the average fluxes, indicating a decreasing amount of flux variability. These general trends are consistent with results reported previously by Mutel et al. (1987) who noted an inverse correlation between flux level and percent circular polarization for RS CVn systems. The decrease in the average flux density also implies a decrease in the level of "quiescence" during the four years of the observations. This is harder to quantify than an average flux density, but an inpsection of Figures 1a through 4a shows that the typical flux densities of times when no significant variability took place decreased from 1993 – 1998: in 1993 the level was 40–50 mJy, while in 1998 it was of order 8 mJy. Richards et al. (2003) monitored HR 1099 at 8 and 2.3 GHz using the Green Bank Interferometer, from 1995–2000, with several observations per day. While several large flares (peak fluxes up to 1.4 Jy) were evident on HR 1099 during this interval, none occurred near the times of our multi-wavelength campaigns in 1996 September and 1998 September, suggesting that the system was in a relatively inactive state during these times.

A closer look at several of the 3.6 cm flares also reveals a temporal pattern similar to the broader trend noticed by Mutel et al. (1987). Figure 5 show patterns of flux and polarization variations at 3.6 cm which illustrate this trend. Mutel et al. (1987) only used averages from observations, not a closely spaced temporal sequence. There is a hint in the flare on 1993 September 16 that the circular polarization reaches its minimum value before the flux level peaks. This effect described in Figure 5 for the 3.6 cm data is even clearer in the 20 cm data illustrated in Figure 6 . Inspection of the flares on 1994 August 26 and 1996 September 7 reveals that this is in fact the case: For the 1996 September 7 flare the flux peaks at September 7.361778, and the polarization has its minimum at September 7.35398, $\approx$ 11 minutes earlier. For the 1994 August 26 flare the difference in time between the peak in the flux and the minimum in the polarization is only $\sim$ 2 minutes, using a data sampling of 1 minute.

We can investigate the polarization of the flares by assuming a two-component model, composed of a quiescent source with flux I_Q and polarization π_Q, and a flare source with flux I_F and polarization π_F; the relation between the individual Stokes' parameters and fractional circular polarization for the quiescent source, flare source, and sum can be expressed as

$$I = \text{total flux} = I_Q + I_F \tag{4-2}$$

$$V = \text{total circularly polarized flux} = V_Q + V_F \tag{4-3}$$

$$\pi = \frac{V}{I}, \quad \pi_Q = \frac{V_Q}{I_Q}, \quad \pi_F = \frac{V_F}{I_F} \quad . \tag{4-4}$$

If the flares are completely unpolarized, then $\pi_F = 0$. We use values of quiescent flux and percent circular polarization determined from pre-flare averages, and plot the expected variation of total polarization during the flare as the flare flux changes. This is depicted in the middle panel of Figure 5 in red crosses and red circles. During the flare rise, the observed trends are consistent with an unpolarized flare emission source. At later stages in the flare, there is more observed circular polarization during the flare than is predicted, indicating that a small amount of flare polarization is present. Equation 4-4 implies a small amount of RCP (up to $\approx$ 20%) during the late stages of the flare.

We determined estimates of peak luminosities and energies of several radio flares.The flare energies were determined by integrating the observed flare light curve points, after subtraction of an estimated constant quiescent flux. Conversion to cgs units was done using 1 mJy = 10^{-26} erg cm^{-2} s^{-1} Hz^{-1}, and the Hipparcos distance to HR 1099 (29 pc). Determinations were made for every frequency where the flare was obvious – typically, X- and C-bands. Results are given in Table 3. The temporal evolution of the flux density at 3.6 and 6 cm for most of these flares is remarkably similar. The monotonic decay of microwave emission during the flare decays is indicative of well-trapped electrons.

Flaring behavior at 20 cm has completely different characteristics than that displayed at lower wavelengths. There are flares at 20 cm that display a change in polarization as the flux level increases, as seen in several 3.6 cm flares. In contrast with polarization levels at other frequencies, the 20 cm polarizations are negative, or left circularly polarized during these flares. Figure 6 shows two examples of 20 cm flares. This reversal of sense of polarization, or helicity, was pointed out by White & Franciosini (1995) as evidence of coherent bursts of radiation: an emitting mechanism distinct from incoherent gyrosynchrotron emission at higher frequencies, which generally keeps the same sense of polarization. Such highly polarized bursts are a relatively common phenomenon on dMe flare stars (Lang et al. 1983; Bastian et al. 1990), and have been interpreted as either emission at the plasma frequency or its harmonics, or radiation from an electron cyclotron maser instability, generally occurring at the cyclotron frequency or its harmonics (Stepanov et al. 1999, 2001; Bingham et al. 2001).

A glance at the polarization light curves (Figures 2b, 3b, and 4b) reveals that for a large amount of the time when HR 1099 was observed at 20 cm, the emission was highly negatively circularly polarized. We estimated the fraction of time the system was exhibiting this behavior, by filtering the polarization data for times when the amount of circular polarization was less than -20%. Roughly 30% of the time when HR 1099 was observed at 20 cm, the emission was characterized by moderate to large values of left circular polarization. The light curves are averages over typically several minutes, and larger variations on smaller timescales could be masked by averaging over large time bins. Thus this is an estimate, but does point out the apparently common nature of such events on HR 1099.

We investigated the flare polarizations for these 20 cm flares in the same way as described above for 3.6 cm flares, by assuming a two-component model of a quiescent source and a flare source contributing to the total observed flux and polarization. In contrast to the 3.6 cm flares, a large amount of left circular polarization is necessary to reproduce the observed polarization variations during these flares. Figure 6 shows the expected polarization variations if the flare is 100% LCP in red crosses and circles, which is consistent with the observed polarization levels. Thus the total polarization can be described as an equal admixture of quiescent polarization at a few percent RCP and 100% left circularly polarized flare emission. This behavior is consistent with expected coherent emission, which should be 100% circularly polarized if it is fundamental plasma emission.

We examined the light curves of flux and polarization changes in Figures 1a through 4b to determine if there was a significant degree of correlation between flares at 20 cm and those at higher frequencies, which are generally attributed to gyrosynchrotron flares. We use a relatively lenient restriction, looking for a close temporal association (within $\sim$ 1 day) between 3.6 cm flares and either an increase in flux or significant amounts of left circularly polarized emission at 20 cm. Table 4 details the 20 cm and 3.6 cm behavior. There is a low correlation between 3.6 cm flares and 20 cm flux/polarization enhancements; only 3 out of the 12 events show a 3.6 cm flare during the same $\approx$ 17 hours of each day where radio coverage at both frequencies was obtained. There are a much larger number of bursts at 20 cm than at 3.6 cm.

The ATCA observations at 13 cm also exhibit some of the same behavior as seen at 20 cm: highly polarized, short duration enhancements. There are two cases with negative circular polarization at 6 cm, 1996 September 3–4 and 1998 September 8–9. The 6 cm data are not simultaneous with the 13/20 cm recordings, but both 6 cm events are accompanied by highly polarized flares at 13 and 20 cm. Since the ATCA data offer simultaneous 13 and 20 cm coverage with the same time binning and resolution, we examined correlations between polarizations at these two frequencies. The time binning is rather coarse for investigating what presumably are short duration bursts; the bins are $\approx$ 15 minutes full width and separated by about 30 minutes. There are only two occasions where the 13 cm LCP emission is accompanied by corresponding LCP 20 cm emission — 1994 August 24–25 and 1996 September 3–4. In the former, the 13 cm emission is left circularly polarized for only $\sim$ 2 hours, whereas the 20 cm data shows LCP for $\sim$ 7 hours. The 20 cm flux peaks earlier than the 13 cm flux and is declining from maximum when the 13 cm flux is increasing to its maximum flux. The 20 cm data reaches its maximum negative left circular polarization when the 20 cm flux peaks, and likewise with the 13 cm LCP and flux. The percent of 20 cm LCP emission is much larger at its peak than the peak of the 13 cm percent LCP emission by about a factor of three. This behavior, with a temporal difference in peak flux and polarization between 13 and 20 cm, could be attributed to a frequency drift in coherent emission between these two frequencies, but the frequency difference ($\Delta\nu \sim 988$ MHz) and temporal difference between flux peaks ($\Delta t \sim 8400$ seconds) leads to a frequency drift rate of $\sim$0.12 MHz s^{-1}, which is about 3 orders of magnitude smaller than frequency drift rates seen in solar phenomena (and deduced from dMe flare star bursts; Güdel et al. 1989), and thus the behavior in the two frequency bands are probably not related.

The second period of LCP emission at both 13 and 20 cm is 1996 September 3–4. Here the behavior is more complicated. There is a close association in the flux evolution at the two frequencies, but the variation of the circular polarization shows no apparent correlation. The 13 cm and 20 cm circular polarizations are changing rapidly with time in the half hour between each subsequent scan, suggesting that much finer temporal variations are taking place. With such coarse time binning it is difficult to say whether the LCP behavior at 20 cm is related to the 13 cm behavior. We note, however, that there are many more instances of highly left circularly polarized behavior at 20 cm, which implies that it is a separate phenomenon from the LCP emission at 13 cm, although we cannot rule out a causal relationship. There is also 6 cm emission that is left circularly polarized during the general time of 13/20 cm bursts — it is consistent with quiescent emission just before and after the burst, and a 50–80% left circularly polarized burst component.

For time periods when the 20 cm light curves show highly LCP emission, we investigated trends in LL and RR flux with time. We found in most cases that temporal resolution at the 10 second level, the time sampling of the VLA data, was necessary to determine the detailed flux variations; sampling on even shorter timescales might be necessary, although unobtainable with this dataset. Figure 7 illustrates several cases of both long and short duration, highly polarized bursts. There are rises and decays which last less than one minute, along with a complex morphology that might indicate a long series of multiple overlapping bursts, each occurring on timescales less than 10 seconds. For all these bursts, the LCP flux dominates over the RCP flux, indicating negatively circularly polarized emission. In contrast to the LCP flux, which shows great variations, the RCP flux is remarkably constant. We also investigated the difference in temporal evolution of the flux at the two intermediate frequency (IF) bands used in continuum mode observing at 20 cm: 1440–1490 and 1360–1410 MHz in 1994 August. The bottom two panels of Figure 7 detail two different kinds of behavior. In the first case, both IF bands show similar evolution; and in the second, the flux patterns change with time and frequency. This latter case is different from what was observed by White & Franciosini (1995) where the LCP flux in the two sidebands was equal and varying in the same way.

4.1.2. Flux and Polarization Spectra

We investigated the trends of flux and polarization with frequency for the multi-frequency radio datasets. While the frequency coverage is not strictly simultaneous due to frequency switching or combining coverage with the VLA and ATCA, we can obtain contemporaneous multi-frequency coverage of up to five frequencies spanning an order of magnitude in frequency to within about a half an hour. During periods where there is no obvious flaring at any wavelengths, such time intervals should be small enough to record the general characteristics of the quiescent radio emission. Problems arise, however, when variability is present at one or more frequencies, and then we can only diagnose some "average" conditions which may or may not represent the actual conditions.

We concentrate on time intervals when 2 cm observations occurred, to extend the frequency coverage, although for the 1993 observations no recordings at 2 cm were obtained. We extracted flux and polarization information from the light curve data for each frequency that was close enough in time to provide adequate temporal and frequency coverage, generally within about 30 minutes of the 2 cm observation. Spectral indices were computed for each successive frequency pair; the spectral index α (where $S_\nu \propto \nu^\alpha$) is computed using a least-squares linear fit to the logarithmic flux and frequency data, and are listed in Table 5. We have sorted the time intervals according to the general light curve behavior the system was exhibiting: either quiescent behavior or the peak/decay of a 3.6 cm flare. Figure 8 displays the flux and polarization spectra typical for these activity levels.

For all the intervals where flux and polarization spectra could be determined, the polarization shows an increasing trend with frequency, regardless of the behavior of the flux spectra. The characteristics of the flux spectra are consistent with previously determined behavior on active binary systems. The quiescent data generally show a decline in flux with increasing frequency. The indices for quiescent observations are flat or slightly negative, $0 \leq \alpha \leq -1$, with an exception being 1998 Sept. 10.3, which has a 3.6–2 cm spectral index of -2.32 ± 0.39. This declining trend of flux with frequency suggests that the emission is optically thin. The increase in observed circular polarization with frequency is in contrast to the expected behavior of optically thin nonthermal gyrosynchrotron radiation from a homogeneous source; however, it is difficult to obtain large values of percent circular polarization under optically thick conditions (Jones et al. 1994). White & Franciosini (1995) have found similar evidence for a rising polarization spectrum with frequency being independent of the flux spectrum shape for a sample of active binary systems.

Several flares at 3.6 cm show corresponding intensity variations at 6 cm, and we investigated these flares for changes in the spectral index $\alpha_{6-3.6}$ during the course of the flare. Figure 5 shows the results for three moderate-sized flares. In general, there is a positive, linear correlation between the flux and spectral index. This is in accord with the general trends noted by Mutel et al. (1987) between the spectral index and luminosity for a sample of active binary systems. During the rise to peak intensity, the spectral index flattens, becoming less negative, even changing sign and becoming increasingly positive for two cases (1994 August 26.5 and 1996 September 7.35). This may signal a change to optically thick emission at the flare peak, and would explain the apparent zero polarization level of the flare, in combination with a positive amount of quiescent circular polarization. The shift from optically thin to optically thick conditions at the flare peak, and return afterwards, implies that the peak frequency ν_{peak} (where $\tau = 1$) is $>$ 8.3 GHz during the flare rise and peak, and $<$ 5 GHz during the flare decay.

4.2. Analysis of UV Observations

Dempsey et al. (1996) discuss the analysis of the 1993 *IUE* observations and 1993 *HST/GHRS* observations. Brown et al. (1994) discuss the analysis of the 1994 *IUE* observations. We will utilize the temporal variations of the extracted line fluxes of C IV and Mg II in our multi-wavelength comparisons in § 5.

4.3. Analysis of *EUVE* Observations

4.3.1. EUV Light Curve Variability

Figure 9 shows the light curves in the EUV during the four observations which comprise this campaign. During the first three observations of HR 1099 the system was in an extremely active state. By comparison, during the fourth observation, in 1998, HR 1099 was relatively inactive, signalling an abrupt change in activity level.

We also attempted to quantify and compare the activity of the system by examining the average non-flaring count rate during the four observations. Determining the actual quiescent level of the system is somewhat difficult, due to the obvious influence of large flares in the light curve. The quiescent, or non-flaring level, might also be affected by rotational modulation of starspots or numerous small-scale flares which occur too close together in time to resolve with *EUVE*'s poor orbital efficiency. The actual quiescent level may be below the average count rate outside of flares in these observations. Nevertheless, we can use these values as upper limits to the actual level of non-flaring emission. In 1993, the average non-flaring luminosity was $9.6\pm1.2\times10^{29}$ erg s^{-1}; in 1994 it was $5.4\pm0.5\times10^{29}$ ergs s^{-1}; in 1996 it was $6.6\pm1.0\times10^{29}$ ergs s^{-1}; and in 1998 it was $6.6\pm0.9\times10^{29}$ ergs s^{-1}. The average level in 1993 is 50–100% higher compared with the average levels in 1994, 1996, and 1998. The significant variability the system was undergoing during most of the observations hampers our efforts to look for evidence of rotational modulation or orbital phase-dependent effects. Also, the observations were spaced far enough apart (generally ∼ one or two years) that changes in the "quiescent" level of the system, could be due to evolution in starspot configuration, if these changes are attributable to phase-dependent effects from starspots.

The top panel of Figure 10 plots the cumulative luminosity distribution of events greater than a given L_X for all six DS/S pointed observations, from 1992, 1993, 1994, 1996, 1998, and 1999, along with the distribution resulting from all the observations taken together. For this comparison, the binning of each light curve was fixed, at ≈ 3000 seconds. The data from the 1992 and 1999 observations, reported in Drake et al. (1994) and Ayres et al. (2001a), were reduced in a similar manner as the data obtained during our 1993, 1994, 1996, and 1998 campaigns. The behavior of this cumulative distribution varies greatly; only in 1993 and 1996 were there events with luminosities greater than 2×10^{30} ergs s^{-1}. The flattening of each distribution at low luminosity probably represents the quiescent emission level, which appears to vary from year to year. The roll-over at high luminosities represents the very largest flares, which happen less frequently. The bottom panel of Figure 10 shows the cumulative distribution of the sum of the pointed observations, expressed as a percent probability distribution. Note that even with the extremes of variability shown in Figure 9 the range of luminosities is still less than a factor of seven between the lowest and highest observed luminosities, the bulk of the observations occuring over a smaller range of ≈ 4 in luminosity. High luminosity events greater than 2×10^{30} ergs s^{-1} actually comprise about 10% of the total number of events in the more than one megasecond of observations from 1992 to 1999.

Figure 11 shows the details of the four largest flares seen with *EUVE*. These flares occurred over the course of many days, in some cases having durations that equal or exceed the stellar orbital period. Long duration high-energy flares on RS CVn binary systems are common (Graffagnino et al. 1995; Ottmann & Schmitt 1994; Kuerster & Schmitt 1996). Such long timescales require sustained heating; for a $\sim 10^7$K plasma with electron density $n_e \sim 10^8$–10^{13} cm^{-3}, the radiative decay time is ∼ 20–2 $\times 10^4$ s. The lack of self-eclipses implies either large sizes or an appropriate location with respect to the stellar axis and the orbital plane.

The flare rises and decays show a remarkable smoothness in the evolution of the count rate. In past analyses of EUV light curves (Osten & Brown 1999; Osten et al. 2000) we assumed that most EUV and X-ray light curves could be expressed as a single exponential rise and one or two exponential decays: a result of exponential changes of density and/or temperature during the flare. For the two large flares observed in 1993 September, this pattern of multiple decay phases appears to hold – both show two distinct decay phases, an initial fast decay followed by a second slower decay. The fast exponential rise and exponential decays plotted in Figure 11 are taken from Osten & Brown (1999). Further probing of EUV flare light curves reveals an increasingly complex flare morphology: Several of the large flares appear to have an inflection in the flare rise with a transition from a slow rise to fast rise, similar to the two decay phases, as shown in Figure 11. The two flares that occurred during the 1993 September observation typify this behavior.

We examined the significance of these slow rises by comparing how well the data were fit by an exponential rise and a constant, quiescent rate, using the reduced chi-squared (χ^2_ν) statistic. The exponential fits are shown in Figure 11. The constant value was determined by averaging count rates in other temporal regions which did not seem to be affected by flares. The slow rise yielded lower χ^2_ν values: For the 1993 September 16 flare, 1.7 (ν =7) compared with 7.6 (ν =8) for a constant rate; for the 1994 August flare, 1.3 (ν =39) against 25.1 (ν =40) for a straight line; and for the 1996 September large flare, 1.2 (ν =57) versus 4.7 (ν =58). Figure 11 illustrates the exponential fits, and delineates the average count rate for each observation, along with the standard deviation of the average count rate. There is a large amount of variability present, even during seemingly quiescent conditions. The increase in luminosity before the impulsive rise is reminiscent of a flare precursor (destabilization of a filament prior to the main event), corresponding to an energy leakage before the main energy release during the flare, as has been discussed for solar flares (see discussion in section 6.5 of Tandberg-Hanssen & Emslie 1988). In the Sun, pre-flare heating and brightening is due to slow rearrangement of the magnetic field and subsequent slow energy release before the impulsive energy release that marks the flare, although not all solar flares exhibit this behavior. The slow energy release may reveal itself as a gradual increase in the plasma radiation.

We compared the similarity of flare light curves by shifting the flares in time and flux so that the peaks coincide. The top panel of Figure 12 shows the two flares in 1993 and the large flare at the end of 1994 superimposed on each other in this way. There is a striking similarity in the rise phases of all three flares. The inflection point in the three flares also appears to occur at roughly the same time before the peak of the flares. The decays of the two flares in 1993 are remarkably similar; the comparison with the 1994 flare breaks down, however, as it appears to plateau for $\sim$ 5 hours before undergoing a single decay. A small flare can be seen peaking on 1994 August 25.8 during the long rise of the 1994 flare shown in Figure 11.

The middle panel of Figure 12 compares the two flares that comprise the double flare seen in 1996 September. Here the similarity in the two flares is even more striking. Plotted in black is the rise and partial decay of the first flare, with the partial rise and decay of the second flare in red shifted on top of it. While we don't have the complete decay of the first flare nor the complete rise of the second flare, the parts that do overlap show a surprising amount of symmetry. We explored this further by reflecting the second flare about the peak, to compare the rise of the first flare with the decay of the second. This reflection is shown in the middle panel of Figure 12 in green. Both flares appear to attain a constant value for ~ 8 hours before decaying. Sanz-Forcada et al. (2002) have examined the *EUVE* datasets presented here. They accumulate quiescent and flare intervals to obtain high S/N spectra of quiescence and flaring, and investigate properties of the emission measure distribution. They suggest that the double flare seen in 1996 September is actually one flare that is self-eclipsed. If this is the case, then the resulting single flare is of enormous proportions, lasting ≈ 3.5 days after a possible flare precursor, or 1.2 rotational and orbital periods. The symmetry of the rise of the first feature and decay of the second would then be in line with symmetries found in morphologies of other flares.

We examined the smaller luminosity flares in the same way to look for patterns of similarity. Most of these six small flares have peaks less than about two times the quiescent luminosity. For the most part these flares appear to be symmetrical, with a long rise and decay. Two flares, however, show a different morphology which is more akin to the classical picture of stellar flares. The flare which peaked on 1994 August 24.2 and that which peaked on 1996 September 5.3 are asymmetrical in the sense that the rise happens very quickly but the decay is long. The two asymmetric flares are remarkably similar as well, when shifted and scaled (see Figure 12, bottom panel).

The general characteristics of most flares seen here show marked departures from the "canonical" flare shape — a fast rise followed by a slow decay. For many of these EUV flares, the evolution of the flare rise and decay is at the same rate. Only two flares appear to show a fast rise and slow decay. In the solar scenario, the energy release, particle acceleration and heating of lower atmosphere plasma to coronal temperatures and subsequent ablation into coronal loops happens quickly (apart from a possible pre-flare cursor; see above); this is the impulsive phase. Perhaps the symmetry between rise and decay in flares seen on active binary systems reflects the nature of the energy release, which happens on longer timescales (gradual instead of explosive evaporation) or in a larger arcade of loops. If multiple loops were involved in producing the flare we see in the light curve, then the slow rise could be interpreted as progressive brightenings as subsequent coronal loops become filled with coronal plasma and radiate. At what we identify as the peak of the flare, the maximum number of loops is filled, or the largest loops in a size distribution of loops are filled with coronal plasma, the radiation reaches a peak and the plasma cools via radiation and conduction (and possibly continued heating; see Favata et al. 2001), leading to a decline in flux.

4.3.2. EUV Spectra

We investigated spectral variations in the *EUVE* data, dividing the data into temporal segments corresponding to the general activity in the system. As described in §3.5, the goal of this paper is to investigate flares on a case-by-case basis. Based on our analysis of the light curves in §4.3.1, we identified temporal intervals corresponding to quiescence and flares, and marked those for subsequent spectral extraction. Figure 9 shows the light curves and corresponding time intervals in which spectra were accumulated; 'Q' refers to quiescent times, 'F' to flare times (often several small-amplitude flares), and 'F1', 'F2', etc. to discrete large-amplitude flares. Table 6 lists the exposure time in the SW and MW for the time intervals indicated in Figure 9. Figures 13 and 14 display the SW and MW spectra for these time intervals, with selected emission lines identified. The spectra are dominated by lines of highly ionized iron — ionization stages XV–XXIV. In spite of the dramatic changes illustrated by the light curves, the corresponding spectral changes are less overwhelming. The most noticeable increases that occur during flare segments compared to quiescent segments are enhancements in the flux from the Fe XXIII/XX λ 132.85 and Fe XXIV $\lambda\lambda$ 192.02, 255.09. Other lines appear to be at the same flux level. Due to the low sensitivity of the *EUVE* spectrometers, the flare spectra have not had any estimate of quiescent flux subtracted, and thus represent a combination of flare and quiescent plasma.

The assumptions we make in analyzing the spectra are that the emission is from a collisionally ionized plasma, in equilibrium, and effectively thin. Under such circumstances, the plasma is in a steady state between collisional ionization and radiative and dielectronic recombination; line formation is a balance between collisional excitation and radiative de-excitation. The effectively thin assumption implies that all the emitted photons escape; some (typically 1/2) are directed outward toward the observer and some are directed inward, possibly to the stellar surface (depending on the geometry). The observed flux can be written as a product of the elemental abundance times an integral involving the plasma emissivity and the differential emission measure:

$$f_{\rm obs} \propto \frac{A}{4\pi d^2} \int P_\lambda(T) n_e n_H \frac{dV}{d\log T} d\log T \tag{4-5}$$

where A is the elemental abundance, P_λ is the plasma emissivity. The quantity $n_e n_H \frac{dV}{d\log T} \equiv \phi(T)$ is the differential emission measure (DEM), or the emission measure (EM) differential in temperature,

$$EM = n_e n_H dV = \phi(T) d\log T \quad . \tag{4-6}$$

Bright lines of iron dominate the spectrum and span a relatively wide temperature range (from Fe XV at 2 MK to Fe XXIV at 20 MK); for these reasons we use these lines to constrain the shape of the coronal differential emission measure distribution. Since the DEM thus determined is relative to the coronal abundance of iron, this eliminates the necessity of determining the iron abundance simultaneously with the DEM. Previous studies that have attempted to constrain both these quantities have found that generally two classes of results match the data statistically: A DEM with a peak between 1 and 30 MK with subsolar iron abundances, or a solar abundance plasma with a marked peak at 100 MK (Schrijver et al. 1995). Restricting the DEM determination by only using iron lines removes some of this ambiguity.

We measured emission line fluxes of lines in the SW and MW spectra by generating a linelist from the plasma emissivities taken from Smith et al. (2001) and assuming a Gaussian line profile. These emissivities have been calculated in the low density limit, and agree with those of Brickhouse et al. (1995) in their low density limit. The full width at half maximum of the line profiles were fixed at the instrumental resolution: 0.38 Å for SW and 1.14 Å for MW. We corrected for the effects of interstellar absorption in the SW and MW spectra by using photoabsorption cross section calculations of Morrison & McCammon (1983) and a hydrogen column density of 1.35 10^{18} cm^{-2} as derived by Piskunov et al. (1997).

The analysis of *EUVE* spectral data is complicated by the presence of continuum emission. Although present only at a low flux level, the continuum flux rises to shorter wavelengths, and can introduce errors in determining the fluxes of emission lines. Pinning down the level of continuum emission requires having line-free regions of the spectrum. The EUV spectral region is littered with numerous weak emission lines in the atomic codes, and the incompleteness of the codes in this region is a recognized problem (Jordan 1996; Beiersdorfer et al. 1999). An added complication is the formation of the continuum flux at temperatures higher than those diagnosed with the emission lines present in the *EUVE* spectrum. Previous studies of stellar coronae in X-rays have revealed coronal elemental abundances that are less than solar (e.g., Singh et al. 1996) and appear to vary during flares (e.g., Güdel et al. 1999). This leads to an increased amount of continuum emission, because the DEM here is computed relative to the iron abundance. Decreasing the iron abundance necessitates raising the DEM by the same amount so that the predicted line flux does not change: A larger DEM consequently produces more continuum flux.

We investigated the effect of sub-solar iron abundances in the spectrum. We performed an initial analysis of the data assuming that the abundance was equal to the solar photospheric abundances of Anders & Grevesse (1989), the minimum amount of continuum that might exist in the spectrum, and using the method described below to generate the DEM. We then predicted what the level of the continuum spectrum should be based on abundances ranging from solar to one tenth the solar photospheric abundance of iron. Figure 15 shows the SW composite quiescent and flare spectra and continuum spectra overlaid. The spectra have been corrected for the effect of interstellar absorption. Abundances ≥ 0.2 times the solar value produce a continuum level that can be compatible with the observed flux levels from both the composite quiescent and flare spectra. Table 7 tabulates the discrepancy in measuring emission line fluxes between assuming no continuum flux, and subtracting a continuum calculated with varying abundances. The discrepancy between line fluxes determined with no continuum subtraction and a continuum calculated assuming very sub-solar abundances grows larger with decreasing abundance.

We also examined shorter time intervals, in which the line fluxes have poorer S/N. In both a shorter quiescent interval (**1998Q**) and a flare interval (**1994F**), the difference in emission line flux introduced by not subtracting a continuum compared with assuming a continuum with iron abundance >0.4 was at the same level as the photometric errors. This is a different result from that obtained for the composite spectra (where Fe/H $\geq$0.2 solar), due mostly to S/N issues. In the following analysis of the *EUVE* data, which uses the lower S/N spectra to examine activity-related spectral changes, we take the coronal iron abundance of HR 1099 to be 0.4 for all time segments, thus assuming the iron abundance does not vary during flares. This is a conservative estimate based on the fluxes in short time interval spectra: The *EUVE* data can only constrain Fe/H to be ≥ 0.2.

The DEM was determined from the emission lines of iron, as described above; initially no continuum flux was subtracted before measuring emission lines. Once the DEM was constrained, a continuum was predicted using the DEM and an iron to hydrogen ratio of 0.4 times the solar photospheric value as given in Anders & Grevesse (1989) and subtracted from the observed spectrum. The emission lines were re-fitted, and the DEM was redetermined. The method for constraining the DEM is an interactive one; the user chooses a value of the DEM at each temperature bin ($\Delta \log T = 0.1$, from $\log T$=6.2–7.5), and adjusts the value of the DEM at each temperature bin until there is suitable agreement between observed line fluxes and those predicted by the DEM. Because plasma emissivities in the low density limit are used, any line exhibiting a departure from collisional ionization equilibrium was not used to constrain the DEM. For temporal intervals where lines of Fe XV,XVI were not detected, the temperature coverage available by lines of Fe XVIII–XXIV is limited to $\log T$ =6.7–7.5. Figure 16a shows the DEMs determined for quiescent intervals; Figures 16b and 16c display the same quantities for flaring intervals. Tables 8 and 9 list the emission line fluxes after continuum subtraction. Figure 17 compares the quiescent and flare DEMs for two cases.

After determining the DEM, and subtracting off our estimate of the continuum emission, the resulting line fits should be due to emission line flux alone. There are transitions in the EUV where the assumption of collisional ionization equilibrium breaks down, due to a metastable upper level. In these cases the emissivity is proportional to the electron density, not the square. The ratio of one of these lines with a line in collisional ionization equilibrium yields an estimate of the electron density at the temperature where the lines are emitted. Two lines of Fe XXI, 102.22 Å and 128.73 Å, satisfy this condition, as do λ114.41 and λ117.17 of Fe XXII. We used the line flux measurements and statistical errors to estimate the electron densities of Fe XXI and Fe XXII. Table 10 lists the electron densities and errors derived for the different time intervals. Figure 18 illustrates the variation in electron density of the different time intervals. There is no significant difference between electron densities derived from flare intervals and those derived from quiescent intervals. This is partly due to the admixture of quiescent flux and flare flux in the spectra extracted from flare intervals (the flare intervals have been defined broadly and encompass regions of only moderate enhancement), and partly from the poor S/N in flare spectra due to the shorter duration of the flares compared to quiescent intervals. Yet, despite these caveats, there is no evidence for significant density enhancements, such as the factors of $\approx$ 10 or greater as seen in solar flares (Bruner et al. 1988). Previous investigations of flares on RS CVn systems with *EUVE* have also shown a lack of conclusive evidence for density enhancements during flare intervals (Sanz-Forcada et al. 2002).

4.4. Analysis of X-ray Observations

Four X-ray observations by three X-ray satellites: *ASCA*, *RXTE*, and *BeppoSAX* were obtained as part of the HR 1099 observations in 1994, 1996, and 1998. While the wavelength coverage, spectral resolution and wavelength of peak sensitivity differ, they all diagnose the very hot plasma (T$\geq$ few MK) present in active binary systems, and are sensitive to much hotter temperatures than the *EUVE* spectra. In the following we analyze the *ASCA*, *RXTE* and *BeppoSAX* datasets individually.

4.4.1. ASCA

As seen in Figure 19, the *ASCA* observation revealed a small flare with an enhancement of $\approx$ 1.8 in the 0.6–10 keV bandpass over the non-flaring level; the flare lasted approximately 8.7 hours. Because of the variability the system was undergoing during the observation, we extracted five different time intervals, denoted **Q** for the non-flaring bit, **R** for the rise of the flare, **P** for the flare peak, and **D1** and **D2** for the two decays of the flare.

The top panel of Figure 19 shows the *ASCA* light curve in three different bandpasses, normalized to their respective average quiescent count rates. The plot illustrates the different response of these energy bands (0.6–2 keV, 2–5 keV, 5–10 keV) to the flare. There is much more flux, relative to the quiescent level, in the higher energy bandpasses. This indicates the increased amount of continuum emission present during the flare. The bandpass 0.6–2 keV covers the peak in the observed spectral distribution, which has contributions mainly from iron L shell emission lines. The 2–5 keV energy range contains emission from hydrogen- and helium-like lines of Ca, Ar, S, and Si, as well as underlying continuum emission. The highest energy range, 5–10 keV, contains mainly continuum emission and the hydrogenic and helium-like lines of iron. With higher temperatures come larger amounts of continuum emission, since above temperatures of $\approx$ 15–20 MK most of the abundant elements are fully stripped and thus there are relatively few line transitions.

Table 11 gives the luminosities in these three bandpasses for the five temporal intervals extracted for spectral analysis (see Figure 19) along with the total luminosity in the 0.6–10 keV range. The luminosity peaks in the **R** and **P** temporal intervals, consistent with the light curve. Using the Hipparcos distance of 29 pc (Perryman et al. 1997), we subtract the X-ray luminosity during quiescence from the X-ray luminosities during the four subsequent time intervals to estimate the net amount of energy radiated during the flare. The system is bright during quiescence, with L_X of 7.5 10^{30} ergs s^{-1} in 0.6–10 keV and increasing to 1.3 10^{31} ergs s^{-1} at the peak of the flare. The total amount of flare radiation is 5.3 10^{34} ergs. Table 11 also lists the rise and decay timescales for the flare in different energy bands, assuming the count rate increases and decreases exponentially during the flare rise and decay, respectively. The higher energy bandpasses display a faster response to the flare.

The SIS0 spectra for the five time intervals are shown in Fig. 20. The spectra were fitted with a discrete, two-temperature VMEKAL model; the hydrogen column density, N_H, was fixed at 1.35 10^{18} cm^{-2} as determined by Piskunov et al. (1997). The abundances of elements O, Ne, Mg, Si, S, Ar, Ca, Fe, and Ni were allowed to vary. Results from spectral fitting to combinations of the SIS0, SIS1, and GIS2 spectra are given in Table 12.[7] We also used SPEX to determine the emission measure distribution assuming a multi-thermal plasma, with the abundances fixed at those determined from the 2T fits. The left panel of Figure 21 shows the resulting emission measures for the five time intervals. The peaks are consistent with temperatures derived from 2T fits, and show an increase in temperature

[7]The location of oxygen lines used in the abundance analysis are near the cutoff at 0.6 keV, and suffer from calibration problems; see http://asca.gsfc.nasa.gov/docs/asca/watchout.html.

during the flare peak, with a gradual subsidance to the quiescent level as the flare decays. The abundances show a statistically significant small increase during the rise of the flare; iron increases a maximum of a factor of three from 13% of the solar photospheric value in quiescence to 32% during the rise phase, decreasing in value over the course of the peak and decay to the value attained during quiescence. This change can be seen in the evolution of the feature in the *ASCA* spectra at 6.7 keV, due to Fe XXV. Any definitive trend for other elemental abundances is marred by the large uncertainties on these abundances. The right panel of Fig. 21 plots the abundances of Ca, Mg, Fe, Si, S, O, and Ar during the five time intervals against the First Ionization Potential (FIP). There does not appear to be any FIP-dependent abundance enhancement. The abundance of Ne, with a FIP of 21.6 eV, unfortunately suffers from large error bars and it is difficult to discern any changes in this abundance through the evolution of the flare.

4.4.2. RXTE

The final, background-subtracted *RXTE* light curves are shown in Fig. 22, binned into 128 second intervals for the 1996 observation and 256 second intervals for the 1998 observation. The data are sparsely sampled in time, but one large flare in 1996 and another in 1998 are evident. We plot the light curves for these flares in two energy bandpasses, 2–5 keV and 5–12 keV, to examine how the flare evolves at different energies. We see similar behavior to that in the *ASCA* light curve in 1994 — the higher energy bandpass (here 5–12 keV) has a much more rapid response to the flare, showing a faster rise and a faster decay compared with 2–5 keV.

We can estimate the amount of energy radiated during these flares by determining a luminosity–count-rate conversion, using the average count rate during the observation, and converting the integrated flux to luminosity. The luminosities in 2–5, 5–12 and 2–12 keV bandpasses were calculated using a 2T MEKAL model applied to the 2–12 keV spectrum accumulated from the entire observation of each year, and are listed in Table 13. We tabulated the net flare energy, determined by summing the observed counts during the flare, converting to energy using the luminosity–count-rate conversion, to obtain the amount of energy radiated during the flare, including the quiescent contribution. The quiescent contribution to the total flare energy was estimated by taking the quiescent count rate, multiplying by the flare duration, and converting to energy using the conversion factor. This quiescent emission was subtracted to give a net estimate of the amount of energy radiated during the flare in each bandpass; these values are listed in Table 14. Both flares lasted only a few hours, yet each radiated a substantial amount of energy ($\sim$ few 10^{34} erg) in the 2–12 keV bandpass. The flare energies in the 2–5 and 5-12 keV bandpasses also are similar.

Also listed in Table 14 are the rise (τ_r) and decay (τ_d) timescales, computed assuming an exponentially increasing and decreasing time profile of the flare. Due to the gaps in the timeseries, neither flare was observed in its entirety; for the 1998 flare we are unable to constrain the rise time due to inadequate temporal sampling. A comparison of the flare timescales for the 2–5 and 5–12 keV bandpasses for both flares reveals smaller timescales, and hence more rapid increases and decreases in flux changes with time, for the higher energy bandpass. This trend was noted by Osten et al. (2000) for another active binary system, σ^2 CrB.

4.4.3. BeppoSAX

The HR 1099 LECS and MECS light curves are shown in Figure 23. A small flare occurred just at the beginning of the observation, followed by a second one during the decay; a third flare occurred at the end of the observation. In all three cases the peak count rate in the MECS increased by a factor of $\sim 2 - 2.5$ with respect to the quiescent one. A few smaller peaks are also evident in the light curve. Given the variability of the emission, we have divided the observation into five separate time intervals, covering the three main flares (labeled **F1**, **F2** and **F3**), the late decay phase of the first two flares (labeled **D**) and the presumably quiescent interval before the third flare (labeled **Q**). In Table 15 we give the luminosities for the five intervals in the same energy bands as *ASCA* for comparison (see Table 11). The quiescent luminosity in the 0.6–10 keV band is 5 10^{30} erg s^{-1}, a factor of $\sim$ 1.4 lower than in the 1994 *ASCA* observation, and rises to 7.8 10^{30} erg s^{-1} during the first two flares. In Table 15 we also give the flare timescales in the MECS band (1.6–10 keV) assuming an exponential rise and decay. While the second and third flare are similar, with rise and decay timescales of $\sim$ 2 and $\sim$ 4 hrs, respectively, the first flare shows a more gradual behaviour, with rise and decay times of $\sim$ 11 and $\sim$ 13 hours. We also note that after the second flare the decay of the emission is slower.

Joint fits of the LECS+MECS spectra have been performed for each time interval. The LECS data have been fitted in the $0.1-4$ keV band only due to calibration problems at higher energies (Fiore et al. 1999). In order to account for the uncertainties in the intercalibration of the LECS and MECS instruments, a relative normalization factor (which was left free to vary) has been included in the fits: the derived best-fit values are $\sim$ 0.8 for all spectra, in agreement with the allowed range of 0.7–1 (Fiore et al. 1999). All spectra have been fitted assuming a 2-temperature MEKAL model with variable global metal abundances, since the lower energy resolution of *BeppoSAX* with respect to *ASCA* does not allow a reliable determination of the individual abundances. The interstellar column density was kept fixed to the value $N_H = 1.35\ 10^{18}$ (Piskunov et al. 1997).

The best-fit parameters are given in Table 16 and the spectra are shown in Figure 24. There is a very good agreement with the parameters derived by *ASCA*, both for the quiescent and flaring spectra, with only a slight difference in the quiescent emission measures, that in *BeppoSAX* are lower by a factor of ~ 1.5. The temperature and emission measure of the hot component are higher during the flares, while the cool component remains constant. Contrary to the *ASCA* flare, we do not find any evidence for an increase of the global abundance, which has a value of $Z \sim 0.3$. This value is consistent with the individual abundances derived by *ASCA*, with the exception of Ni and Ne.

5. Multi-Wavelength Comparisons

Figures 25 through 28 depict the portions of the campaigns from different telescopes that overlap in time. Clear correlations exist between behavior in different spectral regions. Several large flares were caught with EUV/SXR telescopes, and 3.6 cm radio variability indicates a substantial amount of gyrosynchrotron flaring as well. The data are sparsely sampled, suffer from gaps due to earth occultations, and incomplete temporal coverage by ground-based radio telescopes, but several trends shine through: Radio gyrosynchrotron and EUV/SXR flares generally are correlated, with radio flares preceding the thermal emission, and UV emissions exhibit changes that seem to occur during radio flares.

Güdel & Benz (1993) noted an almost linear correlation between X-ray and radio quiescent luminosities for stellar coronae on a number of different kinds of stars, from solar flares to dMe flare stars to flares on RS CVn binary systems. For RS CVn systems containing a subgiant and a main sequence star, the correlation was $L_X/L_R = 0.17\ 10^{15.5\pm0.5}$ Hz. The observational relation was based on measurements of the X-ray luminosity with ROSAT and Einstein, at X-ray energies of 0.2–2.4 keV, typically. In Table 17, we list 3.6 cm radio luminosities and simultaneously obtained EUV (80–180Å) luminosities from the four different campaigns. The ratio of the EUV to radio luminosity spans the range $1.2\ 10^{13}$ – $8.2\ 10^{13}$ Hz, which is slightly lower than the observed values of Güdel & Benz (1993). However, if we take into account the relative amount of radiation in the differing bandpasses for a thermal plasma with a temperature distributions as determined in Section 6.1, the numbers are roughly consistent. Most of the radio and X-ray observations presented in Güdel & Benz (1993) were obtained at widely different times, and so record only some very average coronal conditions. By contrast, our observations are strictly simultaneous, and demonstrate that the ratio of nonthermal to thermal coronal emission reaches an approximately constant value, albeit with some scatter due to differing activity states of the star.

Table 18 summarizes the EUV/SXR flares observed, in terms of the behavior displayed in the other spectral regions involved in the campaigns. In addition to the 17 flares summarized there, there were five radio flares that were not associated with UV or EUV/SXR flares: Three did not have UV or EUV/SXR coverage (1993 September 14.7, 15.3, and 16.4). During the other two, on 1996 September 3.5 and 1998 September 11.5, there was no apparent EUV enhancement. For three events where a radio flare and EUV/SXR flare were coincident (discussed in more detail in §6.3), we estimated the peak flare luminosity and flare energies at 3.6 cm and in the EUV/SXR, by subtracting off an estimate of the quiescent luminosity from the light curve. Due to the poor time sampling of some of the data, we fitted functional forms to the pattern of emission vs time, (e.g. linear rise, exponential decay), and used that representation to estimate the amount of energy radiated during the flare. The ratio of peak EUV flare luminosity to peak radio luminosity is given in Table 19, and shows a similar range as the ratios determined from apparent quiescence, above.

Despite the limited coverage of any given flare with the suite of telescopes employed in these campaigns, we still can investigate rough statistics of correlation in the radio, UV, EUV, and SXR bands. There were five EUV/SXR flares that had partial UV coverage, and all showed some kind of enhancement in the UV. The response of the Mg II line fluxes and C IV line fluxes is similar in three cases; but for the other two, only the higher temperature C IV emission shows an increase. There were five SXR flares that had EUV coverage, but only two showed an enhancement in the EUV. Eight EUV/SXR flares had radio coverage during the flare rise; of these, three showed radio bursts (one EUV flare is a relatively small enhancement above the quiescent count rate, and could be counted as an additional EUV/radio flare coincidence). There were a total of ten 3.6 cm radio flares: Five were associated with EUV/SXR flares, while two had EUV/SXR coverage but there was no rise in high energy thermal flux.

The start of the rise phase in EUV/SXR flares is generally when the impulsive UV and 3.6 cm radio flares occur, as demonstrated in Figures 25, 26a, 26b. The UV and radio radiation show a sudden increase then decay at this point. The radio emission originates from gyrosynchrotron emission from accelerated particles; the abrupt change in behavior suggests an increase in the number of radiating particles, increase of magnetic field strength, or possibly a change in the distribution of the nonthermal electrons. The correlation of UV flux with radio flux suggests that the transition region (C IV) and sometimes the chromosphere (Mg II) are heated by nonthermal particles impinging from the corona. The trend of Mg II fluxes with radio emission is less clear. For the EUV flare that peaked on 1993 September 17.4, both C IV and Mg II showed a peak during the rise of the EUV flare. In subsequent

EUV/SXR flares, however, there was no response from Mg II, in contrast to the behavior illustrated by C IV.

Radio variability is more common at 20 cm than at higher frequencies. Section 4.2 showed that negatively polarized bursting behavior at 20 cm happened about 30% of the time HR 1099 was observed. Figures 26a, 27, 28 compare the flux and polarization behavior at 20 cm to the variations of the thermal plasma in the EUV and SXR. One might expect a higher association rate between 20 cm bursts and EUV/SXR flares, since both appear to occur frequently. Such an assessment is difficult to make, due partly to the gaps in time coverage between the two wavelength regions, and the lack of any structured behavior at 20 cm, compared to the more or less orderly rise and decay of the largest EUV/SXR flares. There are several instances when the 20 cm radio flux appears to maintain a large value of LCP for several hours: 1994 August 24.7–25.0, 1994 August 27.4–27.7, 1996 September 3.3–3.9, 1998 September 8.8.3–8.9, 1998 September 10.5–10.7, and 1998 September 11.4–11.7. At these times there are few EUV flares, but also many gaps in EUV coverage, so it is difficult to determine the association rate.

The DEM distributions for the thermal EUV/SXR emission generally has two peaks, one at 6–8 MK (0.5 keV) and the other at 20–30 MK (1.7–2.6 keV). If we make the assumption that the extent of the 3.6 cm gyrosynchrotron radio emission during these flares is about the size of the primary, as found by Lestrade et al. (1984) during a strong radio flare (θ =0.9 mas), we can estimate the brightness temperature and energy of the electrons producing the gyrosynchrotron radiation. For the four EUV/SXR flares accompanied by 3.6 cm radio bursts, the peak radio fluxes imply electron energies between 70 and 200 keV, well above the energies of the thermal electrons. These electron energies are accessible with the hard X-ray telescopes on board *RXTE* and *BeppoSAX*, but no detectable hard X-ray emission was seen by either satellite.

6. Discussion

6.1. Emission Mechanisms for Radio Bursts

The 3.6, 6, and 20 cm bands have the most extensive overlap of the five frequencies used in our radio observations. Generally, flares are most obvious at 3.6 and 20 cm. Often, variations at 3.6 cm are repeated by variations at 6 cm, but the bandwidth does not generally extend to 20 cm. Emission at 3.6 and 6 cm is consistent with gyrosynchrotron emission, which is expected to be relatively broadband: the approximate expressions in Dulk (1985) cover an order of magnitude range in harmonic number s of the electron gyrofrequency. Thus, one would expect to be able to observe gyrosynchrotron emission from a homogeneous source at both 3.6 and 20 cm. Nondetection of flaring emission at 20 cm could be due to opacity effects, if the emission were optically thick, or due to a cutoff in the emission due to a high ambient density in the flaring region. Alternatively, the lack of correlation between flaring at these two frequencies could be due to a different emission mechanism operating at lower frequencies.

The persistent nature of gyrosynchrotron emission from accelerated particles in active binaries in a steady state is puzzling, and investigations have attempted to explain the observed patterns of flux and polarization with various models. Chiuderi Drago & Franciosini (1993) attempted to explain the quiescent radio emission as the long-timescale decay of flares, (episodic acceleration of electrons), in a dipolar magnetic field configuration. They followed the change in time of the flux spectrum due to decay of a flare, including collisional and radiative losses of an initially power-law distribution of electrons. The spectrum at the time of peak flux had a positive slope from 1–5 GHz, becoming negative for larger frequencies. As losses changed the shape of the electron distribution with energy, the spectrum evolved to a decreasing function of frequency from 1–30 GHz. A three-dimensional dipole field was applied by Jones et al. (1994), who calculated both the flux and polarization spectra resulting from gyrosynchrotron radiation. Jones et al. found it difficult to reconcile the flat flux spectrum with a changing polarization spectrum. Their geometry was a thin shell of radiating electrons of width ~ 0.1 $R_\star$ at 1.9–2 $R_\star$ in an arcade of magnetic loops, with a continuous injection of accelerated particles to maintain the electron distribution against radiative losses. In order to produce a flat flux spectrum, as was observed from their quiescent data, the nonthermal electron density must increase with radius. Jones et al. (1996) examined the VLA and ATCA observations from 1993 and 1994 also presented here. They interpreted the data in light of the 3D model presented in Jones et al. (1994). They argue that the increasing trend of polarization with frequency is indicative of a change from optically thick gyrosynchrotron emission at low frequencies to optically thin radiation at high frequencies. However, White & Franciosini (1995) note in their observations of active binaries that the increasing trend of polarization with frequency is independent of the shape of the flux spectrum, contrary to the expectations from homogeneous sources (Dulk 1985).

Figure 8 displays examples of flux and polarization spectra during the decays of high frequency radio flares. The flux spectrum is increasing at low frequencies, but turns over at higher frequencies, with a maximum between 2 and 5 GHz. This behavior is consistent with optically thick emission at low frequencies and optically thin conditions at high frequencies, a pattern that has been seen during the rise and peak of flares on other active binaries (Feldman et al. 1978; Klein & Chiuderi-Drago 1987; Torricelli-Ciamponi et al. 1998). In the limits of small and large optical depth, the frequency dependence of the effective temperature and absorption coefficient can be combined to estimate the range of spectral indices α between flux measurements at adjacent frequencies. For a homogeneous source in a vacuum, the spectral index α should depend on the power-law index of the electron distribution function, δ, as (Dulk 1985):

$$\begin{aligned} \alpha_{\tau\gg1} &= 2.5 + 0.085\ \delta && \text{(6-1)} \\ 2.7 \leq \alpha_{\tau\gg1} \leq 3.1 & \quad \text{for}\ \ 2 \leq \delta \leq 7 \\ \alpha_{\tau\ll1} &= 1.2 - 0.895\ \delta && \text{(6-2)} \\ -5.1 \leq \alpha_{\tau\ll1} \leq -0.6 & \quad \text{for}\ \ 2 \leq \delta \leq 7. \end{aligned}$$

The spectral indices listed in Table 5 in the 1–5 GHz range are generally flatter than these limits on the spectral index, implying that a shallower distribution is required ($\delta \leq 2$, and out of the range of validity of the formulae in Dulk), the source is inhomogeneous, or the magnetic field varies spatially. Torricelli-Ciamponi et al. used a similar method as Chiuderi Drago & Franciosini (1993) to model the flux spectrum, but examined the rising phase of flares, and determined that a continuous supply of relativistic electrons and loss mechanisms was necessary.

The radio flares at 3.6 and 20 cm generally have quite different characteristics: 20 cm bursts are very highly polarized, and display rapid flux changes (<60 s), while 3.6 cm bursts vary over longer timescales, and are consistent with little to no intrinsic polarization. This suggests a different mechanism at 20 cm, bringing us to the question of what kind of process might be operating to produce the 20 cm flares. The quantities necessary to discriminate different radio emission mechanisms are: (1) time duration of the event; (2) brightness temperature T_b; (3) sense and amount of circular polarization; (4) bandwidth $\Delta\nu$. The time duration is limited by the temporal sampling of the VLA data to be $\geq$ 10 seconds. There are large LCP fluxes that persist for long timescales, $\approx$ 5.6 hours, as well as fluctuations on smaller timescales. Often increases, peaks, and declines in flux were observed to occur with a duration $\leq$ 60 seconds. Knowledge of the brightness temperature involves an estimate of the emitting source size, which we cannot unambiguously deduce from these data. We can place a lower limit on T_b by assuming that the radio source is $\approx$ the size of the binary orbit: consistent with previous VLBI observations of quiescence in active binaries at higher frequencies (Mutel et al. 1985), and constrained by a light travel time of $\sim$ 60s (the approximate duration of the shortest individual bursts). The brightness temperature can be determined from the observed flux S_ν, at a wavelength of 20 cm, assuming a source size $\theta_{\rm mas}$ =2.5 using orbital parameters from Strassmeier et al. (1993) and references therein,

$$T_b(K) \geq 2.2 \times 10^8 \ \ S_\nu(mJy) \ . \tag{6-3}$$

The brightness temperatures of the 20 cm bursts was in the range 1–4 10^{10} K, pointing to a nonthermal process, suggesting electron energies of a few tens of MeV[8]. The high degrees of circular polarization argue for a relatively localized phenomenon, so this is a lower limit to the brightness temperature. The observed circular polarizations are very large and negative and consistent with 100% LCP emission assuming a two-component quiescent and flaring model. The polarization at higher frequencies, where the spectral indices indicate optically thin conditions, suggests X-mode emission. Since the low frequency emission has the opposite helicity, it appears to be o-mode emission, which is consistent with the hypothesis of plasma emission. O-mode plasma emission at the fundamental can be explained by the lower cut-off frequency for o-mode emission compared to x-mode (Benz 1993); polarizations can reach quite high levels. We can place rough limits on the bandwidth by comparing the behavior at 20 cm with that at 13 or 6 cm. From a lack of correlation with higher frequency data, the bandwidth must be smaller than $\approx$ 988 MHz. The difference in flux behavior in the two intermediate frequencies of the VLA L band receiver also constrains the bandwidth of the phenomenon. The two IFs span 50 MHz centered on 1385 and 1465 MHz respectively. The bottom two panels of Figure 7 compare the behavior in these two IFs during some 20 cm bursts. From 1994 August 27.525–27.533, the higher frequencies dominated in flux, although the temporal pattern of both IFs is similar, suggesting $\Delta\nu \geq 130$ MHz. On 1994 August 28.372–28.380 the lower IF dominates in flux initially, followed by a change to higher frequency dominating at the end of the burst event, suggesting that the bandwidth was smaller than 130 MHz. The differential frequency information available in the two IFs from these continuum observations is not enough to pin down the bandwidth; finer spectral binning must be used, such as available with the Arecibo telescope, the Green Bank Telescope, or the expanded VLA.

Highly polarized, short time duration events have been observed on the Sun, although generally at lower frequencies than seen here. The metric and decimetric solar radio bursting and spiky emission is usually attributed to plasma radiation at the fundamental or second harmonic of the plasma frequency ($\nu \sim s\nu_p$, s=1,2). This emission is associated with electron beams, and results from the conversion of electron beam-excited coronal plasma waves into plasma radiation. Table 1 of Dulk (1985) summarizes the characteristics of solar radio bursts. Some bursts display analogous behavior to that seen here. Type I bursts have brightness temperatures $> 10^{10}$ K and are highly polarized in the sense of the o-mode. However, they tend to occur at much lower frequencies ($\nu \leq$ few hundred MHz), and can have very

---

[8]If the emission mechanism is coherent, with particles radiating in phase, the average energy implied by the brightness temperature can be greater than the energy of a single particle. Thus this may be an upper limit to the actual electron energy.

small bandwidths $\Delta\nu \approx 1$ MHz and last for one second at most. Solar radio continuum emissions have been observed which are relatively long-lived, highly polarized, and show large polarizations in the sense of the o-mode; an example is type IV storm continuum. Isliker & Benz (1994) have catalogued solar flare radio emission from 1–3 GHz, and give examples of type IV bursts which last for minutes, modulated on timescales less than 10 seconds, and are strongly polarized.

The two main mechanisms which have been proposed to explain similar behavior in dMe flare stars are plasma radiation or emission from an electron-cyclotron maser instability. Both interpretations suffer from uncertainties in the model parameters, and imprecise knowledge of stellar atmospheric structure. Plasma emission can occur at the fundamental or second harmonic of the plasma frequency ($\nu_p \approx 9\sqrt{n_e(cm^{-3})}(GHz)$), while emission from an electron cyclotron maser instability generally occurs at the fundamental or harmonics of the electron cyclotron frequency ($\nu_B \sim 2.8B(G)$ MHz). These parameters depend on the electron density n_e and magnetic field strength B, whose variation with height (for the case of a homogeneous, stratified atmosphere) or relative changes in inhomogeneous structures are not known. Often only a single coronal electron density or photospheric magnetic field strength measurement exists; it is difficult to infer whether spatial regimes in the stellar upper atmosphere favoring either mechanism exist. Additional complicating factors include the propagation and escape of the radiation once it has been generated: for example, o-mode plasma emission at the fundamental frequency can explain the large values of percent left circular polarization, but this radiation experiences strong free-free absorption due to the high inferred electron densities. Similarly, fundamental radiation from electron-cyclotron maser emission experiences large amounts of gyroresonant absorption, due to the high inferred magnetic field strengths. A coronal loop provides a natural set-up for a magnetic mirror and resulting loss-cone distribution; however, recent research on auroral kilometric radiation (AKR) which invokes a cyclotron maser emission mechanism has shown that a shell maser configuration is more appropriate in this situation (Ergun et al. 2000). A shell maser in a stellar corona would allow the source to be located higher in the corona due to a more moderate requirement of the magnetic mirror ratio. In addition to these two possibilites, Bastian (1996) has proposed some exotic mechanisms to explain the extremely high brightness temperature phenomena observed in dMe flare star coronae.

Without better temporal and frequency resolution, it is impossible to discriminate amongst these two coherent emission mechanisms in the observational data. The hours-long highly LCP emission could be an envelope of thousands of short duration bursts (≤ 10 s) overlapping each other, or it could be diffuse continuum emission. White & Franciosini (1995) suggested the solar analogy of type I noise storms (Kai et al. 1985) to explain this phenomena: a superposition of type I bursts with bandwidths of about 100 MHz is consistent with the data here. Similarly, continuous pumping of free energy into the maser from a parallel electric field could explain the long duration of large negative polarization. The smaller timescale bursts could be due to pulses from the maser. The high coronal temperatures ($T \geq 10$ MK) found in HR 1099 and other active binary systems could reduce the free-free absorption that would result from fundamental plasma emission (free-free absorption coefficient $\sim n_e^2/T^{1/2}$) and explain the higher frequencies where the stellar emission is found, compared to the lower temperature solar corona. The evidence from high energy spectra for high coronal electron densities ($n_e > 10^{12}$ cm^{-3}) suggests there must be extreme density inhomogeneities, however; otherwise the high inferred electron densities would obliterate any effect of high temperatures in reducing the free-free opacity. One of the requirements for generating the electron-cyclotron maser is the condition of a low density plasma, $\nu_p/\nu_B \leq 1$. We do not have exact knowledge of the spatial variations of the electron density or magnetic field in the coronal environment of HR 1099. The situation is made more complicated by the presence of two stars, and possible intrabinary emission. We can make estimates for plausibility arguments. Taking a base coronal electron density of 10^{12} cm^{-3} (see § 4.3.2), a base magnetic field of ≤ 1000 G as determined from Zeeman Doppler imaging (Donati et al. 1990), and estimates for the density scale height and magnetic scale height using the parameters for the K1 IV primary, the plasma frequency always exceeds the electron gyrofrequency:

$$\frac{\nu_p}{\nu_B} = (4\pi m_e c^2)^{1/2} \frac{n_0^{1/2}}{B_0} e^{r(\frac{1}{H_B} - \frac{1}{2H_n})} \tag{6-4}$$

assuming $n(r) = n_0 e^{-r/H_n}$ and $B(r) = B_0 e^{-r/H_B}$, for $H_B \leq H_n$; the density scale height H_n at 10^7 K is 5.6 10^{11} cm, or approximately twice the radius of the K1 subgiant. This assumes a homogeneous coronal plasma: The existence of extreme density inhomogeneities could make conditions more favorable for the electron-cyclotron maser.

6.2. DEM Analysis and Abundances

The temperatures and abundances of the coronal plasma in HR 1099 can be diagnosed in both the EUV (*EUVE*) and X-ray (*ASCA, RXTE, BeppoSAX*). The EUV spectra permit identification of individual emission lines, while X-ray spectra show only broad "humps" of emission line complexes and the underlying continuum. Here we discuss the different analyses and their different views of the coronal structure in HR 1099.

Figure 17 compares the differential emission measures derived from *EUVE* spectra for quiescent and flaring conditions in 1993 and 1996, to discern plasma changes before and during a flare. The same basic shape exists in all the DEMs at temperatures hotter than ≈ 5 MK. The flare intervals are integrated over changing plasma conditions n_e, T_e, and V during the flare itself, so a comparison with the quiescent DEM only yields information about the "average" DEM during a flare. There is also a contribution from quiescent emission to these DEMs, since no estimate of the quiescent spectrum was subtracted from the flare spectra. The flare DEMs plotted in Figure 17 have had the quiescent DEM subtracted from them, to get a sense of the changes that occur in the temperature distribution during the flare. During the flares there is a large amount of hot plasma, T$\geq$ 15 MK, over and above the amount present outside of flares. There is also a significant enhancement in plasma at 6–9 MK during flares. For time intervals where Fe XV and XVI are detected, there is a large drop from the DEM at $T \geq 5$ MK to lower temperatures, showing a minimum around $T =$ 3 MK and rising to a small maximum around $T = 1.6$ MK. The DEM shows evidence of increasing at high temperatures, T$\geq$ 30 MK, beyond which the line diagnostics in the *EUVE* spectra are not sensitive.

Portions of the *EUVE* data have been examined by others. Griffiths & Jordan (1998) performed an analysis of the 1993 and 1994 spectral datasets, without performing time-resolved spectroscopy, despite the fact that several large flares occurred during these observations. They determined that bremsstrahlung continuum was minimal, and determined the fluxes of emission lines in the spectra by using a "local continuum" level. Griffiths & Jordan calculated the emission measure distribution using temperature bins of $\Delta \log T$ =0.3, and emissivities calculated at varying electron densities. They find a peak at $\log T$ =6.9, a decrease in the EM and subsequent increase to hotter temperatures for $\log T \geq 7.1$. For comparison with X-ray spectra, which have overlapping temperature sensitivities, Griffiths & Jordan examined EXOSAT medium energy proportional counter and low energy imaging telescope data, fitted using one or two discrete temperatures. The maxima in the *EUVE* emission measure distributions match those found from the 1T or 2T X-ray fits. Sanz-Forcada et al. (2002) also examined the *EUVE* spectral data of all observations from 1992–1999, accumulating one quiescent and one flare spectrum from all individual quiescent and flare time segments, and derive emission measure distributions for these and a spectrum summed from all *EUVE* exposures of HR 1099, regardless of activity. In their spectral analysis, they subtract a local continuum determined by visual inspection from the spectral data. The general results of Sanz-Forcada et al. are consistent with those found in Griffiths & Jordan (1998) and also found here for the separate time intervals: There is a small peak at $\log T$ =6.3 (due to emission from Fe XV and XVI) and another, larger peak at $\log T$ =6.9. For hotter temperatures, the emission measure decreases and subsequently rises to hotter temperatures up to $\log T$ =7.5, above which *EUVE* spectral data become insensitive.

The fundamental problem in dealing with *EUVE* spectra is the lack of sufficient information to constrain all the quantities that characterize the coronal plasma: The key amongst them being elemental abundances, and hence continuum emission in the spectrum. The general trends reported by the above authors are consistent with the distribution of plasma with temperature derived here from *EUVE*.

The *ASCA* analysis has used the MEKAL plasma code, allowing the abundance of each element (O, Ne, Mg, Si, S, Ar, Ca, Fe and Ni) having strong emission lines in the 0.6–10 keV region to vary independently of each other. Due to the low spectral resolution of the CCDs, some of these abundances are compromised because of severe line blending (the oxygen abundance is suspect due to calibration problems). The analysis of *BeppoSAX* spectra is simplified to discrete multiple temperatures, and an abundance scaling Z. The presence of emission lines from multiple ionic species, and the high energy sensitivity, allows the X-ray spectra to constrain temperatures, abundances, and the continuum level; in practice, due to the low resolution, some of these quantities are entangled.

The low iron abundance during the quiescent *ASCA* observation (Fe/H$\sim$0.12) is apparently incompatible with the observed *EUVE* flux obtained simultaneously; it predicts a continuum level that is larger than the observed EUV fluxes. We took the DEM and abundances derived from the quiescent *ASCA* spectrum (described in §4.3.1) and synthesized the EUV spectrum. We compare the synthesized EUV spectrum with the composite quiescent EUV spectrum. A comparison of the DEMs derived from the *ASCA* and *EUVE* analyses shows that there are hotter temperatures present in the *ASCA* DEM compared with the one derived from *EUVE* data. The hotter plasma in the *ASCA* DEM reveals itself in the *EUVE* spectrum primarily through the continuum, and in order to match the observed EUV iron line strengths, the iron abundance can be at 0.1 times the solar abundance. This difference with the *EUVE* analysis lies in the temperature sensitivity; when there are hotter temperatures, the intrinsic continuum level is higher, and therefore the line-to-continuum ratio can be lower. Disregarding the hotter temperatures artificially depresses the estimated continuum level, necessitating a higher iron abundance. The low Z ($\sim$0.3) derived from the *BeppoSAX* X-ray spectra is consistent with the constraint on abundance determined from the composite *EUVE* spectra, where Fe/H $\geq$ 0.2; the wavelength overlap between these two instruments (*BeppoSAX*: 1.2–120 Å; *EUVE*: 80–370 Å) ensures that a consistent picture can be obtained. Analysis of other low resolution X-ray spectra yield similar results to those found here: Drake et al. (1996) investigated Einstein, EXOSAT, and ROSAT spectra with 2T variable abundances and found a low temperature component at $\sim$ 0.7 keV and another between 2–4 keV, with some variability. The abundance Z was always subsolar, between 0.4–$\leq$0.9 solar, and variable. Drake & Kashyap (1998) investigated the *ASCA* data presented here; however, they did not do a time-resolved spectral analysis, and kept the abundances scaled to a common Z. Their 2T fit agrees with our results, but their Z is $\approx$ 0.4 solar; their data, however, include quiescent and flare intervals (as discussed in §4.3.1). This could account for why their Z is higher than the individual abundances derived here for quiescent and flaring intervals. We mention that the abundances derived by *ASCA* and *BeppoSAX* are in good agreement with the iron photospheric abundance of ~ 0.2 solar derived for the K star by Randich et al. (1993).

In more recent years, HR 1099 has been observed by *Chandra* and *XMM-Newton* (Drake et al. 2001; Audard et al. 2001, respectively). The *XMM-Newton* observation included a large flare. The analysis by Audard et al. of the 7–35 Å *XMM-Newton* spectral region in quiescence utilized a similar technique to that performed here: They used four discrete temperature components (compared to the two in the present analysis of *ASCA* data) using the plasma code SPEX. The abundances derived during the quiescent interval are remarkably similar to those found for the quiescent interval of the present analysis: The abundance of iron relative to the solar photospheric abundance of Anders & Grevesse (1989) is 0.15 ± 0.02, very close to our derived values from analyses of SIS0, SIS1, and GIS2 spectra of 0.12 ± 0.04 from Table 12. Abundances of other elements are similar in the *ASCA* and *XMM-Newton* observation, but due to the differing wavelength coverage and sensitivity, the iron abundance is the more important to compare since in principle it can be determined more accurately. The large flare captured by the *XMM-Newton* observation also revealed an enhancement in the iron abundance, about a factor of three compared to the quiescent value. The continuous emission measures Audard et al. determined using the coronal abundances from discrete temperature fitting imply a broad plateau of emission between 6–30 MK during quiescence, and during the flare there is a high temperature peak at 40–50 MK, along with a secondary peak at $\approx$ 6 MK as in quiescence.

In contrast to the varying behavior seen in the *XMM-Newton* observation, the *Chandra* HETG observation showed no evidence for flares (Ayres et al. 2001a). Drake et al. (2001) analyzed the spectrum to determine DEM and abundances. The DEM showed a broad peak from $\log T$ =6.8–7.4, with a minimum at $\log T$ =6.6 and rise towards cooler temperatures. They determined abundances of O, Ne, Mg, Si, S, and Ar relative to the iron abundance, expressed in relation to the solar photospheric abundances of Anders & Grevesse (1989) for the elements O, Ne, Mg, Si, S, and Ar, and the photospheric iron abundance of Holweger et al. (1991). The use of a different value for the solar photospheric iron abundance makes a cross-comparison difficult, but they determined that the iron abundance was depleted in the coronal spectrum, by about a third relative to the solar photospheric abundance; the coronal abundances of O, Mg, Si, and S are slightly subsolar, whereas the noble gases Ne and Ar are enhanced by factors of several over the solar photospheric values.

6.3. The Neupert Effect

The time delays observed between radio and EUV/SXR flares are in the same sense as expected from the solar analogy, but the scale of the delays is much larger (hours compared with minutes in the solar case). There is an inherent difficulty in causally connecting behaviors based solely on temporal associations. We can take the solar case as an example, and use expectations from solar observations coupled with a theoretical physical connection between emitting mechanisms.

The Neupert effect is the observed correlation in solar flares between the time-integrated radio/HXR light curve and the SXR light curve during the rising phase of the latter (Neupert 1968); alternately, between the radio/HXR light curve and the time derivative of the SXR light curve. This observational association can be explained using the chromospheric evaporation theory, in which the HXR emission is thick-target nonthermal electron-ion bremsstrahlung (Li et al. 1993) and the microwave radiation arises from gyrosynchrotron emission from electrons trapped in a magnetic loop. Most of the energy contained in the nonthermal particles is lost by Coulomb collisions with the ambient plasma in the chromosphere. The chromospheric material at the particle impact site undergoes a radiative instability and can be heated to coronal temperatures (T$>10^6$ K) on a timescale short compared with the hydrodynamic expansion time. The resulting overpressure of the plasma causes it to fill the coronal loop where it radiates thermal soft X-ray emission. This is the "explosive evaporation" model of Fisher et al. (1985).

There have been numerous studies of the Neupert effect in solar flares, and the results are contradictory. Dennis & Zarro (1993) found that the Neupert effect relationship between the soft X-ray time derivative and the hard X-ray emission holds for 80% of impulsive solar flares; events that vary more gradually show a poorer correlation. McTiernan et al. (1999) demonstrated from an analysis of the DEM during solar flares that the Neupert effect is more likely to be seen in higher temperature plasma than at low temperatures, suggesting that the bandpasses of the soft X-ray observations may skew sensitivity to this effect. Hawley et al. (1995) observed the flare star AD Leo using *EUVE* and optical observations, and found a correlation between the two suggestive of a Neupert effect. The optical emission, which serves as a proxy for nonthermal radiation due to electron beam impingement on the stellar photosphere, reaches a peak during the rise of the EUV flare: The time integral of the U band luminosity matches the evolution in EUV count rate during the rise phase. Güdel et al. (1996) investigated radio and X-ray observations of flares on a dMe flare star, finding evidence for a Neupert effect; and most recently, Güdel et al. (2002) found evidence of the Neupert effect in the active binary σ Gem.

We investigated evidence for the Neupert effect in the cases where a radio burst occurred during the rise phase of an EUV/SXR flare. Güdel et al. (1996) constructed a simple model, which we follow here, for the rate of change of the energy content of a volume V of thermal plasma at temperature T and density n_e: a source of energy is provided by heating, presumed to originate from the nonthermal energy input as diagnosed by the radio emission, and energy is lost by radiation. This equation can be written

$$\frac{d}{dt}(3n_e kTV) = \alpha F_R - n_e^2 V P_\lambda(T) \tag{6-5}$$

(equation 1 Güdel et al. 1996) where k is Boltzmann's constant, αF_R gives the amount of nonthermal energy deposition, and $P_\lambda(T)$ is the radiative loss function for optically thin, high temperature thermal plasmas (Mewe et al. 1985). Using a constant radiative time scale $\tau = \frac{3kT}{n_e P_\lambda(T)}$, and neglecting any initial energy content, an analytical solution is :

$$E(t) = \alpha \int_{t_0}^{t} F_R(u) e^{-(t-u)/\tau} du \tag{6-6}$$

and the observed luminosity $L(t) = E(t)/\tau$. The equivalent expression for the classical Neupert effect is

$$E(t) = \alpha \int_{t_0}^{t} F_R(u) du \quad , \tag{6-7}$$

which is the first solution, in the limit of infinite τ. The analyses of the data (Sections 4.3 and 4.4) have been able to constrain density and temperature, but only in a general way; i.e., we can characterize the overall quiescent-flare and flare-flare changes of the plasma, but not a detailed characterization of the plasma evolution during the flare. In reality, the density and temperature will be changing during the course of the flare. In addition, two of the large EUV flares which had accompanying radio flares during their rise (1994 Aug. 26.5–28, 1996 Sept. 7–11) had complex morphologies during the flare rises and decays (for 1996 Sept. 7–11 the radio coverage extended over only $\approx$ 10 hours, compared with the 83.6 hour duration of the EUV flare), making an interpretation in terms of the Neupert effect difficult. The *ASCA/EUVE* flare on 1994 August 25.6–26.0, however, has a relatively simple shape, and we investigated it in detail. Figure 29 shows the flare variation of the thermal plasma in the SXR and EUV bands, along with the radio flare. Estimates of the quiescent emission have been subtracted from all three light curves. We fitted the radio light curve with a linear rise and exponential decay, then used that function to perform the integrations discussed above. The radiative decay timescale τ of 6000 seconds was chosen to match roughly the observed soft X-ray flare decay: this timescale is appropriate for a temperature of 10^7K and $n_e \sim 10^{11}$ cm^{-3}. The agreement with the observed soft X-ray profile is decent, indicating that the chromospheric evaporation scenario is applicable to stellar flares. Table 19 lists the peak luminosities, integrated energies, and flare durations, for the three EUV/SXR flares which showed a radio burst during the flare rise. The L_X/L_R (and L_{EUV}/L_R) ratios have a similar range to those tabulated during quiescent intervals in Table 17, and are comparable in magnitude to the results from Güdel & Benz (1993) for quiescent X-ray and radio emission from a sample of active stars and solar flares. This could suggest a common heating mechanism for quiescent and flaring coronal plasma.

We also call attention to the EUV flare of 1993 September 17.4, where there was a gap in the radio coverage but UV coverage was available from *IUE*. The UV fluxes of C IV and Mg II peak near the start of the EUV flare rise, in a pattern similar to that seen with several radio flares. Solar flare UV radiation shows a close temporal and spatial association with hard X-ray emission (Cheng 1999) — The interpretation is that the chromospheric and transition region material is directly heated by the nonthermal particles, so that the increase in intensity of these lines traces the nonthermal energy input. The close association between UV and radio fluxes is clearer in the flare on 1994 August 27.0, where both are seen to be rising at the start of the EUV flare rise.

6.4. Flare frequency

Several flares were detected with multiple EUV/SXR telescopes, and show a general trend in the amount of contrast between the flare peak and surrounding "quiescent" level: A larger response is seen at the harder energies. In several cases, the enhancement in the EUV light curve is consistent with the level of quiescent variations, and only by examining the flare in a multi-wavelength context can hints of flare emission in the EUV be recognized. The salient flares are those on 1994 August 25.76, 1996 September 4.8, 1998 September 7.9, and 1998 September 9.8. While the SXR light curves exhibit enhancements of 2–3 over the level outside of the flare, the EUV light curve typically shows variations at the level of 20–30%. This suggests that lower energy bandpasses will be insensitive to all but the most energetic flares. Unfortunately, none of the large EUV flares were observed in the SXR; we expect the flare contrast would have been huge.

In Osten & Brown (1999) the flare frequency was determined for a sample of active binary systems that were observed with *EUVE*. After consideration of the poor flare contrast in the EUV, it is possible that those flare frequencies were underestimated. The most extreme example of this is illustrated by the *EUVE* observations in 1998. The light curve of EUV variations in Figure 9 shows only one moderate flare noticeable during an observation spanning 8.7 days. We noted in Section 4.3.1 that there was a sudden shift in activity from the behavior displayed in the 1993–1996 observations and that illustrated in 1998. Inspection of the *BeppoSAX* and *RXTE* light curves in Figure 28 show that there are roughly five more flares, in addition to the one obvious in the *EUVE* light curve. Based on the *EUVE* light curve, we would have concluded that the flare frequency was $\sim$ 0.1 day^{-1}; using the multi-wavelength light curves, we would infer a much higher rate, $\sim$ 0.7 day^{-1}. Feldman et al. (1995a) examined a sample of solar flares spanning four orders of magnitude in peak emission measure, and found an almost power-law dependence between the peak emission measure ($\sim$ peak luminosity) and the peak flare temperature, with a steep dependence (EM$\propto$T^5). Feldman et al. extrapolated the results to a few of the largest stellar flares which had been reported in the literature. This relation implies that larger flares are also hotter, which would skew the flare spectral energy distribution to harder photon energies, and explain the apparent discrepancy between the *EUVE* flare enhancements and the *RXTE*/*BeppoSAX* flare enhancements.

Güdel et al. (2003) examined the flare rate distribution on the M dwarf flare star AD Leo using simultaneous *EUVE* and *BeppoSAX* LECS and MECS light curves in combination with model-flare-synthesized light curves generated assuming a power law distribution of flares with energy. They found a systematic flattening of the derived distributions generated using the harder energy MECS data, compared with the *EUVE* and LECS detector data. They interpreted this skewing as due to the harder energy range of the MECS detector, and the increasing peak temperatures of more luminous flares. The softer bandpasses are more sensitive to quiescent emission. Such a statistical treatment of flare rate distributions will be less biased than simply counting individual large flares. Harder X-ray bandpasses are more favorable, however, for investigating the temperatures involved in large stellar flares.

7. Conclusions

There are several conclusions to be drawn from such a broad investigation of flaring on the active binary system HR 1099.

One of the surprising results obtained from radio observations is how common bursts at low frequencies are on HR 1099 – occurring roughly one third of the time. We have investigated the nature of L-band bursts, and find that they are characterized by emission that can achieve large values of percent left circular polarization ($\rightarrow$ 100%), is highly variable (possibly varying on timescales less than the 10 second integration time of the VLA observations) and long-lasting (attaining high flux levels and high degrees of left percent circular polarization for hours). Due to an inability to constrain the source size of these bursts, only a moderate lower limit on the brightness temperature, $T_b \geq 10^{10}$K, can be determined. Such brightness temperatures could be consistent with incoherent gyrosynchrotron emission; coupled with large values of circular polarization, short timescales and apparent lack of similarity with higher frequency variations, however, it is more likely that this phenomenon is an example of a coherent mechanism. Determining what mechanism might be operating in the coronae of HR 1099 requires observations with better time resolution (to constrain the source size), and larger frequency coverage (to determine the bandwidth of the emission).

The characteristics of X-ray and microwave emission from active binary systems and dMe stars share similarities. The thermal coronal emission from both is characterized by electron temperatures T_e of 5–30 MK, high densities ($n_e \approx 10^{12}$ cm^{-3}), and coronal abundances that are subsolar in quiescence and appear to vary during flares. Centimeter-wavelength radio emission is generally attributed to nonthermal gyrosynchrotron radiation outside of flares (Gudel & Benz 1996). The phenomena observed on HR 1099 at 20 cm reported here, and on other active binary systems reported by others, has parallels with behavior on dMe stars: in both cases, there is evidence for highly polarized and time variable emission (dMe star behavior shows evidence for fast fluctuations [$\Delta t \leq 20$ milliseconds] and extremely high brightness temperatues, [$T_b \geq 10^{16}$K]). Constraining the observational properties of these low-frequency bursts on active binary systems will reveal the extent of the apparent similarity in dynamics of these two kinds of coronal environments.

Radio observations show several large flares at 3.6 cm. The increase of flux and decrease of polarization during 3.6 cm flares is consistent with a constant quiescent level in intensity and polarization and a flare which increases in flux but remains unpolarized. The 6–3.6 cm spectral indices during the flares show an increase during the flare rise, attaining the largest value as the flux reaches its maximum value (see also Richards et al. 2003). This behavior is consistent with an increase in optical depth during the flare rise, and also consistent with little or no circular polarization during the flare; it is difficult to obtain large values of circular polarization under optically thick conditions. The behavior of the radio flux spectra illustrate the general trends of active binary gyrosynchrotron emission: Spectral indices are flat or slightly negative during quiescence, and show a peak between 2 and 5 GHz during flares. The observed polarizations always increase with frequency, regardless of the behavior of the flux spectra with frequency (as also discussed in White & Franciosini 1995).

There were no definite detections of HXR emission at energies larger than > 12 keV during or outside of flares. Yet the radio fluxes indicate the existence (and persistence) of accelerated particles. To date, there have been only a few detections of hard X-ray (20–50 kev) emission by *BeppoSAX* at the peak of very strong flares (Favata & Schmitt 1999; Maggio et al. 2000; Pallavicini 2001; Franciosini et al. 2001). This HXR emission however has been interpreted as thermal emission due to the very high temperatures (T $\sim 10^8$ K) reached in these flares. Our *BeppoSAX* PDS observation of HR 1099 gives only an upper limit to hard X-ray emission which is two orders of magnitude lower than the soft X-ray emission.

The fact that no HXR emission has been detected by either *RXTE* or *BeppoSAX* is due to the fact that the temperatures reached by the observed X-ray flares on HR 1099 are much lower than those needed (about 100 MK) for thermal hard X-ray emission; and secondly, to the fact that the nonthermal electrons indicated by the radio observations are apparently insufficient to produce detectable non-thermal hard X-ray emission (as is also true for the Sun where the ratio of non-thermal to thermal hard X-ray emission in impulsive solar flares is $\geq 10^{-5}$).

Flares lasting several days appear to be a common feature on active stars. Such long-duration flares have now been detected not just on active binary systems (Kuerster & Schmitt 1996), but on active evolved single giant stars (Ayres et al. 1999, 2001b) as well as higher gravity dMe flare stars (Cully et al. 1994). A feature common to many of these flares is the presence of a change in the light curve decay phase, from an initially fast decay to a slower decay. Several flares on HR 1099 discussed in this paper also show evidence for such decay morphologies. Unfortunately, the sensitivities of the EUV and SXR telescopes which observed these flares are not sufficient to determine the change of plasma parameters (n_e, T_e) with time during the decay phase; usually only a gross estimate of the total flare changes with respect to quiescent intervals is possible. This renders an interpretation of the underlying cause of the observed decay change difficult: a change to low-density structures during the late stages of the decay could explain the long decay timescales. Another viable explanation is the presence of continued heating during the decay (e.g. Favata & Schmitt 1999). A possible clue may come from studying solar flares; a few long-duration solar events (e.g. Feldman et al. 1995b) appear to possess a break during the decay, similar to the behavior seen in stellar long-duration events.

EUVE observations reveal many flares; HR 1099 was in a high state of activity for three out of the four years it was observed during these campaigns. There is suggestive evidence of a flare precursor in four large EUV flares, consisting of a slow increase in flux before the flare rise. The dynamic range of events exhibited by HR 1099 was less than a factor of 7 in the EUV. Most flares in the EUV show a remarkable amount of symmetry between the flare rise and decay, an observation that is at odds with the fast rise and slow decay typical of chromospheric evaporation in solar flares. An investigation of the time-resolved spectral variations confirms the creation of hot plasma during flare intervals. The existence of many weak lines blended with continuum radiation in the EUV hinders spectral interpretation, particularly with regard to elemental abundances and activity-related abundance changes. This also limits the hottest temperatures to which EUVE spectra are sensitive. Densities determined from *EUVE* spectra indicate high values ($n_e \sim$ few 10^{12} cm^{-3}) during quiescence, but no evidence for a statistically significant enhancement during flares.

ASCA observations of a small flare indicate an enhancement of the iron abundances by about a factor of three between quiescence and the peak of the flare. The emission measure distribution shows the same general structure during quiescence and flares: A peak at 6–10 MK and another between 20 and 30 MK. During flares, the high temperature peak becomes more prominent and moves to hotter temperatures. The temperatures derived from *BeppoSAX* and *ASCA* spectra are generally consistent with each other; however, the small flares observed with *BeppoSAX* did not show any evidence for abundance changes. The behavior in different SXR bands as investigated with *ASCA* and *RXTE* reveal faster changes at the harder energies, indicative of hotter temperature plasma.

The multi-wavelength flare data illustrate fair correlation between EUV/SXR flares and radio/UV bursts. This can be interpreted in the light of solar flare mechanisms using the Neupert effect, where the time integral of the nonthermal radiation is proportional to the rise phase of the EUV/SXR light curve. The correspondence of radio and UV light curves suggests that the UV line fluxes also can be used as a proxy for the the nonthermal radiation impinging on the chromosphere. Three EUV/SXR flares showed a radio burst during the flare rise, with time delays between peak radio and EUV/SXR of 2.5–30 hours. These values are much larger than typical values for solar flares, where the delay is on the order of minutes. The highly polarized emission at 20 cm shows a low degree of correlation with gyrosynchrotron flaring activity at 3.6 cm. The ratios of flare luminosities in the EUV and 3.6 cm bandpasses indicate a remarkable amount of similarity with ratios derived from simultaneous observations of quiescence in the two bandpasses. This suggests that a similar mechanism which forms the quiescent thermal/nonthermal radiation is also present, at some level, in producing the time-varying flare emission. The radio and EUV flares considered here last orders of magnitude longer than typical solar flares, where nonthermal radio radiation lasts $\sim$ minutes, and EUV/SXR thermal radiation lasts $\sim$ hours. Yet, the ratios of EUV-to-radio flare duration for the three flares discussed are in agreement with the solar and stellar flares discussed by Güdel et al. (1996).

There is a noticeably greater enhancement in the flare luminosity compared with the quiescent luminosity for higher energy bandpasses. For times when EUV and X-ray observations are simultaneous, often flares are obvious in the X-ray light curve but only appear as "quiescent" modulations in the EUV. More luminous flares tend to be hotter, and thus the flare spectral energy distribution will be shifted to higher energies, and involve predominantly continuum emission; flares will then favor the X-ray spectral regions over the EUV. This can lead to a bias that lowers the observed flare frequency, and affects the distribution of flares with energy.

This work was supported by NASA grants NGT5-50241, NAG5-7020, NAG5-3226,

NAG5-2259, NSG5-4589, NAG5-2530, NAG5-7398, and NSF grant AST-0206367 to the University of Colorado. RAO is grateful for the support of a GSRP fellowship. This represents the results of VLA projects AB691, AB719, AB793, and AB874, and ATCA projects C302, C370, and C546. EF, RP and GT acknowledge partial support from the Italian Space Agency (ASI). We gratefully acknowledge Keith Jones (University of Queensland, Australia; retired) for his effort in obtaining the early ATCA observations, and Bryan Deeney for his contribution in the IUE data analysis. We thank the referee for a careful reading of this lengthy paper.

REFERENCES

Anders, E. & Grevesse, N. 1989, Geochim. Cosmochim. Acta, 53, 197

Arnaud, K. A. 1996, in ASP Conf. Ser. 101: Astronomical Data Analysis Software and Systems, ed. G. H. Jacoby & J. Barnes, Vol. 5, 17

Aschwanden, M. J. & Benz, A. O. 1997, ApJ, 480, 825

Audard, M., Güdel, M., & Mewe, R. 2001, A&A, 365, L318

Audard, M., Güdel, M., Sres, A., Raassen, A. J. J., & Mewe, R. 2003, A&A, 398, 1137

Ayres, T. R., Brown, A., Osten, R. A., Huenemoerder, D. P., Drake, J. J., Brickhouse, N. S., & Linsky, J. L. 2001a, ApJ, 549, 554

Ayres, T. R., Osten, R. A., & Brown, A. 1999, ApJ, 526, 445

—. 2001b, ApJ, 562, L83

Barstow, M. A. 1985, Space Science Reviews, 40, 35

Bastian, T. J. 1996, in ASP Conf. Ser. 93: Radio Emission from the Stars and the Sun, 447–+

Bastian, T. S., Bookbinder, J., Dulk, G. A., & Davis, M. 1990, ApJ, 353, 265

Beiersdorfer, P., Lepson, J. K., Brown, G. V., Utter, S. B., Kahn, S. M., Liedahl, D. A., & Mauche, C. W. 1999, ApJ, 519, L185

Benz, A. O. 1993, Plasma astrophysics: Kinetic processes in solar and stellar coronae, Vol. 184, Astrophysics and Space Science Library (Kluwer)

Bingham, R., Cairns, R. A., & Kellett, B. J. 2001, A&A, 370, 1000

Boella, G., Butler, R. C., Perola, G. C., Piro, L., Scarsi, L., & Bleeker, J. A. M. 1997, A&AS, 122, 299

Boggess, A., Bohlin, R. C., Evans, D. C., Freeman, H. R., Gull, T. R., Heap, S. R., Klinglesmith, D. A., Longanecker, G. R., Sparks, W., & West, D. K. 1978a, Nature, 275, 377

Boggess, A., Carr, F. A., Evans, D. C., Fischel, D., Freeman, H. R., Fuechsel, C. F., Klinglesmith, D. A., Krueger, V. L., Longanecker, G. W., & Moore, J. V. 1978b, Nature, 275, 372

Bradt, H. V., Swank, J. H., & Rothschild, R. E. 1990, Advances in Space Research, 10, 297

Brandt, J. C., Heap, S. R., Beaver, E. A., Boggess, A., Carpenter, K. G., Ebbets, D. C., Hutchings, J. B., Jura, M., Leckrone, D. S., Linsky, J. L., Maran, S. P., Savage, B. D., Smith, A. M., Trafton, L. M., Walter, F. M., Weymann, R. J., Ake, T. B., Bruhweiler, F., Cardelli, J. A., Lindler, D. J., Malumuth, E., Randall, C. E., Robinson, R., Shore, S. N., & Wahlgren, G. 1994, PASP, 106, 890

Brickhouse, N. S., Raymond, J. C., & Smith, B. W. 1995, ApJS, 97, 551

Brinkman, A. C., Behar, E., Güdel, M., Audard, M., den Boggende, A. J. F., et al. 2001, A&A, 365, L324

Brown, A., Osten, R. A., Ayres, T. R., & Drake, S. A. 1997, American Astronomical Society Meeting, 29, 807

Brown, A., Osten, R. A., Drake, S. A., Jones, K. L., & Stern, R. A. 1998, in IAU Symp. 188: The Hot Universe, Vol. 188, 215–+

Brown, A., Skinner, S., Stewart, R., Drake, S., & Deeney, B. 1994, American Astronomical Society Meeting, 185, 1463

Brown, A. & Skinner, S. L. 1996, in ASP Conf. Ser. 109: Cool Stars, Stellar Systems, and the Sun, ed. R. Pallavicini & A. K. Dupree, Vol. 9, 255

Brown, A., Skinner, S. L., Stewart, R. T., & Jones, K. L. 1996, in IAU Colloq. 153: Magnetodynamic Phenomena in the Solar Atmosphere - Prototypes of Stellar Magnetic Activity, ed. Y. Uchida, T. Kosugi, & H. S. Hudson (Kluwer), 279

Bruner, M. E., Crannell, C. J., Goetz, F., Magun, A., & McKenzie, D. L. 1988, ApJ, 334, 494

Busà, I., Pagano, I., Rodonò, M., Neff, J. E., & Lanzafame, A. C. 1999, A&A, 350, 571

Cheng, C.-C. 1999, in The many faces of the sun: a summary of the results from NASA's Solar Maximum Mission., ed. K. T. Strong, J. L. R. Saba, B. M. Haisch, & J. T. Schmelz (Springer), 393

Chiuderi Drago, F. & Franciosini, E. 1993, ApJ, 410, 301

Cully, S. L., Fisher, G. H., Abbott, M. J., & Siegmund, O. H. W. 1994, ApJ, 435, 449

Dempsey, R. C., Neff, J. E., Thorpe, M. J., Linsky, J. L., Brown, A., Cutispoto, G., & Rodono, M. 1996, ApJ, 470, 1172

Dennis, B. R. & Zarro, D. M. 1993, Sol. Phys., 146, 177

Donati, J.-F. 1999, MNRAS, 302, 457

Donati, J.-F., Semel, M., Rees, D. E., Taylor, K., & Robinson, R. D. 1990, A&A, 232, L1

Drake, J. & Kashyap, V. 1998, in ASP Conf. Ser. 154: Cool Stars, Stellar Systems, and the Sun, ed. R. A. Donahue & J. A. Bookbinder, Vol. 10, 1014

Drake, J. J., Brickhouse, N. S., Kashyap, V., Laming, J. M., Huenemoerder, D. P., Smith, R., & Wargelin, B. J. 2001, ApJ, 548, L81

Drake, J. J., Brown, A., Patterer, R. J., Vedder, P. W., Bowyer, S., & Guinan, E. F. 1994, ApJ, 421, L43

Drake, S. A., Singh, K. P., & White, N. E. 1996, in IAU Colloq. 152: Astrophysics in the Extreme Ultraviolet, ed. S. Bowyer & R. Malina (Kluwer), 147

Dulk, G. A. 1985, ARA&A, 23, 169

Ergun, R. E., Carlson, C. W., McFadden, J. P., Delory, G. T., Strangeway, R. J., & Pritchett, P. L. 2000, ApJ, 538, 456

Favata, F., Reale, F., Micela, G., Sciortino, S., Maggio, A., & Schmitt, J. H. M. M. 2001, in ASP Conf. Ser. 223: Cool Stars, Stellar Systems and the Sun, ed. R. J. Garcia López, R. Rebolo, & M. R. Zapatero Osorio, Vol. 11, 1133

Favata, F. & Schmitt, J. H. M. M. 1999, A&A, 350, 900

Feldman, P. A., Taylor, A. R., Gregory, P. C., Seaquist, E. R., Balonek, T. J., & Cohen, N. L. 1978, AJ, 83, 1471

Feldman, U., Laming, J. M., & Doschek, G. A. 1995a, ApJ, 451, L79+

Feldman, U., Seely, J. F., Doschek, G. A., Brown, C. M., Phillips, K. J. H., & Lang, J. 1995b, ApJ, 446, 860

Fiore, F., Guainazzi, M., & Grandi, P. 1999, Cookbook for NFI BeppoSAX Spectral Analysis v. 1.2, available at www.asdc.asi.it/bepposax/software/

Fisher, G. H., Canfield, R. C., & McClymont, A. N. 1985, ApJ, 289, 425

Fox, D. C., Linsky, J. L., Veale, A., Dempsey, R. C., Brown, A., Neff, J. E., Pagano, I., Rodono, M., Bromage, G. E., Kuerster, M., & Schmitt, J. H. M. M. 1994, A&A, 284, 91

Franciosini, E., Pallavicini, R., & Tagliaferri, G. 2001, A&A, 375, 196

Güdel, M., Linsky, J. L., Brown, A., & Nagase, F. 1999, ApJ, 511, 405

Gagne, M., Valenti, J., Johns-Krull, C., Linsky, J., Brown, A., & Gudel, M. 1998, in ASP Conf. Ser. 154: Cool Stars, Stellar Systems, and the Sun, ed. R. A. Donahue & J. A. Bookbinder, Vol. 10, 1484

Graffagnino, V. G., Wonnacott, D., & Schaeidt, S. 1995, MNRAS, 275, 129

Griffiths, N. W. & Jordan, C. 1998, ApJ, 497, 883

Güdel, M. & Benz, A. O. 1993, ApJ, 405, L63

Güdel, M., Benz, A. O., Bastian, T. S., Furst, E., Simnett, G. M., & Davis, R. J. 1989, A&A, 220, L5

Gudel, M. & Benz, A. O. 1996, in ASP Conf. Ser. 93: Radio Emission from the Stars and the Sun, 303–+

Güdel, M., Benz, A. O., Schmitt, J. H. M. M., & Skinner, S. L. 1996, ApJ, 471, 1002

Güdel, M., Audard, M., Smith, K. W., Behar, E., Beasley, A. J., & Mewe, R. 2002, ApJ, 577, 371

Güdel, M., Audard, M., Kashyap, V. L., Drake, J. J., & Guinan, E. F. 2003, ApJ, 582, 423

Hawley, S. L., Fisher, G. H., Simon, T., Cully, S. L., Deustua, S. E., Jablonski, M., Johns-Krull, C. M., Pettersen, B. R., Smith, V., Spiesman, W. J., & Valenti, J. 1995, ApJ, 453, 464

Heap, S. R., Brandt, J. C., Randall, C. E., Carpenter, K. G., Leckrone, D. S., Maran, S. P., Smith, A. M., Beaver, E. A., Boggess, A., Ebbets, D. C., Garner, H. W., Hutchings, J. B., Jura, M., Linsky, J. L., Savage, B. D., Cardelli, J. A., Trafton, L. M., Walter, F. M., Weymann, R. J., Ake, T. B., Crenshaw, D. M., Malamuth, E. M., Robinson, R. D., Sandoval, J. L., Shore, S. N., Wahlgren, G. M., Bruhweiler, F., Lindler, D. J., Gilliland, R. L., Hulbert, S. J., & Soderblom, D. R. 1995, PASP, 107, 871

Henry, G. W., Eaton, J. A., Hamer, J., & Hall, D. S. 1995, ApJS, 97, 513

Holweger, H., Bard, A., Kock, M., & Kock, A. 1991, A&A, 249, 545

Isliker, H. & Benz, A. O. 1994, A&AS, 104, 145

Jones, K. L., Brown, A., Stewart, R. T., & Slee, O. B. 1996, MNRAS, 283, 1331

Jones, K. L., Stewart, R. T., Nelson, G. J., & Duncan, A. R. 1994, MNRAS, 269, 1145

Jordan, C. 1996, in IAU Colloq. 152: Astrophysics in the Extreme Ultraviolet, ed. S. Bowyer & R. Malina (Kluwer), 81

Kai, K., Melrose, D. B., & Suzuki, S. 1985, in Solar Radiophysics: Studies of Emission from the Sun at Metre Wavelengths, 415–441

Klein, K.-L. & Chiuderi-Drago, F. 1987, A&A, 175, 179

Kucera, T. A., Dennis, B. R., Schartz, R. A., & Shaw, D. 1981, ApJ, 475, 338

Kuerster, M. & Schmitt, J. H. M. M. 1996, A&A, 311, 211

Kundu, M. R., White, S. M., Jackson, P. D., & Pallavicini, R. 1988, A&A, 195, 159

Lang, K. R., Bookbinder, J., Golub, L., & Davis, M. M. 1983, ApJ, 272, L15

Lestrade, J. F., Mutel, R. L., Phillips, R. B., Webber, J. C., Niell, A. E., & Preston, R. A. 1984, ApJ, 282, L23

Li, P., Emslie, A. G., & Mariska, J. T. 1993, ApJ, 417, 313

Linsky, J. L., Neff, J. E., Brown, A., Gross, B. D., Simon, T., Andrews, A. D., Rodono, M., & Feldman, P. A. 1989, A&A, 211, 173

Maggio, A., Pallavicini, R., Reale, F., & Tagliaferri, G. 2000, A&A, 356, 627

McTiernan, J. M., Fisher, G. H., & Li, P. 1999, ApJ, 514, 472

Mewe, R., Gronenschild, E. H. B. M., & van den Oord, G. H. J. 1985, A&AS, 62, 197

Morrison, R. & McCammon, D. 1983, ApJ, 270, 119

Mutel, R. L., Lestrade, J. F., Preston, R. A., & Phillips, R. B. 1985, ApJ, 289, 262

Mutel, R. L., Morris, D. H., Doiron, D. J., & Lestrade, J. F. 1987, AJ, 93, 1220

Ness, J.-U., Schmitt, J. H. M. M., Burwitz, V., Mewe, R., Raassen, A. J. J., van der Meer, R. L. J., Predehl, P., & Brinkman, A. C. 2002, A&A, 394, 911

Neupert, W. M. 1968, ApJ, 153, L59

Oláh, K., Kolláth, Z., & Strassmeier, K. G. 2000, A&A, 356, 643

Osten, R. A. & Brown, A. 1999, ApJ, 515, 746

Osten, R. A., Brown, A., Ayres, T. R., Linsky, J. L., Drake, S. A., Gagné, M., & Stern, R. A. 2000, ApJ, 544, 953

Ottmann, R. & Schmitt, J. H. M. M. 1994, A&A, 283, 871

Pallavicini, R, Tagliaferri, G., & Stella, L. 1990, A&A, 228, 403

Pallavicini, R. 2001, in Cool Stars, Stellar Systems, and the Sun: 11th Cambridge Workshop, ed. R. G. Lopez, R. Rebolo, & M. R. Zapaterio Osorio, ASP Conf. Ser. No. 223 (San Francisco: ASP), 377

Pasquini, L., Schmitt, J. H. M. M., & Pallavicini, R. 1989, A&A, 226, 225

Perryman, M. A. C., Lindegren, L., Kovalevsky, J., Hoeg, E., Bastian, U., Bernacca, P. L., Crézé, M., Donati, F., Grenon, M., van Leeuwen, F., van der Marel, H., Mignard, F., Murray, C. A., Le Poole, R. S., Schrijver, H., Turon, C., Arenou, F., Froeschlé, M., & Petersen, C. S. 1997, A&A, 323, L49

Piskunov, N., Wood, B. E., Linsky, J. L., Dempsey, R. C., & Ayres, T. R. 1997, ApJ, 474, 315

Randich, S., Gratton, R., & Pallavicini, R. 1993, A&A, 273, 194

Richards, M. T., Waltman, E. B., Ghigo, F. D., & Richards, D. S. P. 2003, ApJS, 147, 337

Sanz-Forcada, J., Brickhouse, N. S., & Dupree, A. K. 2002, ApJ, 570, 799

Schmitt, J. H. M. M., Ness, J.-U., & Franco, G. 2003, A&A, in press

Schrijver, C. J., Mewe, R., van den Oord, G. H. J., & Kaastra, J. S. 1995, A&A, 302, 438

Singh, K. P., White, N. E., & Drake, S. A. 1996, ApJ, 456, 766

Smith, R. K., Brickhouse, N. S., Liedahl, D. A., & Raymond, J. C. 2001, ApJ, 556, L91

Stepanov, A. V., Kliem, B., Krüger, A., Hildebrandt, J., & Garaimov, V. I. 1999, ApJ, 524, 961

Stepanov, A. V., Kliem, B., Zaitsev, V. V., Fürst, E., Jessner, A., Krüger, A., Hildebrandt, J., & Schmitt, J. H. M. M. 2001, A&A, 374, 1072

Stern, R. A., Uchida, Y., Walter, F., Vilhu, O., Hannikainen, D., Brown, A., Veale, A., & Haisch, B. M. 1992, ApJ, 391, 760

Strassmeier, K. G., Hall, D. S., Fekel, F. C., & Scheck, M. 1993, A&AS, 100, 173

Tanaka, Y., Inoue, H., & Holt, S. S. 1994, PASJ, 46, L37

Tandberg-Hanssen, E. & Emslie, A. G. 1988, The physics of solar flares (Cambridge University Press)

Torricelli-Ciamponi, G., Franciosini, E., Massi, M., & Neidhoefer, J. 1998, A&A, 333, 970

Trigilio, C., Umana, G., Catalano, S., Pallavicini, R., & Tagliaferri, G. 2000, in EVN Symposium 2000, ed. J. E. Conway, A. G. Polatidis, R. S. Booth, & Y. M. Pihlström (Onsala Space Obs.), 173

Trigilio, C., Umana, G., & Migenes, V. 1993, MNRAS, 260, 903

Umana, G., Trigilio, C., Tumino, M., Catalano, S., & Rodono, M. 1995, A&A, 298, 143

van den Oord, G. H. J. & Barstow, M. A. 1988, A&A, 207, 89

Vogt, S. S., Hatzes, A. P., Misch, A. A., & Kürster, M. 1999, ApJS, 121, 547

Weiler, E. J., Schmitz, M., Fraquelli, D. A., Piirola, V., Ryle, M., Gibson, D. M., Owen, F. N., Bopp, B. W., & Hall, D. S. 1978, ApJ, 225, 919

White, S. M. & Franciosini, E. 1995, ApJ, 444, 342

Wood, B. E., Harper, G. M., Linsky, J. L., & Dempsey, R. C. 1996, ApJ, 458, 761

Table 1. Summary of Multi-wavelength Observations

Year	Radio	UV	EUV	X-ray
1993	VLA[a], ATCA[b]	*IUE*[c], *HST/GHRS*[d]	*EUVE*[e]	...
	Sept 13.6–18.4, Sept. 14.5–17.9	Sept. 16.4–19.2, Sept. 15.0–19.7	Sept. 16.4–21.6	
1994	VLA, ATCA	*IUE*	*EUVE*	*ASCA*[f]
	Aug. 25.3–28.6, Aug. 23.7–27.0	Aug. 23.5–28.7	Aug. 24.0–28.0	Aug. 25.2–26.1
1996	VLA, ATCA	...	*EUVE*	*RXTE*[g]
	Sept. 2.3–7.7, Sept. 2.6–7.0		Sept. 1.5–11.1	Sept. 7.6–11.2
1998	VLA, ATCA	...	*EUVE*	*BeppoSAX*[h], *RXTE*
	Sept. 7.3–11.7, Sept. 8.6–12.9		Sept. 3.0–11.7	Sept. 6.9–10.0, Sept. 7.6–11.2

[a]VLA observations are at 3.6,6,20 cm (1993) and at 2,3.6,6,20 cm (1994,1996,1998)

[b]ATCA observations are at 3.6,6,13,20 cm

[c]*IUE* observations C IV, Mg II

[d]*HST/GHRS* observations C IV

[e]*EUVE* 80–380 Å

[f]*ASCA* 0.6–10 keV

[g]*RXTE* 2–12 keV

[h]*BeppoSAX* 1.5–10 keV

Table 2. Average 3.6 cm fluxes for HR 1099

Year	Avg. Flux (mJy)	Avg. Pol (%)
1993 Sept. 13.6–17.9	143.5±80.6	7.3±5.6
1994 Aug. 23.7–27.0	28.7±7.3	19.0±2.6
1996 Sept. 2.3–7.7	14.7±4.8	23.4±4.5
1998 Sept. 7.3–12.9	9.1±2.4	26.0±5.2

Table 3. Radio Flare Properties

Wavelength (cm)	L_{pk} (erg s^{-1} Hz^{-1})	E_{int} (erg Hz^{-1})	t_p[1] (d)	Δt[2] (d)
		1993 September 16–17		
3.6	$2.2\ 10^{17}$	$7.4\ 10^{21}$	16.3561±0.0003	0.64
6	$1.6\ 10^{17}$	$5.7\ 10^{21}$	16.3948±0.0005	0.64
		1994 August 25–26		
3.6	$1.2\ 10^{16}$	$3.8\ 10^{19}$	25.6618±0.0002	0.08
		1994 August 26–27		
3.6	$2.6\ 10^{16}$	$1.4\ 10^{20}$	26.56354±0.00007	0.15
6	$2.0\ 10^{16}$	$1.3\ 10^{20}$	26.5658±0.0002	0.15
20	$1.0\ 10^{16}$	$5.8\ 10^{19}$	26.5687±0.001	0.15
		1994 August 27–28		
3.6	$1.1\ 10^{16}$	$3.8\ 10^{19}$	27.4359±0.0004	0.17
6	$9.6\ 10^{15}$	$4.1\ 10^{19}$	27.440±0.002	0.17
		1996 September 4–5		
3.6	$3.6\ 10^{15}$	$9.8\ 10^{18}$	4.3759±0.0006	0.09
6	$3.8\ 10^{15}$	$1.8\ 10^{19}$	4.380±0.002	0.09
		1996 September 7a		
3.6	$1.9\ 10^{16}$	$1.1\ 10^{20}$	7.3630±0.0002	0.13
6	$5.2\ 10^{15}$	$2.8\ 10^{19}$	7.360±0.001	0.13
		1996 September 7b		
3.6	$5.5\ 10^{15}$	$2.9\ 10^{19}$	7.4738±0.0008	0.09
		1998 September 11–12		
3.6	$1.8\ 10^{15}$	$7.6\ 10^{18}$	11.510±0.002	0.10

[1] t_p: time of flare peak from profile fitting

[2] Δt: flare duration

Table 4. Correlations between 20 cm and 3.6 cm flares

Day	20 cm behavior	3.6 cm behavior
1994 Aug. 24–25	flux $\Uparrow$, large LCP	no variation
1994 Aug. 26–27	no change in flux, moderate LCP	moderate flare
1994 Aug. 27–28	flux $\Uparrow$, large LCP	small flare
1994 Aug. 28–29	flux $\Uparrow$, large LCP	no variation
1996 Sept. 2–3	flux $\Uparrow$, moderate LCP	no variation
1996 Sept. 3–4	no change in flux, moderate LCP	small enhancement
1996 Sept. 4–5	flux $\Downarrow$, moderate LCP	small flare
1996 Sept. 7–8	no variation	2 moderately large flares
1998 Sept. 8–9	flux $\Uparrow$, large LCP	slow modulation
1998 Sept. 9–10	no change in flux, moderate LCP	no variation
1998 Sept. 10–11	flux $\Uparrow$, large LCP	slow increase in flux
1998 Sept. 11–12	flux $\Uparrow$, large LCP	no variation

Table 5. Radio spectral indices for HR 1099

Year	Day	$\alpha_{3.6-2}$	$\alpha_{6-3.6}$	α_{13-6}	α_{20-13}	α_{20-6}
			Quiescence			
1993	Sept. 17.7	...	-0.40	0.30	0.90	...
1994	Aug. 25.4	-0.46 ± 0.06	-0.48 ± 0.02	...	...	-0.04 ± 0.01
1994	Aug. 26.4	-0.45 ± 0.08	-0.34 ± 0.03	...	...	0.01 ± 0.02
1996	Sept. 2.6	-0.74 ± 0.06	-0.46 ± 0.07	-0.08 ± 0.06	0 ± 0.08	...
1998	Sept. 7.3	-0.43 ± 0.09	-0.49 ± 0.03	...	...	0 ± 0.02
1998	Sept. 7.6	-0.16 ± 0.08	-0.31 ± 0.06	...	...	-0.07 ± 0.03
1998	Sept. 9.3	-0.84 ± 0.12	-0.64 ± 0.03	...	...	-0.30 ± 0.04
1998	Sept. 10.3	-2.32 ± 0.39	-0.45 ± 0.09	...	...	-0.49 ± 0.04
1998	Sept. 11.3	-0.66 ± 0.10	-0.40 ± 0.04	...	...	-0.32 ± 0.03
			Flare decays/peaks			
1993	Sept. 14.6	...	0.16	0.64	1.51	...
1993	Sept. 15.9	...	-0.25	0.28	1.29	...
1993	Sept. 16.6	...	-0.11	0.49	1.09	...
1994	Aug. 25.6	-0.36 ± 0.07	0.08 ± 0.06	-0.23 ± 0.05	0.21 ± 0.07	...
1994	Aug. 26.6	-0.48 ± 0.06	-0.24 ± 0.04	0.06 ± 0.04	0.77 ± 0.08	...

Table 6. Summary of *EUVE* Exposure Times [1]

Time Interval	SW (s)	MW (s)
1993 **Q**	16524.5	16064.3
1993 **F1**	24453.7	22652.
1993 **F2**	20427.6	19229.6
1994 **Q**	5687.0[a]	5678.7[a]
1994 **F**	49484.8	49255.1
1996 **Q**	43742.4	40766.8
1996 **F**	44229.0	41090.9
1996 **F1**	67882.2	66570.9
1996 **F2**	36778.7	36596.3
1998 **Q**	141476.	118332.9
1998 **F**	12457.[a]	10547.3[a]
sumQ	402273.	370690.
sumF	266539.	257924.

[1]See Section 4.3.2 for explication of how time intervals were determined; Figure 9 depicts time intervals.

[a]Spectrum was not detected.

Table 7. Comparison of continuum effect on measured line fluxes

	composite quiescent spectrum		composite flare spectrum	
Fe/H /(Fe/H)$_{\odot}$	Fe XVIII λ 93.92[a]	Fe XXII λ 135.78[a]	Fe XVIII λ 93.92[a]	Fe XXII λ 135.78[a]
1.0	0.94	0.88	0.91	0.92
0.9	0.93	0.88	0.90	0.92
0.8	0.92	0.87	0.89	0.91
0.7	0.92	0.87	0.87	0.91
0.6	0.90	0.86	0.85	0.90
0.5	0.89	0.86	0.83	0.89
0.4	0.86	0.84	0.78	0.88
0.3	0.81	0.83	0.72	0.86
0.2	0.69	0.80	0.58	0.81
0.1	0.46	0.71	0.16	0.67

[a] Measured emission line flux with continuum subtracted at given abundance divided by emission line flux with no continuum subtraction

Table 8. *EUVE* Line Fluxes for HR 1099

Line	**1993Q**	**1993F1**	**1993F2**	**1994F**	**1996Q**	**1996F**	**1996F1**	**1996F2**	**1998Q**
					(10^{-13} erg cm^{-2} s^{-1})				
Fe XVIII λ93.92	2.00±0.33	2.32±0.44	1.53±0.42	1.31±0.26	1.01±0.23	0.99±0.22	0.87±0.19	1.83±0.34	1.09±0.12
Fe XXI λ97.88	<0.7	<1.1	<1.1	<0.6	<0.5	<0.6	0.61±0.18	0.90±0.28	0.64±0.10
Fe XIX λ101.55	<0.7	1.28±0.36	<1.0	0.58±0.17	0.59±0.18	<0.5	0.81±0.16	1.28±0.29	0.40±0.08
Fe XXI λ102.22	1.20±0.26	1.51±0.39	1.26±0.36	0.82±0.18	0.82±0.19	<0.5	1.02±0.17	1.91±0.31	0.67±0.09
Fe XVIII λ103.937	0.65±0.21	0.98±0.32	<1.0	<0.52	0.48±0.15	0.69±0.19	1.00±0.17	1.30±0.28	0.49±0.08
Fe XIX λ108.37	1.03±0.23	2.53±0.44	1.16±0.38	1.48±0.22	0.58±0.18	0.96±0.20	1.37±0.18	1.46±0.28	0.67±0.10
Fe XIX λ109.97	<0.6	<1.0	<1.0	<0.4	<0.5	<0.4	0.60±0.14	1.01±0.27	0.34±0.08
Fe XIX λ111.70	<0.6	1.00±0.31	<1.0	0.76±0.18	<0.4	<0.4	0.49±0.14	1.31±0.26	0.32±0.07
Fe XXII λ114.41	<0.6	1.18±0.33	<1.1	<0.5	<0.5	<0.5	0.87±0.16	1.49±0.29	0.29±0.08
Fe XXII λ117.17	2.03±0.31	3.24±0.48	2.53±0.48	2.03±0.27	1.30±0.22	1.78±0.24	2.09±0.22	3.35±0.36	0.93±0.11
Fe XX λ118.66	0.72±0.24	1.19±0.37	<1.1	0.80±0.20	0.56±0.18	0.78±0.19	1.25±0.17	1.01±0.25	0.54±0.09
Fe XIX λ120.00	<0.7	1.34±0.38	<1.0	<0.5	<0.5	<0.5	0.61±0.15	<0.7	<0.2
Fe XX λ121.83	0.92±0.26	1.43±0.40	<1.2	0.72±0.19	0.90±0.20	1.35±0.23	1.05±0.18	1.64±0.30	0.73±0.09
Fe XXI λ128.73	2.54±0.36	3.02±0.52	2.49±0.54	1.98±0.26	1.55±0.25	1.97±0.28	2.16±0.22	3.20±0.38	1.41±0.13
Fe XX,XXIII λ132.85	6.13±0.60	19.10±1.14	12.2±1.03	5.35±0.45	5.70±0.48	5.86±0.51	6.31±0.41	11.90±0.74	4.73±0.24
Fe XXII λ135.78	1.04±0.34	3.98±0.59	2.35±0.60	1.68±0.30	1.36±0.27	1.18±0.26	1.42±0.24	2.08±0.37	0.97±0.13
Fe XXIV λ192.02	4.34±0.92	11.30±1.58	8.64±1.57	5.02±0.67	3.85±0.66	3.32±0.66	6.27±0.62	7.28±0.90	2.33±0.36
Fe XXIV λ255.09	<3.0	7.16±1.51	6.82±1.76	3.88±0.80	<2.5	3.89±0.84	3.47±0.64	6.10±1.09	1.40±0.43
Fe XV λ284.16	<2.7	<3.4	5.10±1.53	<1.7	<2.0	<2.0	1.41±0.44	2.38±0.74	1.10±0.37
Fe XVI λ335.41	<2.6	<3.4	<4.3	<1.8	<1.9	<1.9	1.56±0.46	2.56±0.71	<1.1
Fe XVI λ360.76	<2.4	<3.2	<4.1	<1.7	<1.9	<1.8	<1.3	<2.1	1.11±0.34

Table 9. *EUVE* Line Fluxes from composite quiescent and flare spectra

Line	λ (Å)	**sumQ** (10^{-13} erg cm^{-2} s^{-1})	**sumF**
Fe XVIII	93.92	1.19±0.97	1.27±0.10
Fe XXI	97.88	0.59±0.06	0.60±0.09
Fe XIX	101.55	0.61±0.06	0.73±0.08
Fe XXI	102.22	0.75±0.06	1.00±0.08
Fe XVIII	103.94	0.51±0.05	0.86±0.08
Fe XIX	108.37	0.84±0.06	1.20±0.08
Fe XIX	109.97	0.36±0.05	0.46±0.07
Fe XIX	111.70	0.35±0.05	0.59±0.07
Fe XXII	114.41	0.48±0.05	0.76±0.08
Fe XXII	117.17	1.53±0.08	2.13±0.11
Fe XX	118.66	0.61±0.06	0.90±0.08
Fe XIX	120.00	0.34±0.05	0.42±0.07
Fe XX	121.83	0.95±0.07	1.09±0.09
Fe XXI	128.73	1.74±0.09	2.07±0.11
Fe XX,XXIII	132.85	5.41±0.16	6.82±0.22
Fe XXII	135.78	1.48±0.09	1.68±0.12
Fe XXIV	192.02	3.50±0.22	6.73±0.34
Fe XXIV	255.09	2.21±0.25	4.66±0.35
Fe XV	284.16	1.30±0.21	2.26±0.24
Fe XVI	335.41	1.21±0.21	2.11±0.24
Fe XVI	360.76	0.95±0.20	1.25±0.22

Table 10. Electron densities in *EUVE* spectra from Fe XXI and Fe XXII line ratios

Time interval	Fe XXI 128.73/102.22		Fe XXII 117.17/114.41	
	ratio$\pm$ 1σ error	n$_e$ (cm^{-3})	ratio$\pm$ 1σ error	n$_e$ (cm^{-3})
1993Q	2.1$\pm$0.5	3.0$\times$10^{12} (1.5$\times$10^{12} – 6$\times$ 10^{12})	4.0$\pm$1.8	...
1993F1	2.0$\pm$0.6	3.2$\times$10^{12} (1.6$\times$10^{12}–8.7$\times$10^{12})	2.7$\pm$0.9	$>$4.7 10^{12}
1993F2	2.0$\pm$0.7	3.2$\times^{12}$(1.5$\times$10^{12} – 10^{13})	3.5$\pm$1.9	5.1$\times$10^{12}(6.8$\times$10^{11}–10^{13})
1994F	2.4$\pm$0.6	2.0$\times$10^{12}(10^{12} – 4.3$\times$10^{12})	4.7$\pm$1.9	...
1996Q	1.9$\pm$0.5	3.7$\times$10^{12}(1.9$\times$10^{12}–9.1$\times$10^{12})	2.8$\pm$1.1	$>$3.4 10^{12}
1996F	5.1$\pm$2.3	$<$1.4$\times$10^{12}	4.0$\pm$1.6	...
1996F1	2.1$\pm$0.4	2.8$\times$10^{12} (1.7$\times$10^{12}–4.9$\times$10^{12})	2.4$\pm$0.5	...
1996F2	1.7$\pm$0.3	5.1$\times$10^{12} (3.2$\times$10^{12}–9.3$\times$10^{12})	2.2$\pm$0.5	...
1998	2.1$\pm$0.3	3.0$\times$10^{12} (1.9$\times$10^{12} – 4.5$\times$10^{12})	3.2$\pm$0.9	7.2$\times$10^{12} (2.8$\times$10^{12}–10^{13})
sumF	2.1$\pm$0.2	3.0$\times$10^{12} (2.3$\times$10^{12}–3.8$\times$10^{12})	2.8$\pm$0.3	$>$8.1 10^{12}
sumQ	2.3$\pm$0.2	2.2$\times$10^{12} (1.8$\times$10^{12}–2.8$\times$10^{12})	3.2$\pm$0.4	7.4$\times$10^{12}(4.9$\times$10^{12}–10^{13})

Table 11. Luminosities and timescales during the 1994 *ASCA* observation

Energy Range (keV)	**Q**[1] (ergs s^{-1})	**R/Q**	**P/Q**	**D1/Q**	**D2/Q**
0.6–2	5.2 10^{30}	1.4	1.6	1.3	1.2
2–5	1.9 10^{30}	2.2	2.0	1.4	1.1
5–10	4.4 10^{29}	3.6	2.5	1.5	1.2
0.6–10	7.5 10^{30}	1.7	1.7	1.3	1.1
	τ_r (hrs)			τ_d (hrs)	
0.6–2	4.3±0.7			8.4±2.0	
2–5	2.2±0.3			4.8±1.5	
5–10	0.9±0.2			2.8±1.3	
0.6–10	3.8±0.5			7.6±1.6	

[1]N_H=1.35 10^{18} cm^{-2} was used to estimate the luminosities.

Table 12. VMEKAL 2-Temperature spectral fits to flaring/quiescent *ASCA* spectra

	Q[1]	**R**[1]	**P**[1]	**D1**[1]	**D2**[1]
			– SIS0 0.6 - 10 keV –		
kT_1 (keV)	$0.7^{+0.02}_{-0.03}$	0.72 ± 0.06	0.67 ± 0.05	$0.65^{+0.04}_{-0.06}$	0.71 ± 0.05
kT_2 (keV)	$2.21^{+0.13}_{-0.09}$	$2.86^{+0.19}_{-0.18}$	$2.39^{+0.15}_{-0.12}$	$2.21^{+0.11}_{-0.10}$	$2.46^{+0.50}_{-0.43}$
log EM_1 (cm^{-3})	$53.54^{+0.12}_{-0.09}$	$53.23^{+0.14}_{-0.12}$	$53.42^{+0.10}_{-0.12}$	$53.42^{+0.12}_{-0.10}$	$53.84^{+0.16}_{-0.39}$
log EM_2 (cm^{-3})	$53.74^{+0.02}_{-0.03}$	53.97 ± 0.04	54.05 ± 0.04	53.87 ± 0.03	53.74 ± 0.10
O	0.2 ± 0.1	$0.54^{+0.36}_{-0.29}$	$0^{+0.19}_{-0}$	$0.27^{+0.19}_{-0.15}$	$0.13^{+0.32}_{-0.11}$
Ne	$0.97^{+0.19}_{-0.20}$	$1.57^{+0.57}_{-0.51}$	$1.16^{+0.37}_{-0.30}$	$1.59^{+0.35}_{-0.30}$	$0.73^{+0.64}_{-0.22}$
Mg	$0.27^{+0.11}_{-0.09}$	$0.25^{+0.39}_{-0.25}$	$0.26^{+0.28}_{-0.23}$	$0.51^{+0.24}_{-0.20}$	$0.17^{+0.31}_{-0.10}$
Si	0.23 ± 0.07	$0.68^{+0.35}_{-0.29}$	$0.33^{+0.22}_{-0.17}$	$0.40^{+0.17}_{-0.14}$	$0.15^{+0.14}_{-0.07}$
S	0.27 ± 0.10	$0.25^{+0.35}_{-0.25}$	$0.22^{+0.240}_{-0.216}$	$0.34^{+0.20}_{-0.18}$	$0.21^{+0.18}_{-0.17}$
Ar	$0.44^{+0.31}_{-0.30}$	$1.27^{+0.94}_{-0.90}$	$0^{+0.23}_{-0}$	$0.88^{+0.54}_{-0.51}$	$0.31^{+0.65}_{-0.31}$
Ca	$0.56^{+0.45}_{-0.44}$	$0.73^{+1.05}_{-0.73}$	$0.92^{+0.85}_{-0.84}$	$0.12^{+0.70}_{-0.12}$	$0.002^{+0.628}_{-0.002}$
Fe	0.12 ± 0.04	0.33 ± 0.11	$0.22^{+0.09}_{-0.06}$	0.20 ± 0.06	$0.05^{+0.12}_{-0.02}$
Ni	$1.14^{+0.40}_{-0.35}$	$1.88^{+1.57}_{-1.32}$	$1.48^{+1.11}_{-0.90}$	$1.12^{+0.80}_{-0.84}$	$0.75^{+0.75}_{-0.39}$
χ^2/dof	156.2/160	143.8/128	91.0/121	122.5/130	130.6/121
			– SIS0 + SIS1 0.6 - 10 keV –		
kT_1 (keV)	0.70 ± 0.02	0.71 ± 0.05	$0.73^{+0.05}_{-0.04}$	0.66 ± 0.03	$0.73^{+0.04}_{-0.03}$
kT_2 (keV)	$2.22^{+0.11}_{-0.07}$	$2.82^{+0.15}_{-0.13}$	$2.44^{+0.13}_{-0.10}$	$2.20^{+0.09}_{-0.08}$	$2.20^{+0.38}_{-0.11}$
logEM_1 (cm^{-3})	$53.55^{+0.09}_{-0.08}$	$53.26^{+0.11}_{-0.09}$	$53.48^{+0.14}_{-0.10}$	$53.40^{+0.08}_{-0.07}$	$53.58^{+0.25}_{-0.11}$
log EM_2 (cm^{-3})	53.73 ± 0.02	53.97 ± 0.03	54.05 ± 0.04	53.87 ± 0.02	$53.78^{+0.03}_{-0.09}$
O	0.21 ± 0.08	$0.47^{+0.25}_{-0.21}$	$0.12^{+0.16}_{-0.12}$	$0.27^{+0.14}_{-0.11}$	$0.30^{+0.14}_{-0.18}$
Ne	$1.04^{+0.15}_{-0.16}$	$1.58^{+0.42}_{-0.37}$	$1.10^{+0.29}_{-0.27}$	$1.60^{+0.26}_{-0.24}$	$1.21^{+0.24}_{-0.41}$
Mg	$0.29^{+0.09}_{-0.07}$	$0.30^{+0.28}_{-0.26}$	$0.36^{+0.21}_{-0.19}$	$0.53^{+0.17}_{-0.16}$	$0.32^{+0.14}_{-0.17}$
Si	$0.26^{+0.05}_{-0.06}$	$0.62^{+0.25}_{-0.21}$	$0.25^{+0.14}_{-0.13}$	$0.40^{+0.12}_{-0.11}$	$0.22^{+0.10}_{-0.08}$
S	0.31 ± 0.08	$0.24^{+0.25}_{-0.24}$	$0.25^{+0.18}_{-0.17}$	$0.23^{+0.14}_{-0.13}$	$0.29^{+0.14}_{-0.13}$
Ar	$0.48^{+0.23}_{-0.24}$	$0.84^{+0.64}_{-0.67}$	$0^{+0.23}_{-0}$	$0.45^{+0.38}_{-0.37}$	$0.28^{+0.41}_{-0.28}$
Ca	0.60 ± 0.34	$0.98^{+0.80}_{-0.84}$	$0.84^{+0.65}_{-0.66}$	$0.31^{+0.54}_{-0.31}$	$0.009^{+0.481}_{-0.009}$
Fe	0.12 ± 0.03	0.30 ± 0.08	$0.20^{+0.07}_{-0.06}$	0.21 ± 0.05	$0.14^{+0.05}_{-0.08}$
Ni	$1.05^{+0.28}_{-0.27}$	$1.92^{+1.14}_{-0.88}$	$1.72^{+0.84}_{-0.75}$	$1.28^{+0.64}_{-0.54}$	$0.82^{+0.49}_{-0.46}$

Table 12—Continued

	Q[1]	**R**[1]	**P**[1]	**D1**[1]	**D2**[1]
χ^2/dof	355.8/325	264.8/253	253.7/244	260.4/259	263.0/243
			– SIS0 + GIS2 0.6 - 10 keV –		
kT_1 (keV)	$0.69^{+0.03}_{-0.02}$	0.72 ± 0.06	$0.68^{+0.06}_{-0.05}$	$0.65^{+0.04}_{-0.05}$	0.70 ± 0.05
kT_2 (keV)	$2.17^{+0.09}_{-0.07}$	$2.86^{+0.05}_{-0.04}$	$2.36^{+0.11}_{-0.10}$	$2.25^{+0.09}_{-0.10}$	$2.31^{+0.47}_{-0.25}$
log EM_1 (cm^{-3})	$53.53^{+0.09}_{-0.07}$	$53.24^{+0.13}_{-0.11}$	53.46 ± 0.11	$53.42^{+0.11}_{-0.09}$	$53.75^{+0.21}_{-0.27}$
log EM_2 (cm^{-3})	53.74 ± 0.02	53.97 ± 0.03	54.05 ± 0.04	53.86 ± 0.03	$53.76^{+0.11}_{-0.07}$
O	$0.19^{+0.09}_{-0.08}$	$0.56^{+0.31}_{-0.27}$	$0^{+0.16}_{-0}$	$0.30^{+0.17}_{-0.15}$	$0.18^{+0.35}_{-0.16}$
Ne	$1.02^{+0.16}_{-0.17}$	$1.55^{+0.51}_{-0.49}$	$1.16^{+0.37}_{-0.28}$	1.61 ± 0.32	$0.84^{+0.48}_{-0.31}$
Mg	$0.29^{+0.10}_{-0.08}$	$0.30^{+0.35}_{-0.30}$	$0.28^{+0.26}_{-0.20}$	$0.51^{+0.23}_{-0.18}$	$0.20^{+0.23}_{-0.13}$
Si	$0.23^{+0.06}_{-0.05}$	$0.54^{+0.27}_{-0.22}$	$0.28^{+0.18}_{-0.13}$	$0.37^{+0.14}_{-0.12}$	$0.11^{+0.09}_{-0.08}$
S	0.22 ± 0.08	$0.28^{+0.29}_{-0.26}$	$0.08^{+0.22}_{-0.08}$	$0.32^{+0.16}_{-0.15}$	$0.24^{+0.18}_{-0.15}$
Ar	0.68 ± 0.26	$0.24^{+0.70}_{-0.24}$	$0^{+0.16}_{-0}$	0.77 ± 0.44	$0.42^{+0.63}_{-0.42}$
Ca	$0.87^{+0.40}_{-0.39}$	$0.58^{+0.95}_{-0.58}$	$1.30^{+0.64}_{-0.65}$	$0^{+0.71}_{-0}$	$0.13^{+0.73}_{-0.13}$
Fe	0.13 ± 0.03	0.32 ± 0.09	$0.22^{+0.07}_{-0.06}$	$0.20^{+0.07}_{-0.05}$	$0.07^{+0.09}_{-0.04}$
Ni	$1.08^{+0.35}_{-0.32}$	$2.14^{+1.33}_{-1.17}$	$1.20^{+0.96}_{-0.78}$	$1.14^{+0.74}_{-0.67}$	$0.77^{+0.62}_{-0.45}$
χ^2/dof	529.0/490	338.8/321	285.4/313	337.4/350	314.1/316

[1] N_H fixed at 1.35 10^{18} cm^{-2}. Uncertainties are 90% confidence intervals.

Table 13. Luminosity in *RXTE* observations

Energy Range (keV)	1996 (erg s^{-1})	1998 (erg s^{-1})
2–5	2.6 10^{30}	1.7 10^{30}
5–12	7.7 10^{29}	3.8 10^{29}
2–12	3.4 10^{30}	2.1 10^{30}

Table 14. Flare energies in *RXTE* observations

Energy Range (keV)	τ_r (hrs)	τ_d (hrs)	Δ t (hrs)	Energy (ergs)
1996 Flare on September 4.8				
2–5	1.66±0.11	3.85±0.54	2.6	1.6 10^{34}
5–12	1.13±0.09	2.24±0.35	2.6	8 10^{33}
2–12	1.38±0.09	2.63±0.24	2.6	2.7 10^{34}
1998 Flare on September 9.8				
2–5	...[a]	3.88±0.66	3.4	1.3 10^{34}
5–12	...[a]	1.89±0.34	3.4	3 10^{33}
2–12	...[a]	2.61±0.37	3.4	1.6 10^{34}

[a]Flare rise was not observed.

Table 15. Luminosities and MECS timescales during the 1998 *BeppoSAX* observation

Energy Range (keV)	**Q** (erg s^{-1})	**F1** (erg s^{-1})	**F2** (erg s^{-1})	**D** (erg s^{-1})	**F3** (erg s^{-1})
0.6–2	3.7 10^{30}	5.0 10^{30}	5.1 10^{30}	4.1 10^{30}	4.4 10^{30}
2–5	1.1 10^{30}	2.2 10^{30}	2.1 10^{30}	1.3 10^{30}	1.5 10^{30}
5–10	2.3 10^{29}	6.0 10^{29}	6.1 10^{29}	2.8 10^{29}	3.9 10^{29}
0.6–10	5.1 10^{30}	7.8 10^{30}	7.8 10^{30}	5.7 10^{30}	6.4 10^{30}
τ_r (hrs)		11.1±0.7	2.1±0.3		2.3±0.3
τ_d (hrs)		13.2±3.8	3.7±0.2		4.5±0.4

Table 16. MEKAL 2-Temperature spectral fits to flaring/quiescent *BeppoSAX* LECS + MECS spectra

	F1	**F2**	**D**	**Q**	**F3**
kT_1 (keV)	$0.90^{+0.09}_{-0.09}$	$0.83^{+0.13}_{-0.11}$	$0.77^{+0.07}_{-0.07}$	$0.81^{+0.04}_{-0.05}$	$0.78^{+0.11}_{-0.09}$
kT_2 (keV)	$2.41^{+0.18}_{-0.15}$	$2.42^{+0.34}_{-0.22}$	$1.98^{+0.13}_{-0.11}$	$1.98^{+0.10}_{-0.08}$	$2.24^{+0.31}_{-0.18}$
log EM_1 (cm^{-3})	$53.42^{+0.15}_{-0.16}$	$53.35^{+0.24}_{-0.23}$	$53.34^{+0.12}_{-0.13}$	$53.35^{+0.09}_{-0.08}$	$53.40^{+0.20}_{-0.18}$
log EM_2 (cm^{-3})	$53.76^{+0.04}_{-0.05}$	$53.75^{+0.05}_{-0.07}$	$53.63^{+0.04}_{-0.04}$	$53.55^{+0.03}_{-0.04}$	$53.64^{+0.05}_{-0.08}$
Z	$0.27^{+0.07}_{-0.05}$	$0.34^{+0.14}_{-0.10}$	$0.30^{+0.07}_{-0.05}$	$0.29^{+0.04}_{-0.03}$	$0.30^{+0.10}_{-0.08}$
χ^2/dof	179.2/172	113.7/115	170.5/177	329.8/287	121.4/130

Table 17. Radio, EUV Quiescent Emission Properties

Dates	$L_{3.6}$ (erg s^{-1} Hz^{-1})	L_{EUV} (erg s^{-1})	log $\frac{L_{EUV}}{L_{3.6}}$ (Hz)
1993 Sept. 17.7–17.9	9.5 10^{16}	1.2 10^{30}	13.1
1994 Aug. 25.3–25.6	3 10^{16}	6.6 10^{29}	13.3
1994 Aug. 26.4–26.5	2.9 10^{16}	8.4 10^{29}	13.5
1996 Sept. 2.3–2.8	1.9 10^{16}	6.0 10^{29}	13.5
1996 Sept. 6.3–7.0	9.9 10^{15}	7.2 10^{29}	13.9
1998 Sept. 7.4–7.6	9.9 10^{15}	7.3 10^{29}	13.9
1998 Sept. 9.6–9.8	8.0 10^{15}	6.6 10^{29}	13.9

Table 18. EUV/SXR flares on HR 1099 and multi-wavelength behavior

Time of peak flux	EUV/SXR telescope that saw flare	comments
1993 Sept. 17.4	*EUVE*	C IV/Mg II flux rises, peaks $\approx$ 4 hrs before EUV peak
		secondary maximum in Mg II flux after EUV peak
		gap in radio coverage during EUV flare rise
1993 Sept. 19.2	*EUVE*	C IV flux rise and peak $\approx$ 3 hrs before EUV flare peak
		Mg II flux increases but does not reach a peak
		no radio coverage
1994 Aug. 24.2	*EUVE*	flare seen in Mg II, C IV; peak is missed
		gap in radio coverage
1994 Aug. 25.76	*EUVE*, *ASCA*	radio flare peaks $\sim$ 2.5 hrs before EUV/SXR maxima
		no response of Mg II to flare, slight increase in C IV
1994 Aug. 27.00	*EUVE*	radio flare accompanied by increase in C IV flux; both peak $\approx$
		4.8 hrs before the end of the EUV rise
		no response from Mg II
1996 Sept. 2.0	*EUVE*	no radio, SXR coverage
1996 Sept. 2.9	*RXTE*	no radio flare, no EUV enhancement
1996 Sept. 4.4	*EUVE*	small radio flare peaks $\sim$ 0.5 hr before small EUV enhancement, gap in SXR coverage
1996 Sept. 4.8	*EUVE*, *RXTE*	possibly small radio enhancement
1996 Sept. 5.3	*EUVE*	gaps in SXR coverage; radio coverage limited to after EUV peak
1996 Sept. 8.7–9.6	*EUVE*	2 radio flares during EUV rise, peaking $\sim$ 30 hrs before 1st EUV peak
		radio coverage limited to beginning of EUV flare; gap in SXR coverage
1998 Sept. 5.9	*EUVE*	no radio, SXR coverage
1998 Sept. 7.1	*BeppoSAX*	gap in EUV, radio coverage

Table 18—Continued

Time of peak flux	EUV/SXR telescope that saw flare	comments
1998 Sept. 7.3	*BeppoSAX*	limited EUV, radio coverage; no increase in EUV or radio flux
1998 Sept. 7.9	*BeppoSAX*, *RXTE*	small enhancement in *BeppoSAX* light curve, rise in *RXTE*
		no EUV flare, gap in radio coverage
1998 Sept. 8.4	*BeppoSAX*	small enhancement in *BeppoSAX* light curve
		no EUV enhancements, no radio flare
1998 Sept. 9.8	*BeppoSAX*, *RXTE*	no EUV or radio enhancement

Table 19. Comparison of radio, EUV/SXR flare properties

Date	1994 Aug. 25.76	1994 Aug. 27.0	1996 Sept. 7
EUV/SXR peak Lum. (erg s^{-1})	2.4×10^{29} (EUV)	1.2×10^{30}	1.9×10^{30}
	5.2×10^{30} (SXR)		
3.6 cm peak Lum. (erg s^{-1} Hz^{-1})	1.2×10^{16}	2.6×10^{16}	1.9×10^{16}
ratio $L_{EUV,SXR}/L_R$ (Hz)	2.0×10^{13} (EUV)	4.6×10^{13}	1.0×10^{14}
	4.3×10^{14} (SXR)		
EUV/SXR energy (erg)	1.8×10^{33} (EUV)	8.1×10^{34}	3.5×10^{35}
	5.3×10^{34}(SXR)		
3.6 cm energy (erg Hz^{-1})	3.8×10^{19}	1.4×10^{20}	1.1×10^{20}
ratio $E_{EUV,SXR}/E_R$ (Hz)	4.7×10^{13} (EUV)	5.8×10^{14}	3.2×10^{15}
	1.4×10^{15} (SXR)		
EUV/SXR duration $\Delta t_{EUV,SXR}$ (hr)	9.4	30.1	83.6
3.6 cm duration Δt_R (hr)	2	2.3	10.2
ratio $\Delta t_{EUV,SXR}/\Delta t_R$	4.5	13.1	8.2
$t_{peak,EUV(SXR)}$-$t_{peak,R}$ (hr)	2.5	4.8	30

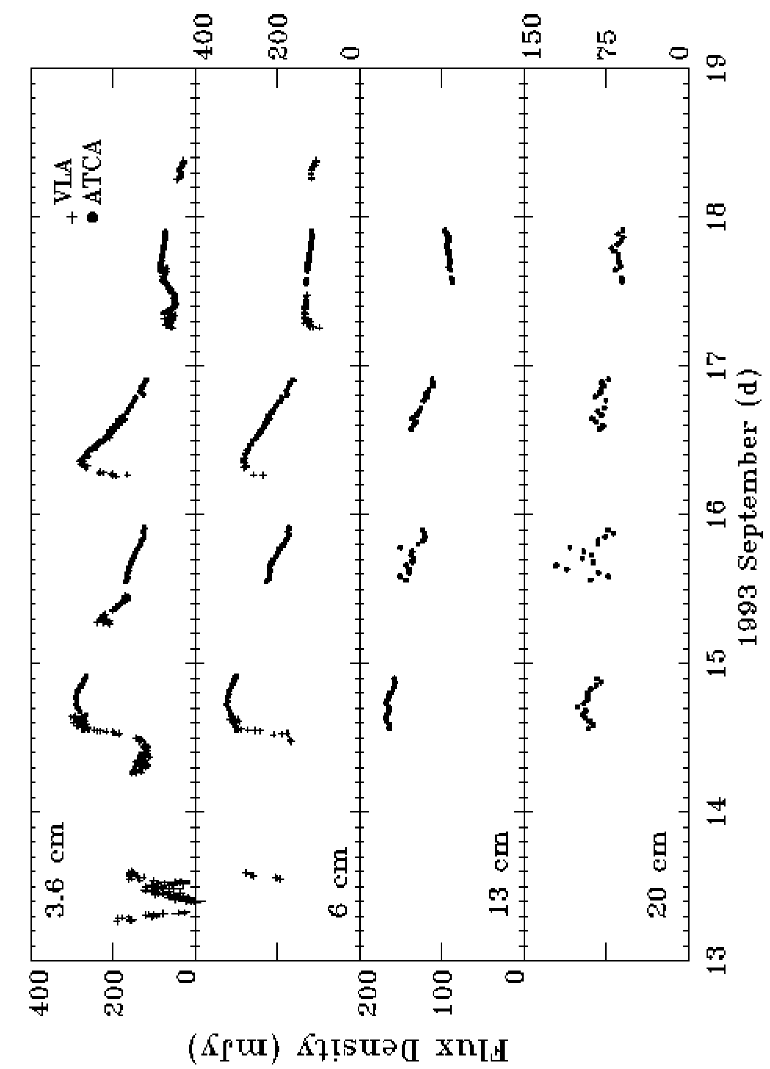

Fig. 1a.— (a) Flux density variations at 3.6, 6, 13, and 20 cm during the 1993 observations. Crosses indicate VLA data; circles denote ATCA observations. Error bars are 1 σ. (b) Variations in percent circular polarization at 3.6, 6, and 13 cm during the 1993 observation. Symbols as in Figure 1a. Error bars are 1 σ. Zero percent circular polarization is shown as a dotted line.

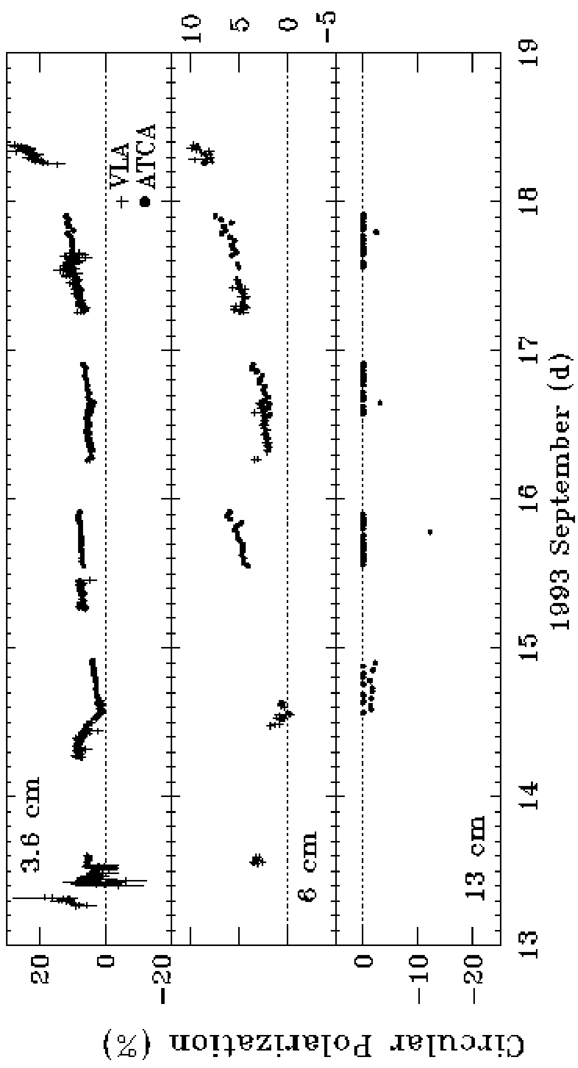
3.6 cm
6 cm
13 cm
+ VLA
● ATCA
1993 September (d)
Circular Polarization (%)

Fig. 1b.—

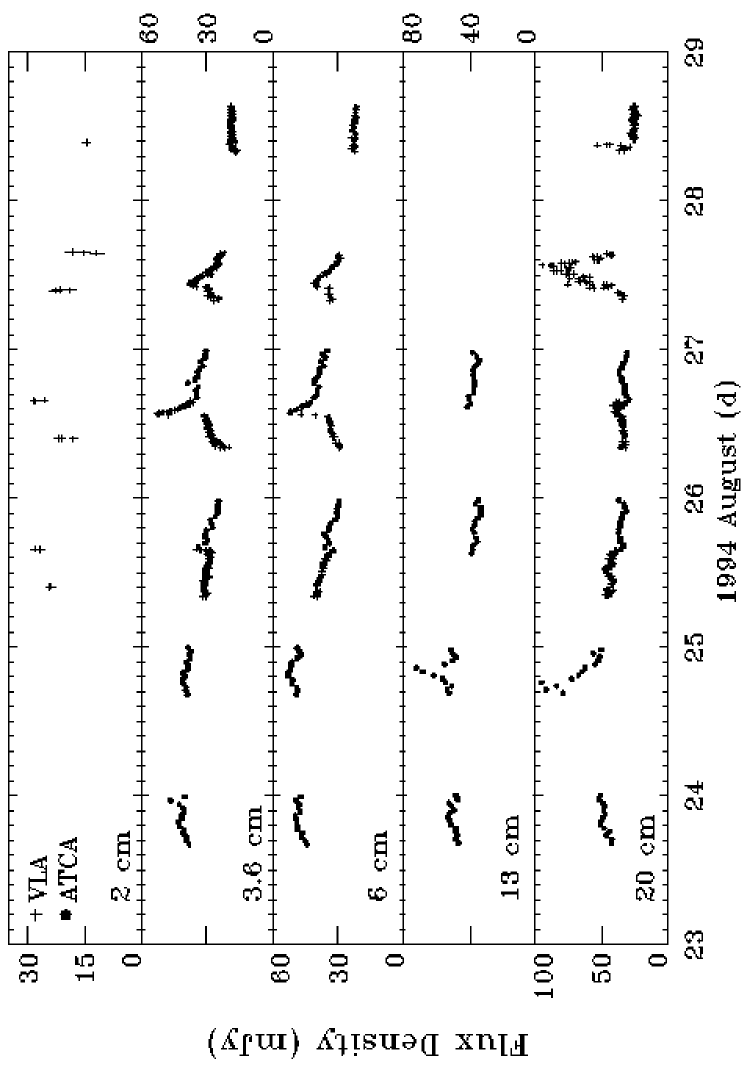

Fig. 2a.— (a)Flux density variations at 2, 3.6, 6, 13, and 20 cm during the 1994 observations. Crosses indicated VLA data; circles denote ATCA observations. Error bars are 1 σ. (b) Variations in percent circular polarization at 2, 3.6, 6, 13, and 20 cm. Symbols are as in Figure 2a. Error bars are 1 σ. Zero percent circular polarization is shown as a dotted line.

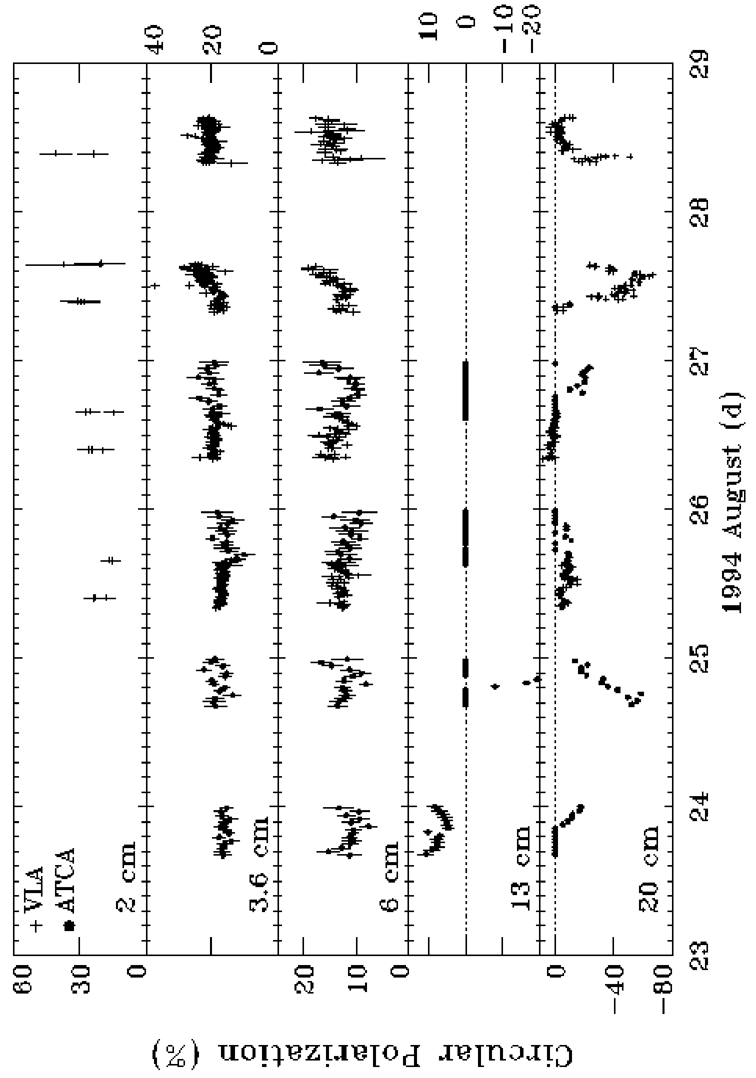

+ VLA
ATCA
2 cm
3.6 cm
6 cm
13 cm
20 cm
Circular Polarization (%)
1994 August (d)

Fig. 2b.—

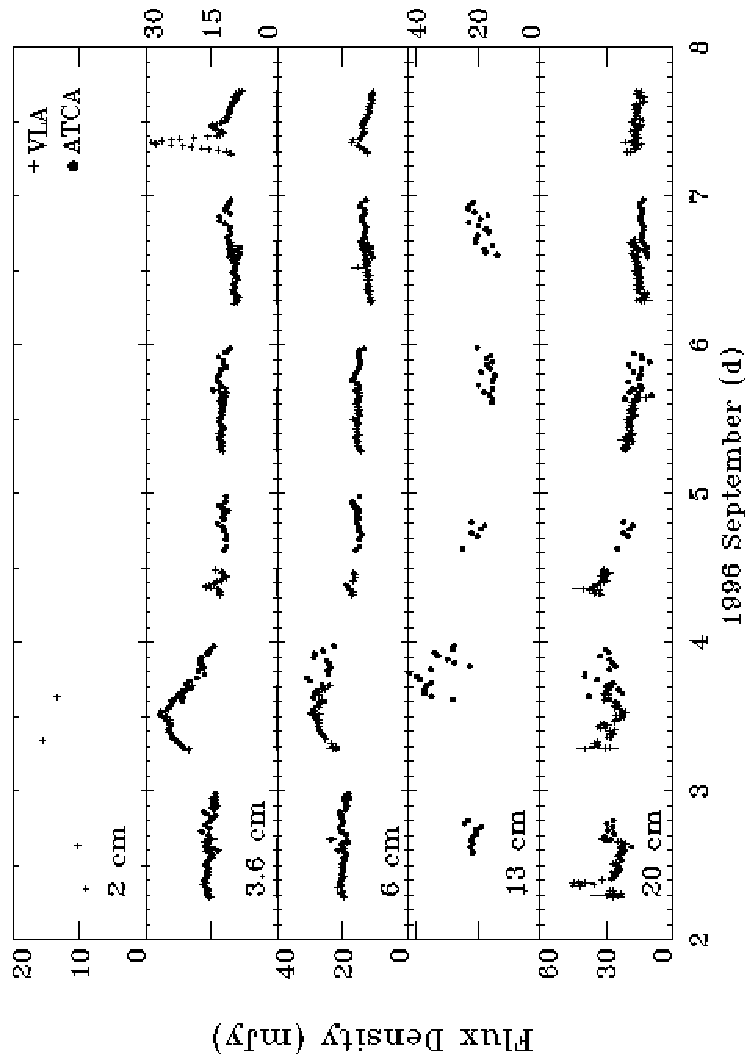

Fig. 3a.— (a) Flux density variations at 2, 3.6, 6, 13, and 20 cm during the 1996 observations. Crosses indicate VLA data; circles denote ATCA observations. Error bars are 1 σ. (b) Variations in percent circular polarization at 2, 3.6, 6, 13, and 20 cm. Symbols are as in Figure 3a. Error bars are 1 σ. Zero percent circular polarization is shown as a dotted line.

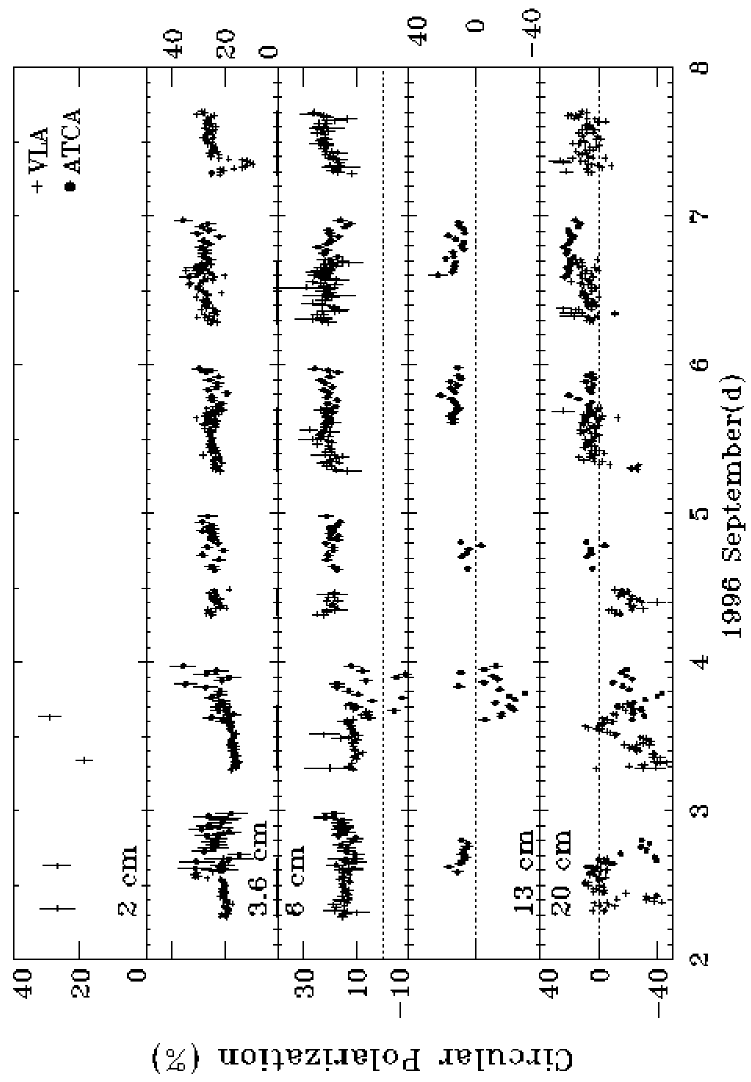
+ VLA
● ATCA
2 cm
3.6 cm
6 cm
13 cm
20 cm
1996 September(d)
Circular Polarization (%)

Fig. 3b.—

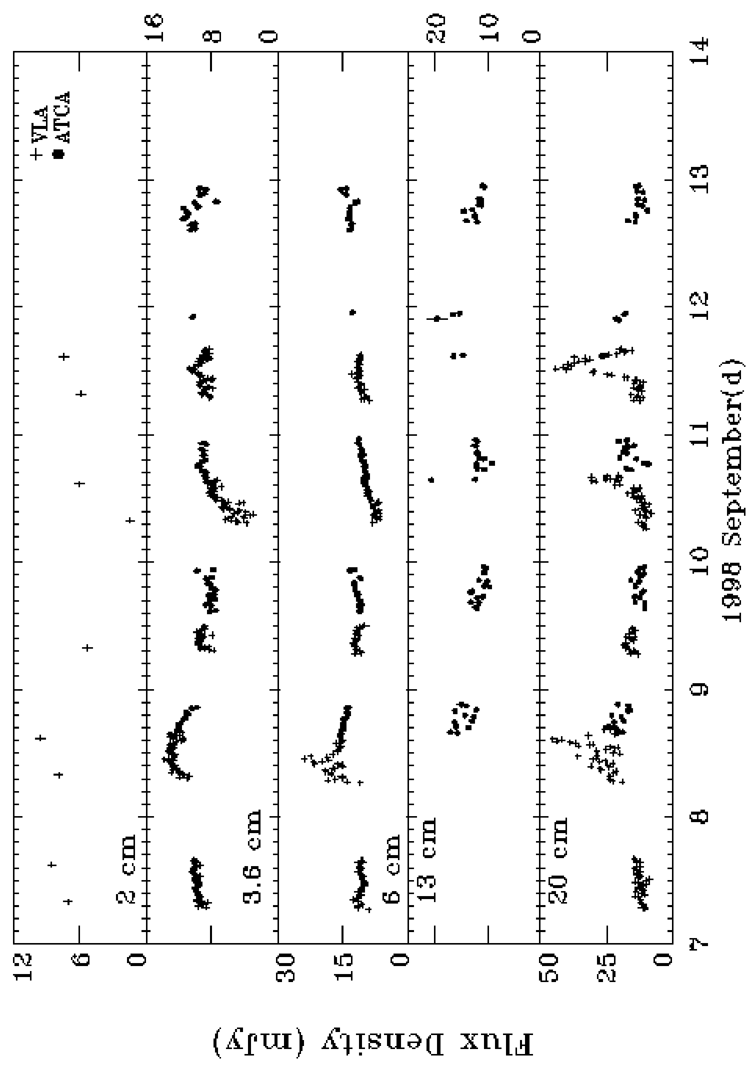

Fig. 4a.— (a) Flux density variations at 2, 3.6, 6, 13, and 20 cm during the 1998 observations. Crosses indicate VLA data; circles denote ATCA observations. Error bars are 1 σ. (b) Variations in percent circular polarization at 2, 3.6, 6, 13, and 20 cm. Symbols are as in Figure 4a. Error bars are 1 σ. Zero percent circular polarization is shown as a dotted line.

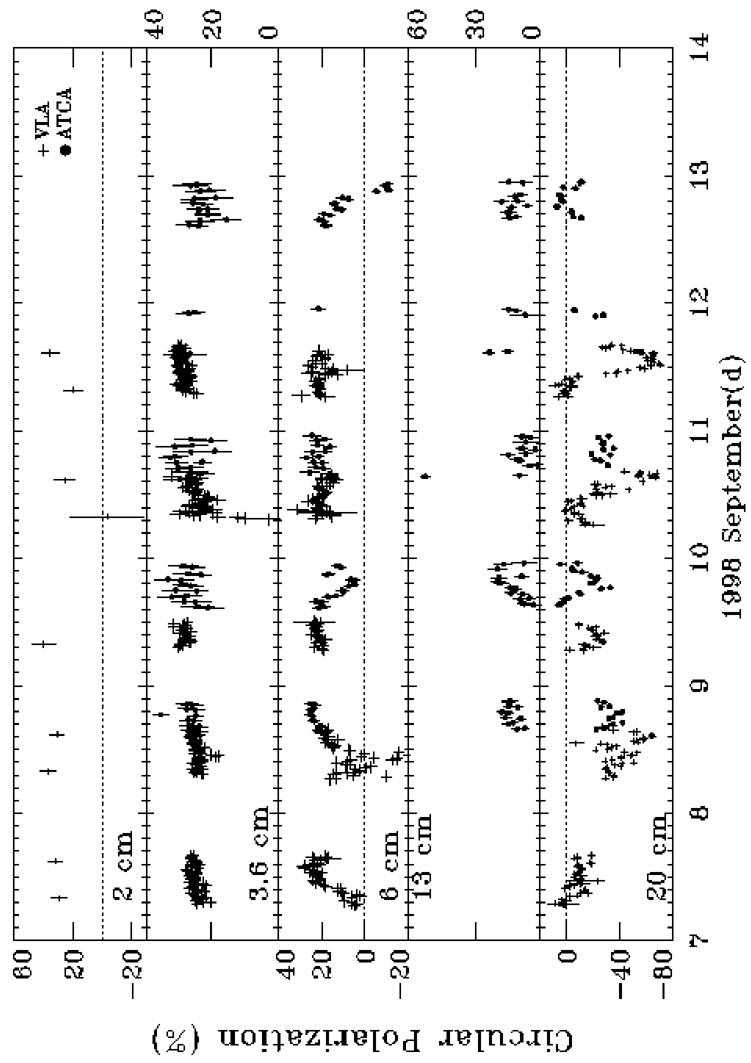
2 cm
3.6 cm
6 cm
13 cm
20 cm
+ VLA
● ATCA
1998 September(d)
Circular Polarization (%)

Fig. 4b.—

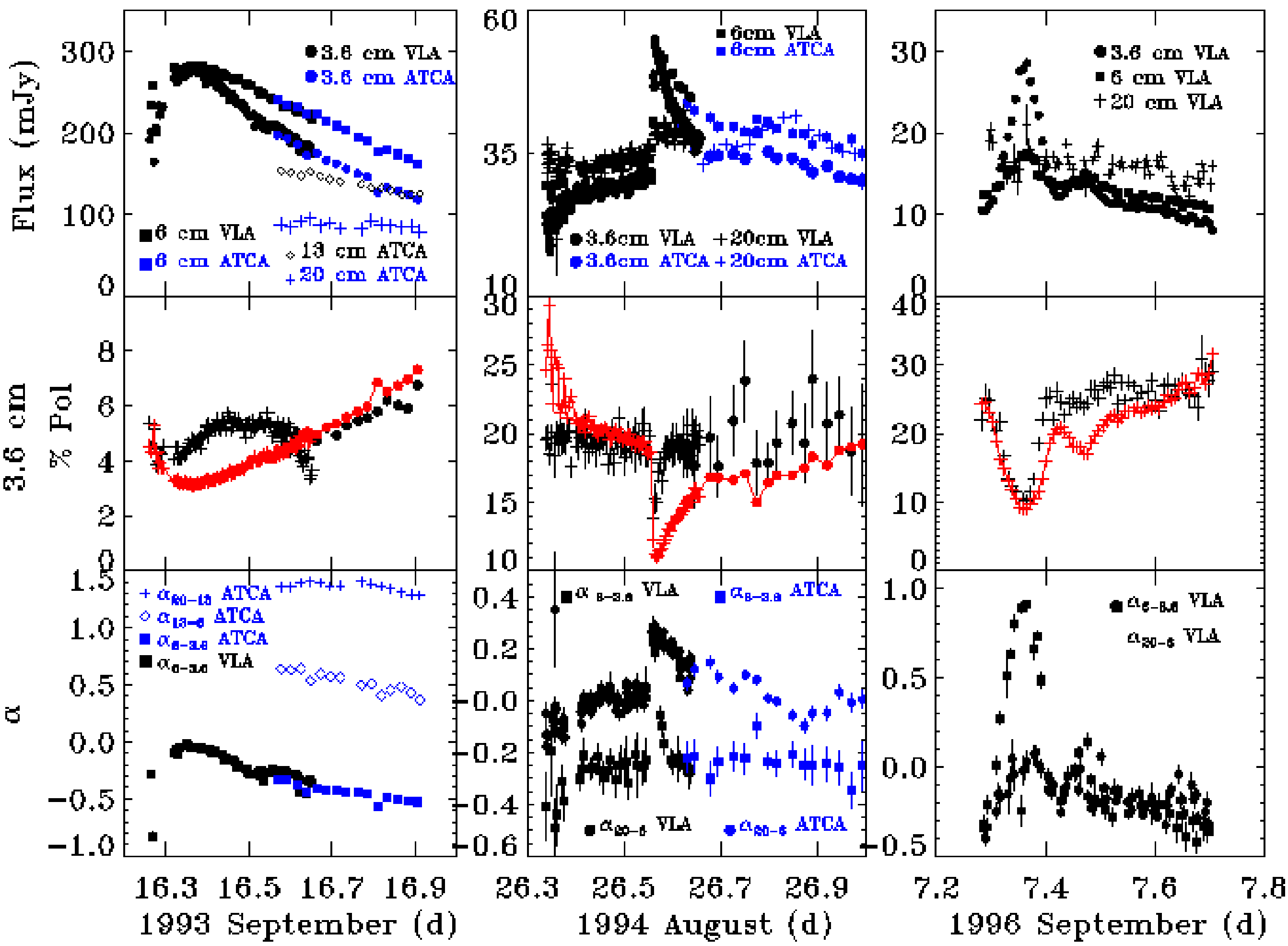

Fig. 5.— Flux, polarization and spectral index variations of three radio flares. **(top row)**: Flux variations at 3.6, and 6 cm; 13 and 20 cm flux variations are plotted where there is coverage. The VLA data has a temporal sampling of 5 minutes, while the ATCA data is binned at ∼ half an hour. **(middle row)**: Observed 3.6 cm circular polarization variations. An increase in flux (as seen in the top row) is accompanied by a marked decrease in percent circular polarization; the polarization minima occur at the flux maximuma for these flares. The red line indicates the polarization variations from a combination of an unpolarized flare and steady, polarized quiescent emission; see text for details. **(bottom row)**: Observed 6–3.6 cm, 13–6, 20–6, and 20–13 spectral indices during the flares. The maximum spectral index is reached at the time of the flare peak flux. The flare spectral indices are consistent with an increase in optical depth during the flare rise.

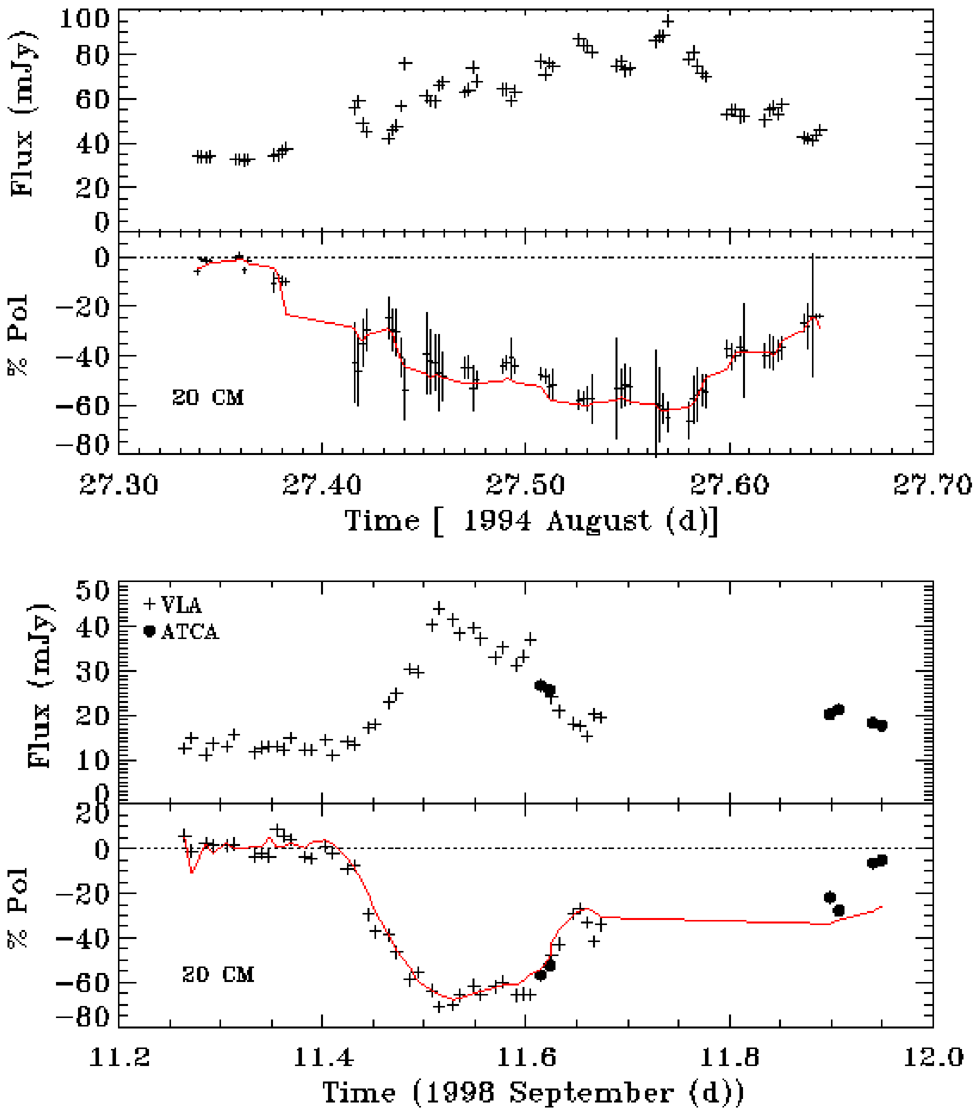

Fig. 6.— Flux and polarization variations of two flares seen at 20 cm in 1994 and 1998. Time bins are 300 seconds in length. Crosses indicate VLA data; circles indicate ATCA data. A noticeable decrease in polarization accompanies increase in flux during a flare, and the polarization increases as the flux declines. Red line indicates the amount of polarization expected if the flare is 100% left circularly polarized; see text for details.

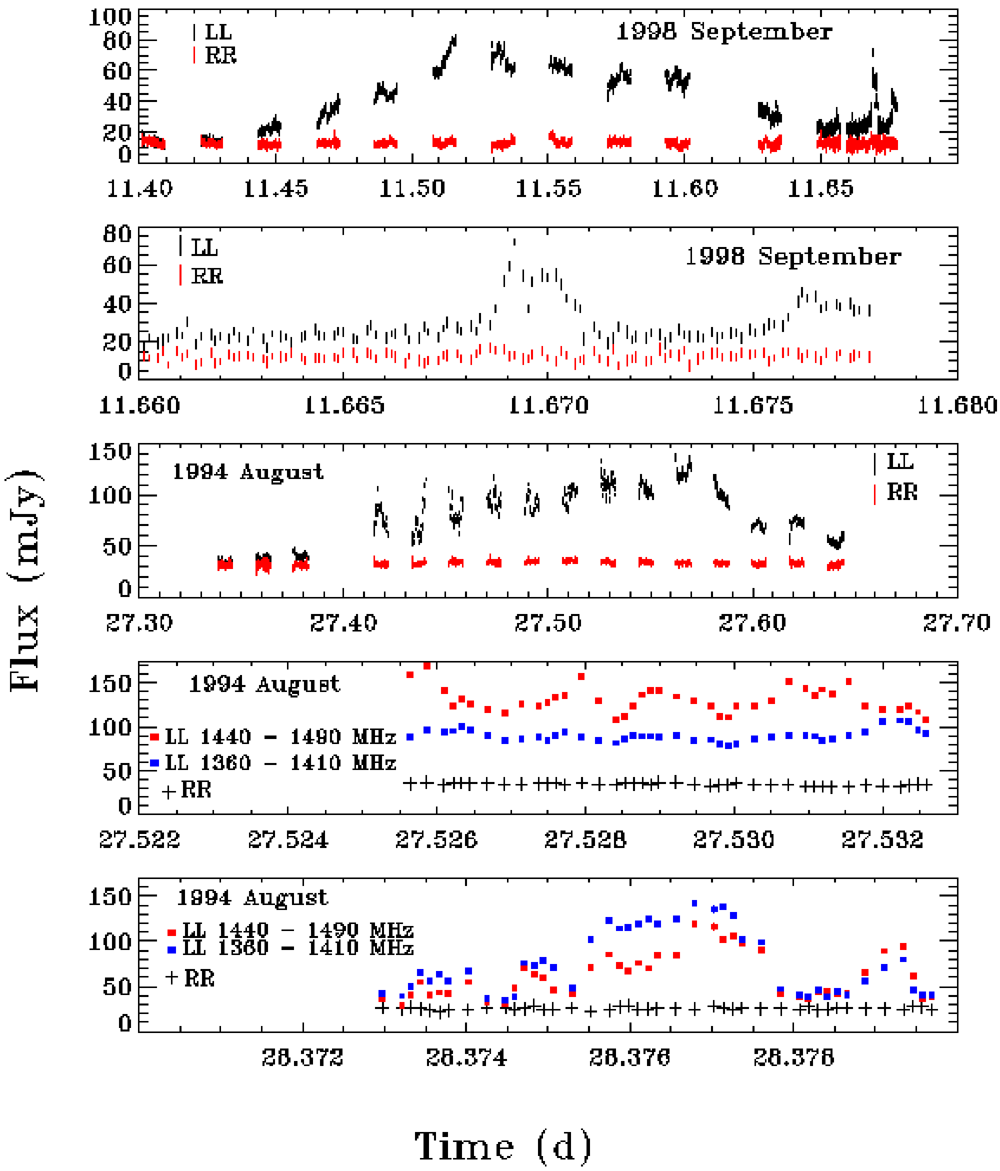

Fig. 7.— Examples of L-band highly polarized emissions (plotted at the maximum time resolution of 10 seconds). Top panel displays LL, RR emission over 5–6 hours in 1998; subsequent panel shows a short duration (≈ 80 seconds) burst. Another example of long time duration, highly polarized fluxes in 1994 is shown. The bottom two panels compare RCP flux with LCP flux in the two frequency bands used in the observation; there is some evidence for different flux density variations at the two bands which comprise the 20 cm continuum observation.

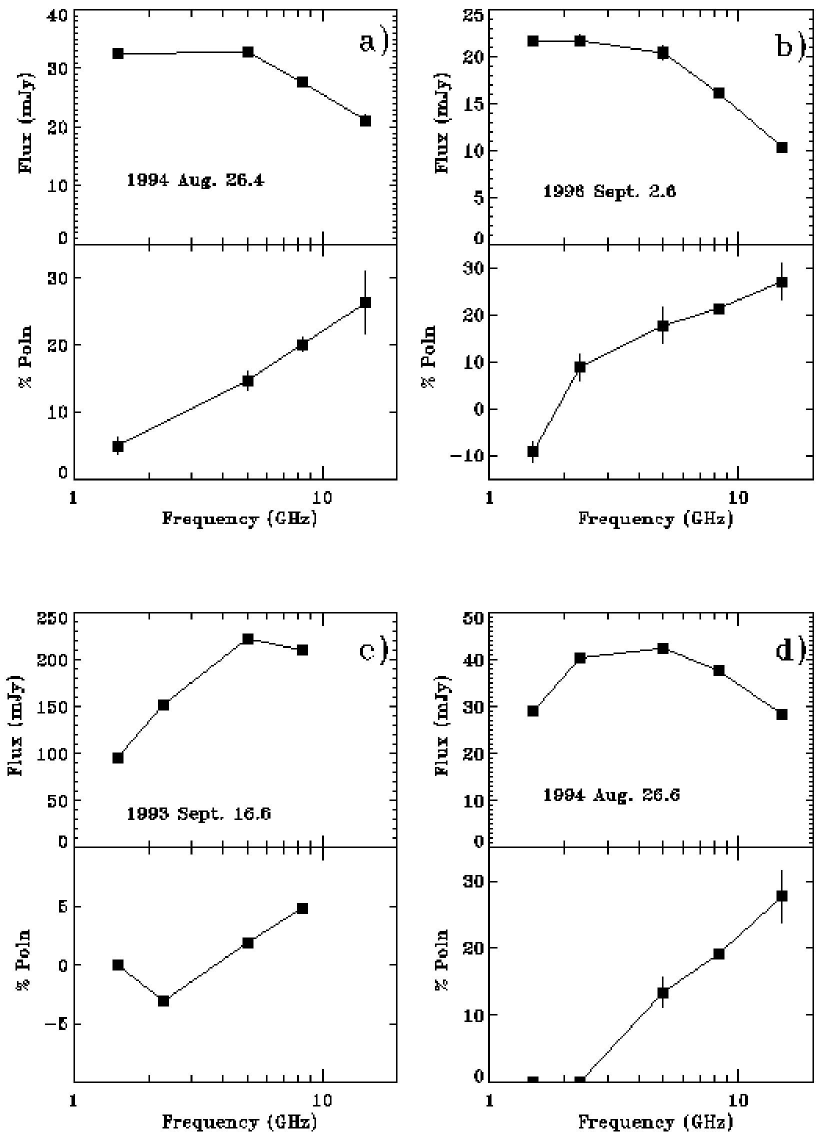

Fig. 8.— Examples of flux and circular polarization spectra for quiescent emission (panels *a* and *b*) and during the peak/decay of gyrosynchrotron flares (panels *c* and *d*) from HR 1099. Spectral indices are listed in Table 5.

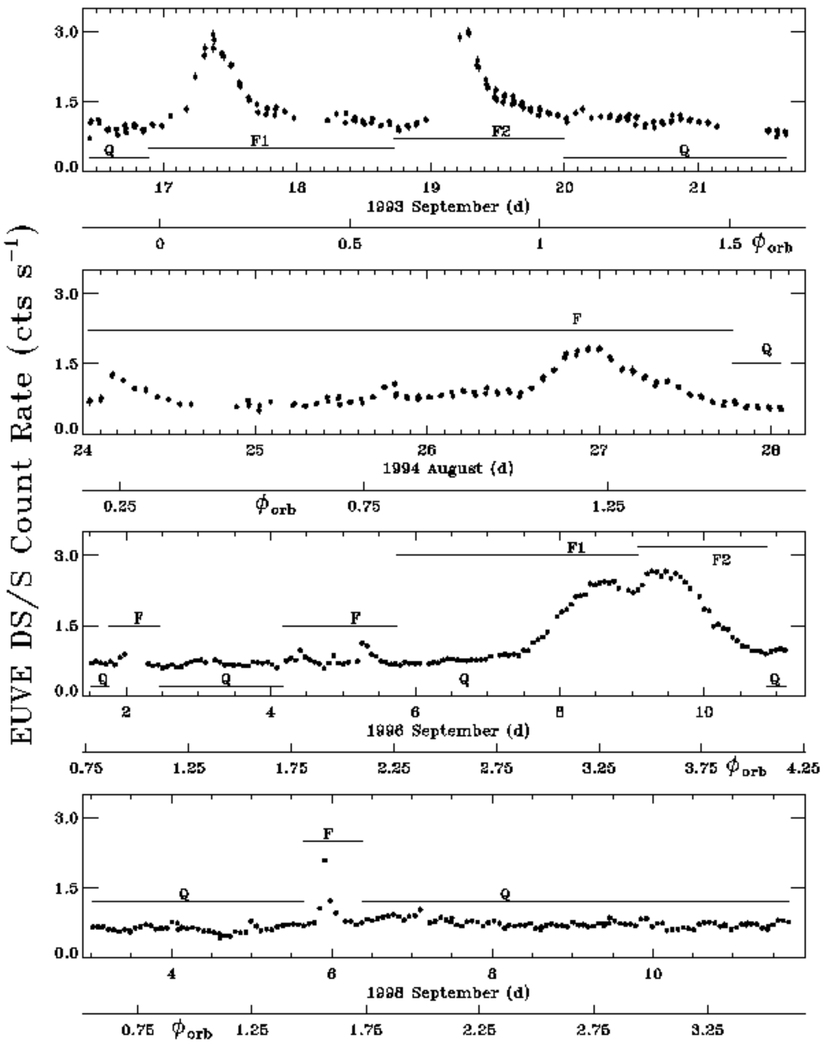

Fig. 9.— Light curves of EUV (80-150 Å) variability as recorded by *EUVE* during 1993, 1994, 1996 and 1998 observations. Binary orbital phase is shown in addition to UT time. Time intervals used for spectral extraction are also noted, and are based on an analysis of light curve variability presented in Section 4.3.1: ‘Q’ refers to quiescent times, ‘F’ to flare times (often several small-amplitude flares), and ‘F1’, ‘F2’, etc. to discrete, large-amplitude flares. Each point represents ≈ 3000 seconds of data, or one point per satellite orbit. Error bars are 1 σ.

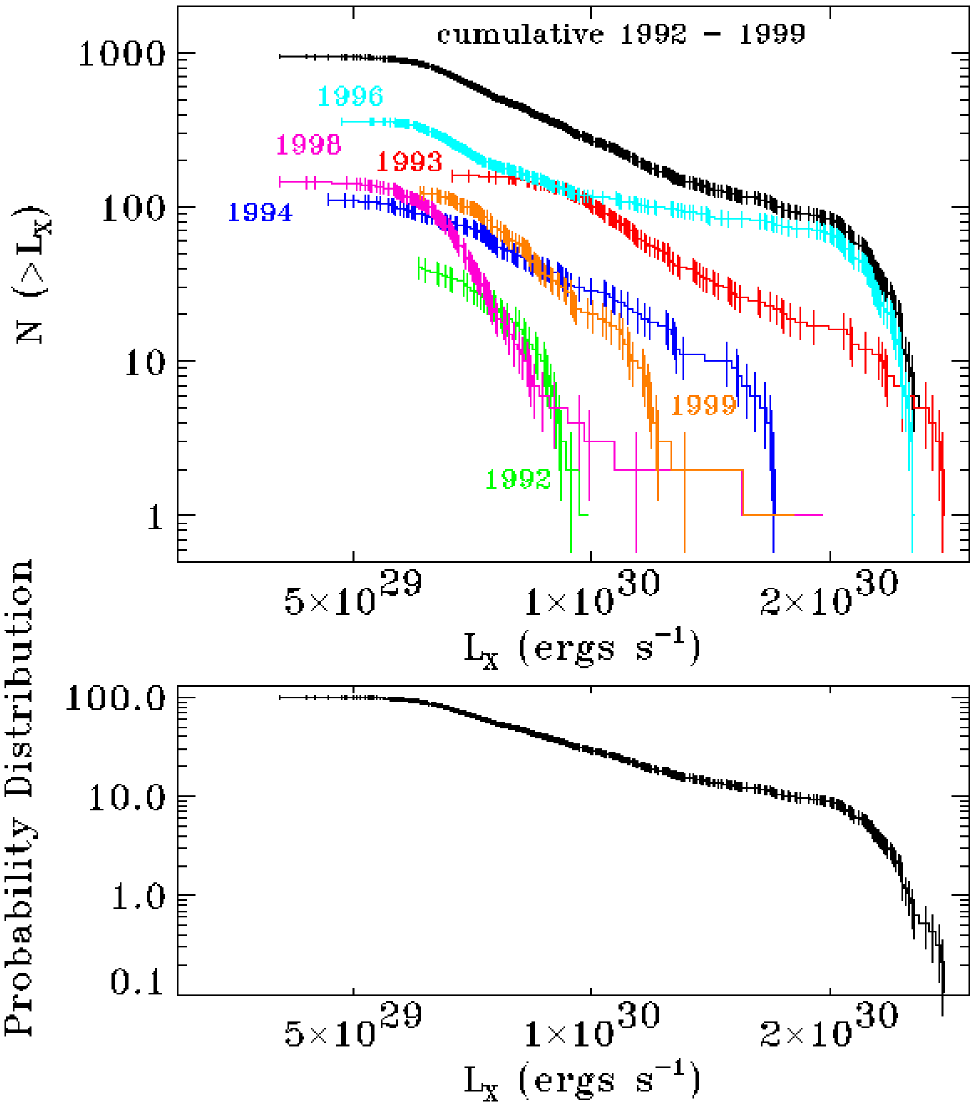

Fig. 10.— **(top)** Cumulative luminosity distributions for the six DS/S observations of HR 1099 from 1992 through 1999. The number of bins with luminosity greater than a given luminosity is plotted, along with the same distribution using all the observations together. **(bottom)** Distribution of light curve events from all DS/S observations of HR 1099, expressed as a percent probability of being larger than a given L_X. There is a flattening at low luminosities and a turnover at high luminosities. The flattening at low luminosities represents the non-flaring luminosities which may be considered "quiescence", while the high luminosity turnover (above 2 10^{30} erg s^{-1}) represents the peaks of the largest flares observed.

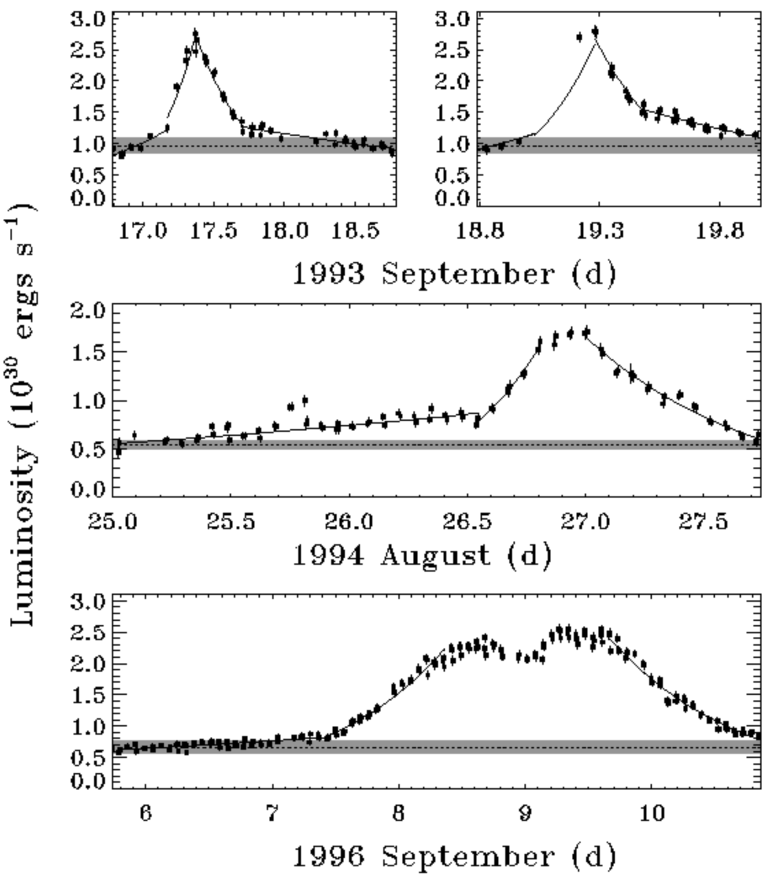

Fig. 11.— Close-up view of four large flares observed with *EUVE*, where the count rate has been converted to luminosity. All four flares seem to show a two-stage rise, an initial slow rise followed by a faster phase. The two flares observed in 1993 September also show evidence for a two-stage decay, with an initial fast period followed by a slower decay. Two large flares occurred in 1996 September too close in time to separate the decay of the first flare from the rise of the second flare.

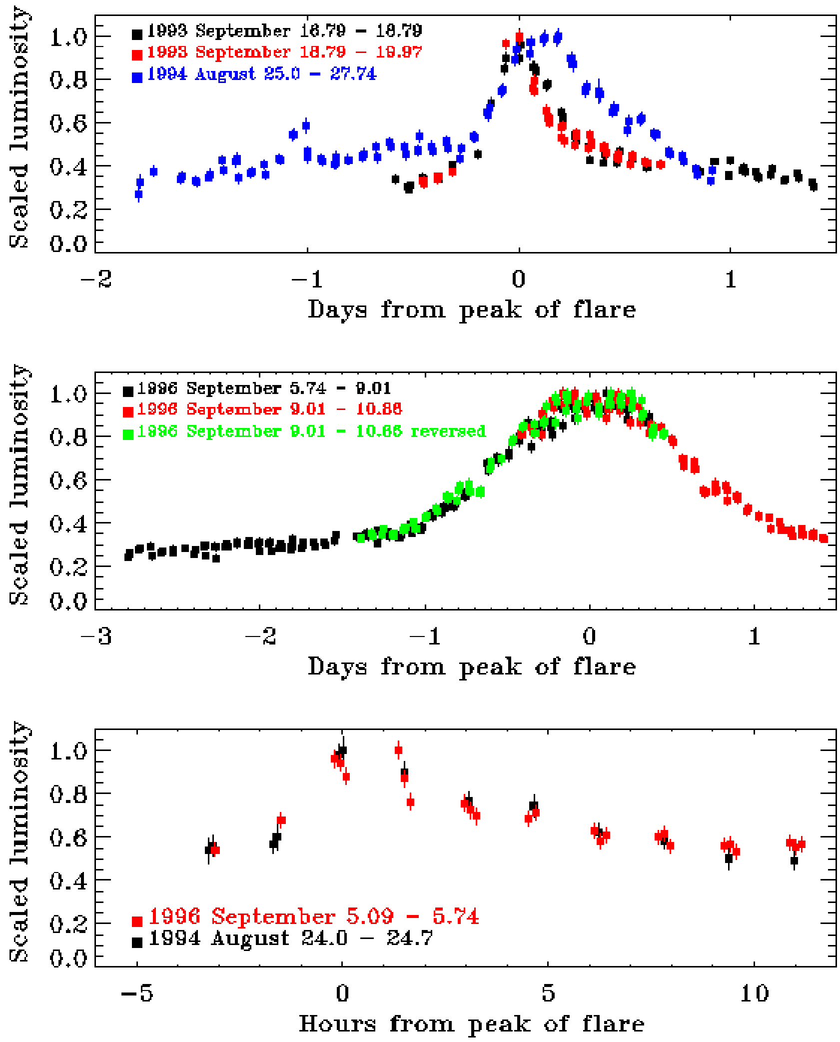

Fig. 12.— **(top)** Flares from 1993 September 16.79 - 18.79 (black), 1993 September 18.79 - 19.97 (red), and 1994 August 25.0 - 27.74 (blue) shifted in time and flux. The two flares in 1993 September are remarkably similar in shape. All three flares seem to show an initial slow rise before the peak of the flare followed by a fast rise. The flare in 1994 August attained a plateau for ≈ 5 hours before decaying again. While the decays of the two flares in 1993 September are very similar, the decay from the 1994 August flare is quite different. **(middle)** Flares from 1996 September 5.74 - 9.01 (black) and 1996 September 9.01 - 10.86 (red), shifted in time and scaled vertically so the peaks overlap. The 1996 September 9.01 - 10.86 flare has also been reflected about the peak to compare the decay of this flare with the rise of the 1996 September 5.74 - 9.01 flare. There is a remarkable amount of symmetry in these two flares. **(bottom)** Flares from 1994 August 24.0–24.7 (black), and 1996 September 5.09–5.74 (red), shifted in time and scaled vertically so the peaks overlap. The flares show a distinct asymmetry, having a fast rise and slow decay that is typical of impulsive solar flares.

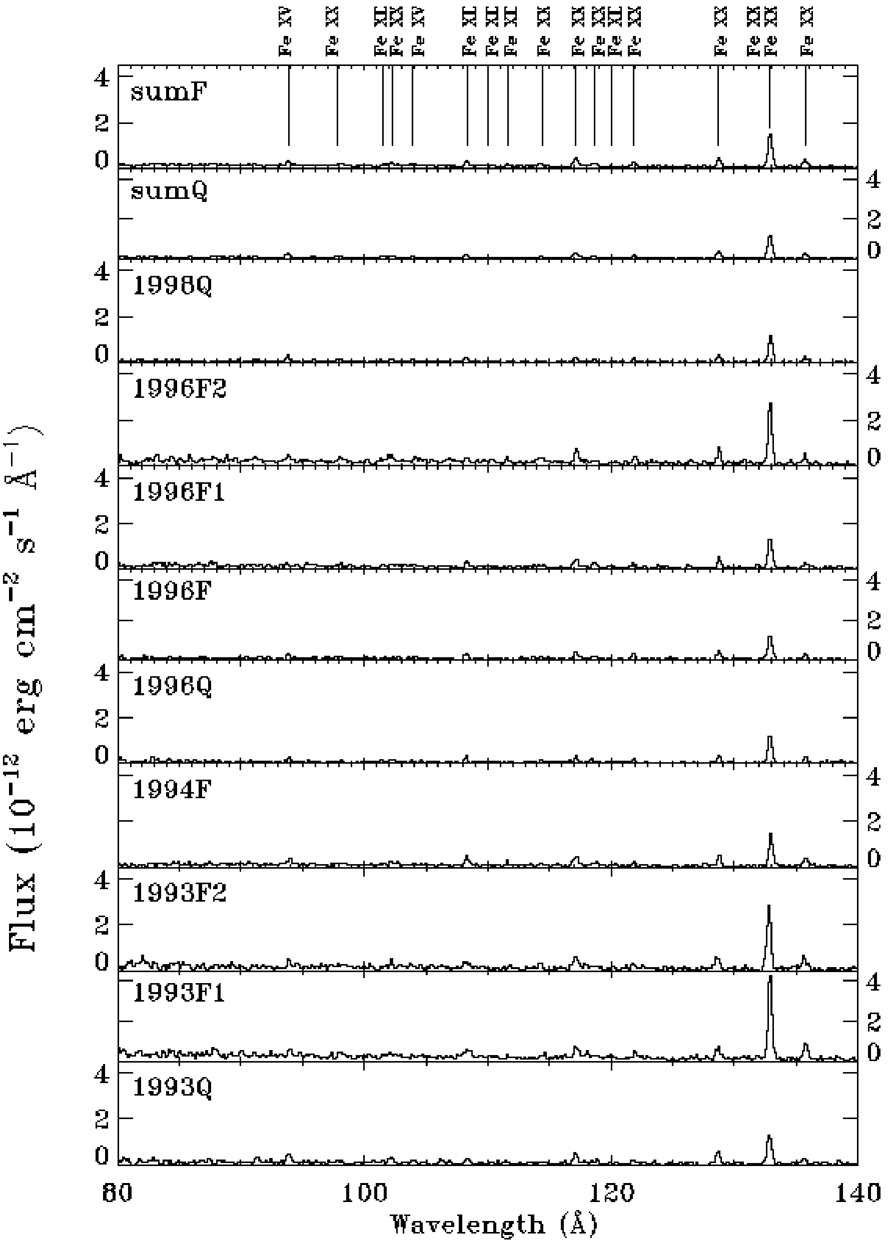

Fig. 13.— *EUVE* SW spectra from all observations. Time intervals are indicated in Figure 9; sumQ and sumF represent the sum of all quiescent and flaring time intervals, respectively.

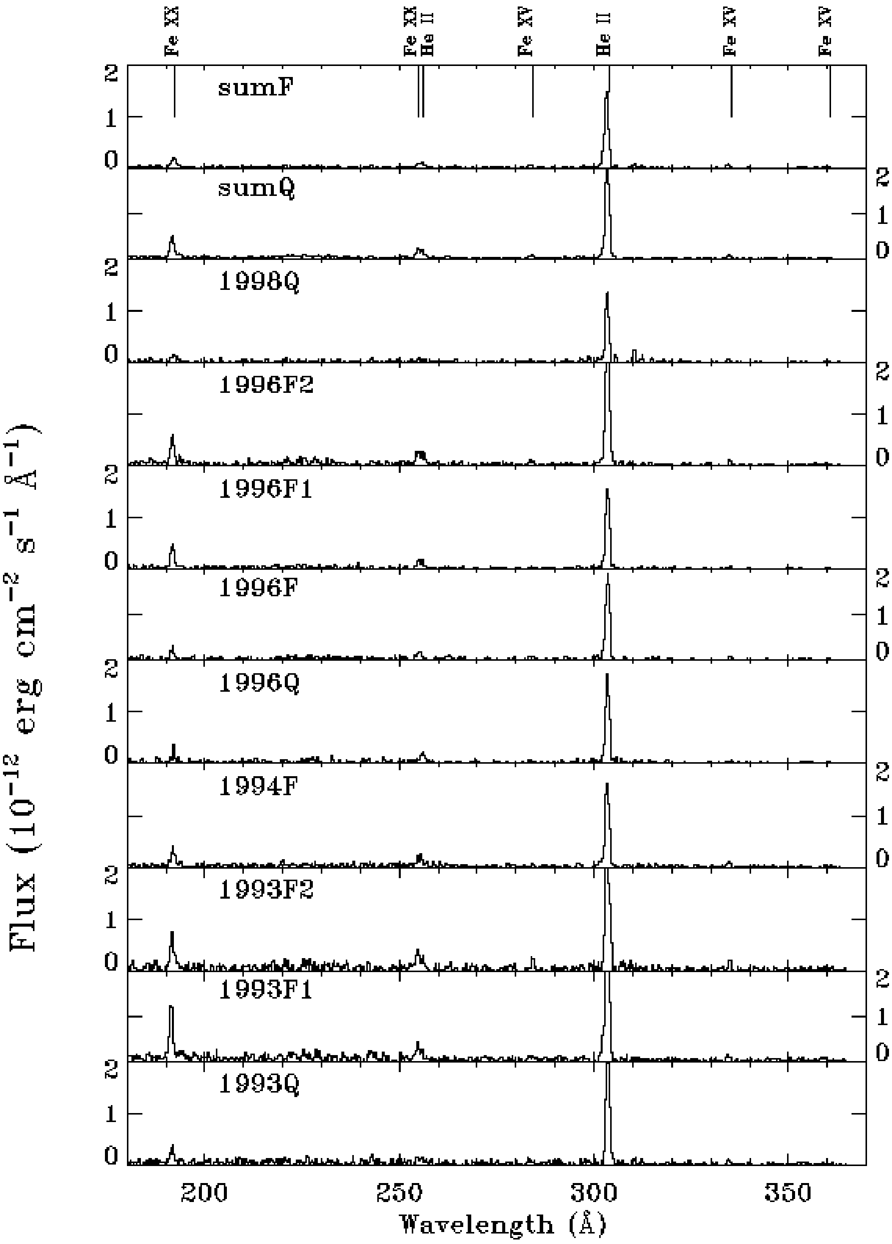

Fig. 14.— *EUVE* MW spectra from all observations. Time intervals are indicated in Figure 9; sumQ and sumF represent the sum of all quiescent and flaring time intervals, respectively.

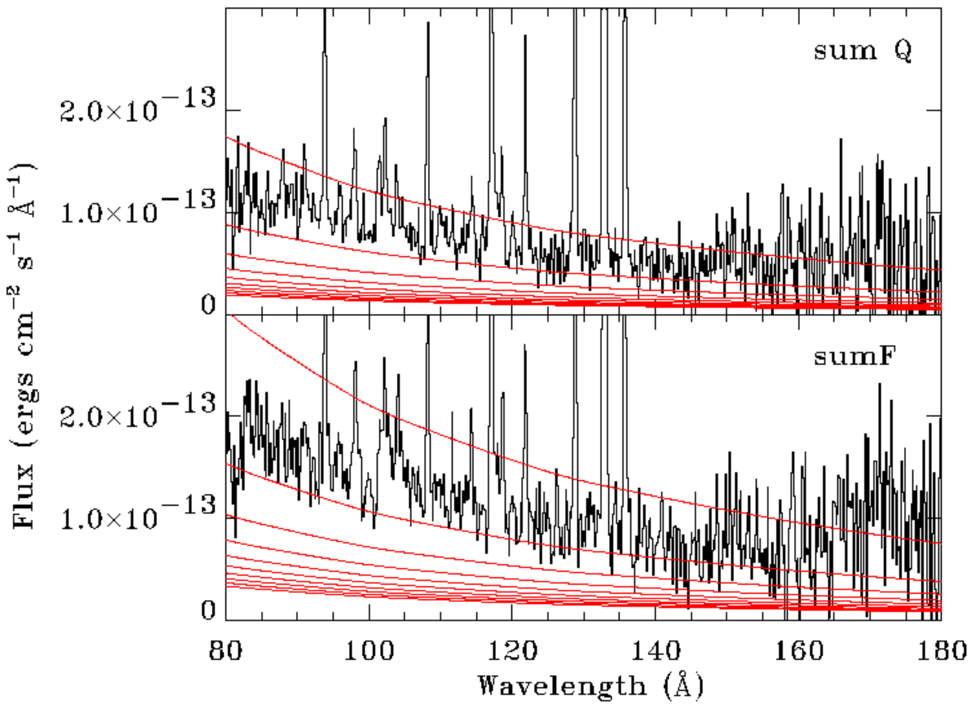

Fig. 15.— EUV composite quiescent and flare SW spectrum of HR 1099. Overlaid in red are continuum spectra calculated assuming different values of the iron to hydrogen ratio, using the differential emission measure distribution determined from each spectrum. From bottom to top, curves decrease from the solar photospheric abundance to one tenth the solar photospheric value in steps of 0.1.

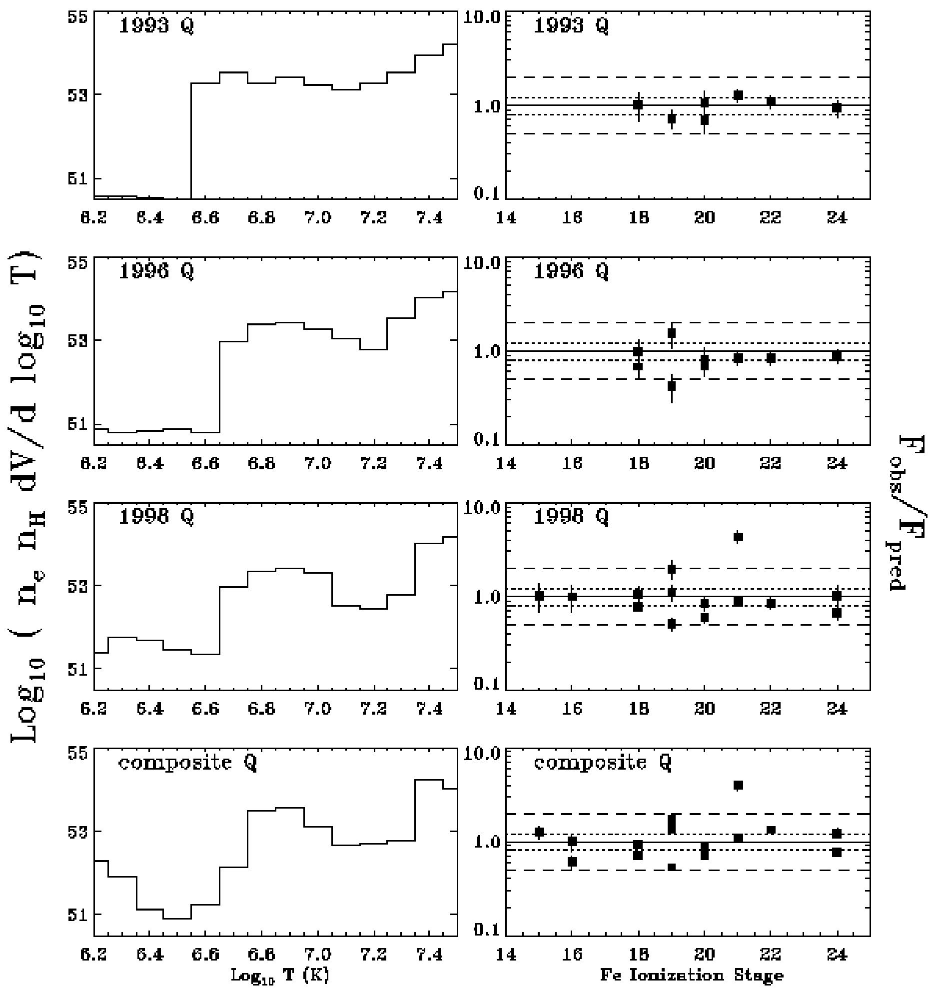

Fig. 16a.— (a) Left panels show DEMs from quiescent *EUVE* data; right panels indicate agreement between observed flux levels and fluxes predicted by the DEM at left. The solid line indicates agreement between observed and predicted fluxes; dashed lines show factor of two agreement and dotted lines, 20%. Time intervals are shown in the upper left corners and correspond to those depicted in Figure 9. (b,c) Same as Figure 16a, for flaring intervals from *EUVE* spectra.

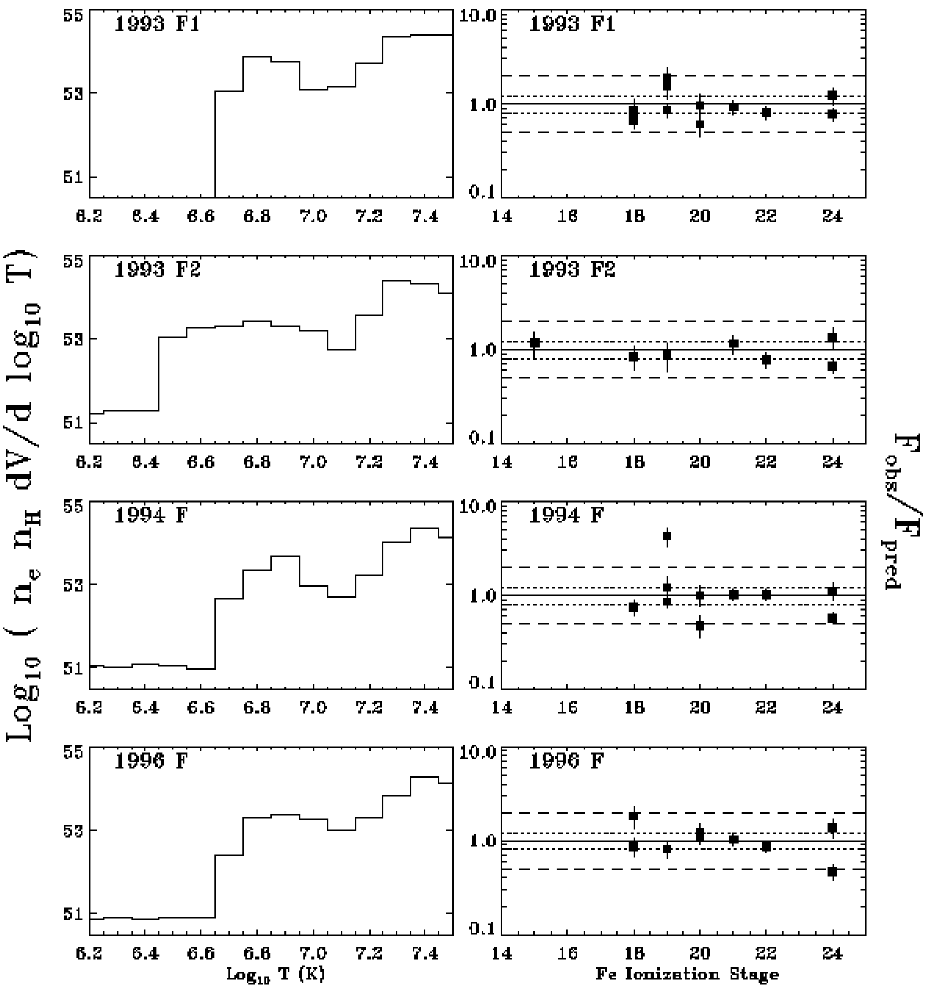
1993 F1
1993 F1
1993 F2
1993 F2
1994 F
1994 F
1996 F
1996 F
Log_{10} (n_e n_H dV/d $\log_{10}$ T)
F_{obs}/F_{pred}
Log_{10} T (K)
Fe Ionization Stage

Fig. 16b.—

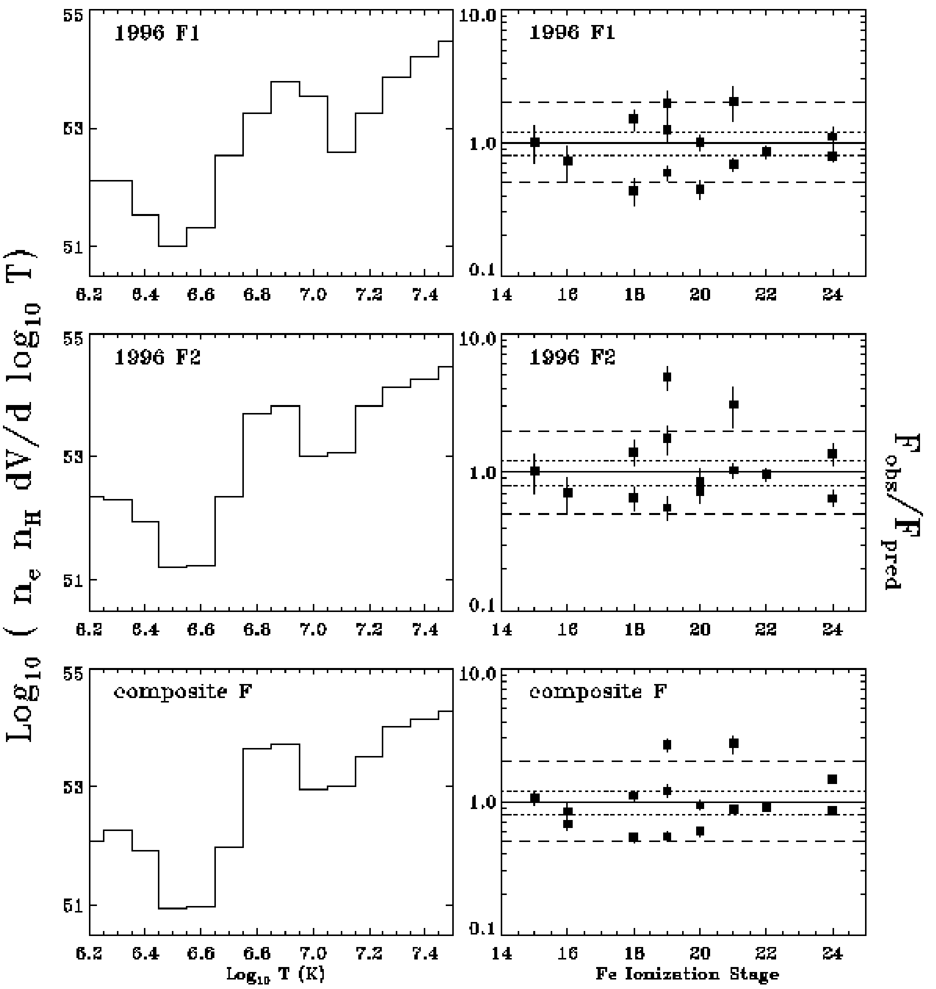
1996 F1
1996 F2
composite F
Log_{10} (n_e n_H dV/d log_{10} T)
F_{obs}/F_{pred}
Log_{10} T (K)
Fe Ionization Stage

Fig. 16c.—

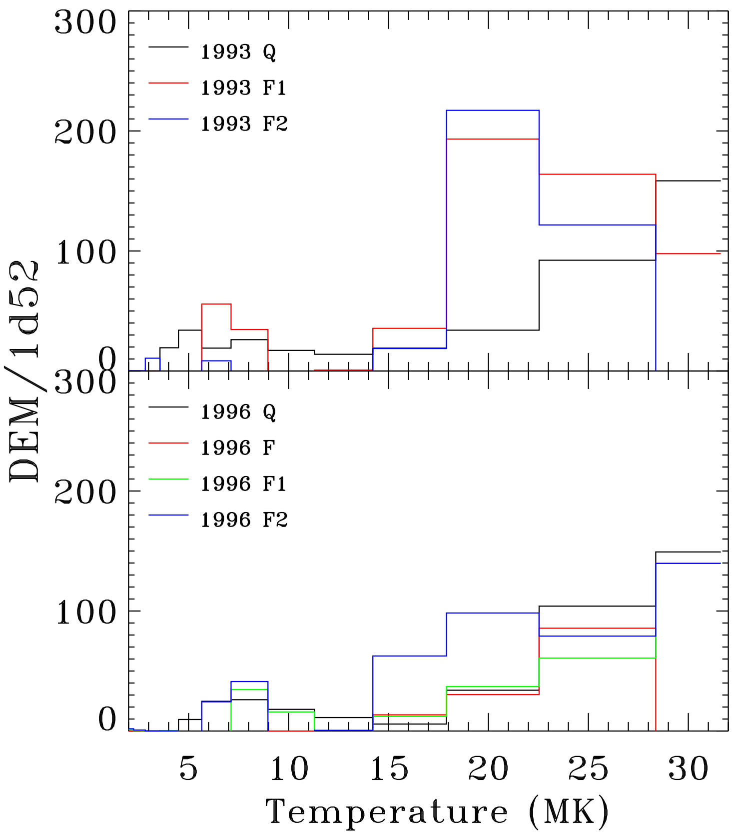

Fig. 17.— Comparison of quiescent and flare DEMs from 1993 and 1996 *EUVE* observations. The flare DEMs have had the quiescent DEM subtracted, to examine the flare contribution to the DEM. This shows up primarily as more plasma at temperatures > 15 MK, and an enhancement at 6–9 MK.

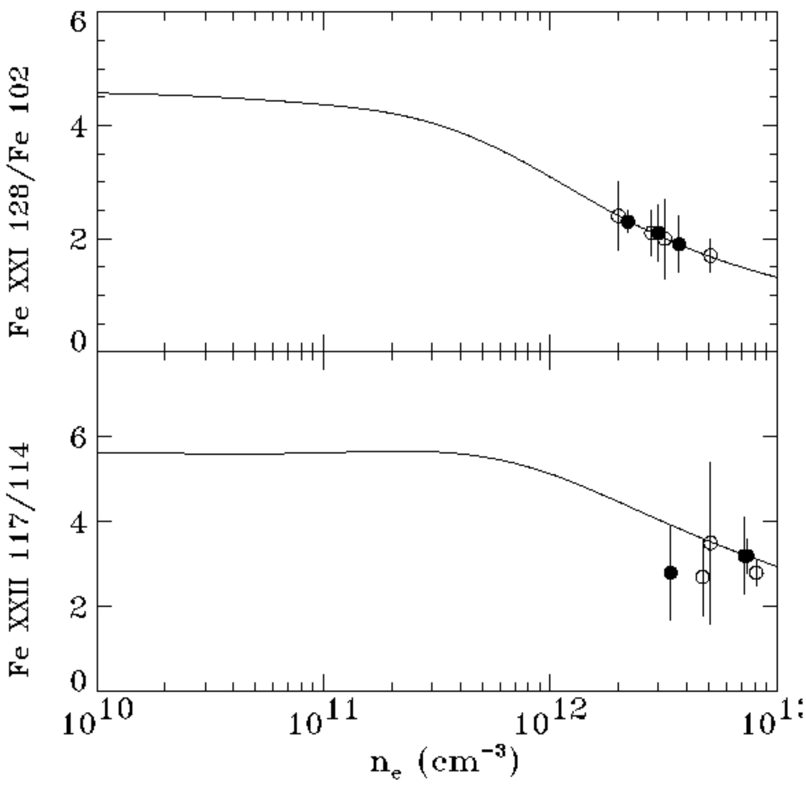

Fig. 18.— Electron densities derived from Fe XXI and Fe XXII energy flux line ratios in *EUVE* spectra of HR 1099. Circles indicate values of the line ratios; error bars correspond to 1 σ uncertainties. Theoretical curves are from Brickhouse et al. (1995). Open circles indicate flare segments; filled circles quiescent intervals. All measurements indicate high electron densities; there is no systematic enhancement of electron densities during flare segments compared to quiescent segments.

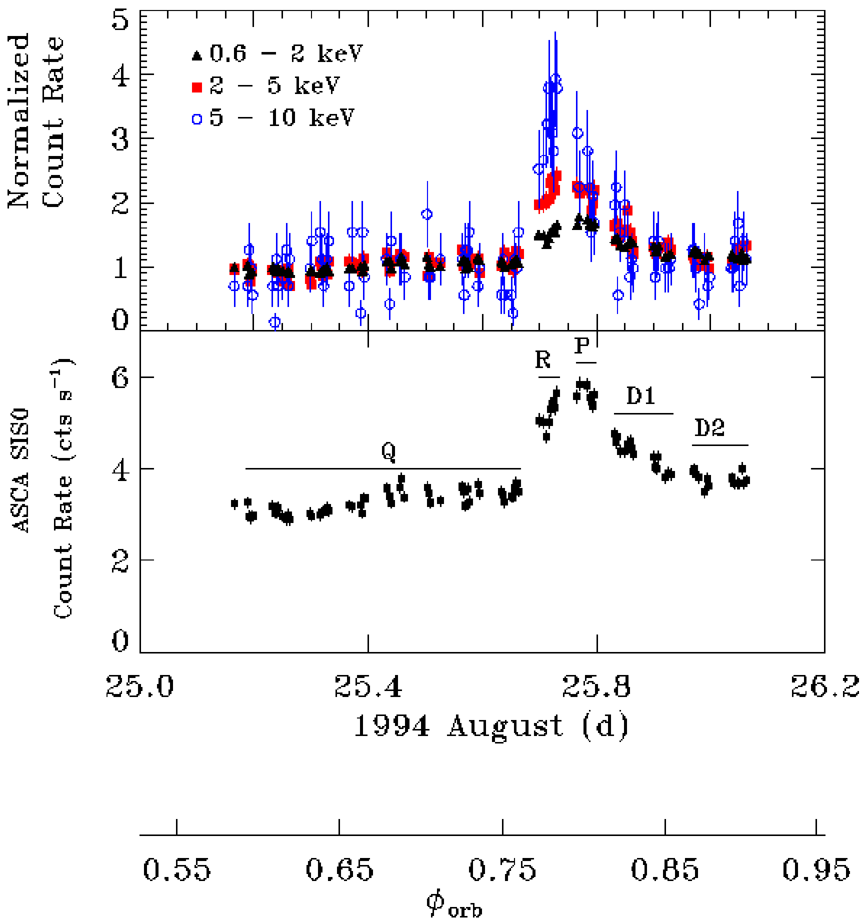

Fig. 19.— **(top)** Time evolution of *ASCA* SIS0 count rates in three different bandpasses, 0.6–2 keV, 2–5 keV, and 5–10 keV, during the observation, normalized to the respective average quiescent count rates in each bandpass. Error bars are 1 σ. There is a trend of increasing enhancement in count rate during the flare with increasing bandpass energy. **(bottom)** *ASCA* SIS0 0.6-10 keV light curve during the 1994 observation. Time intervals used for spectral extraction are indicated; binary orbital phase during the observation is indicated at the bottom. Each point is an average over 256 s; error bars are 1 σ.

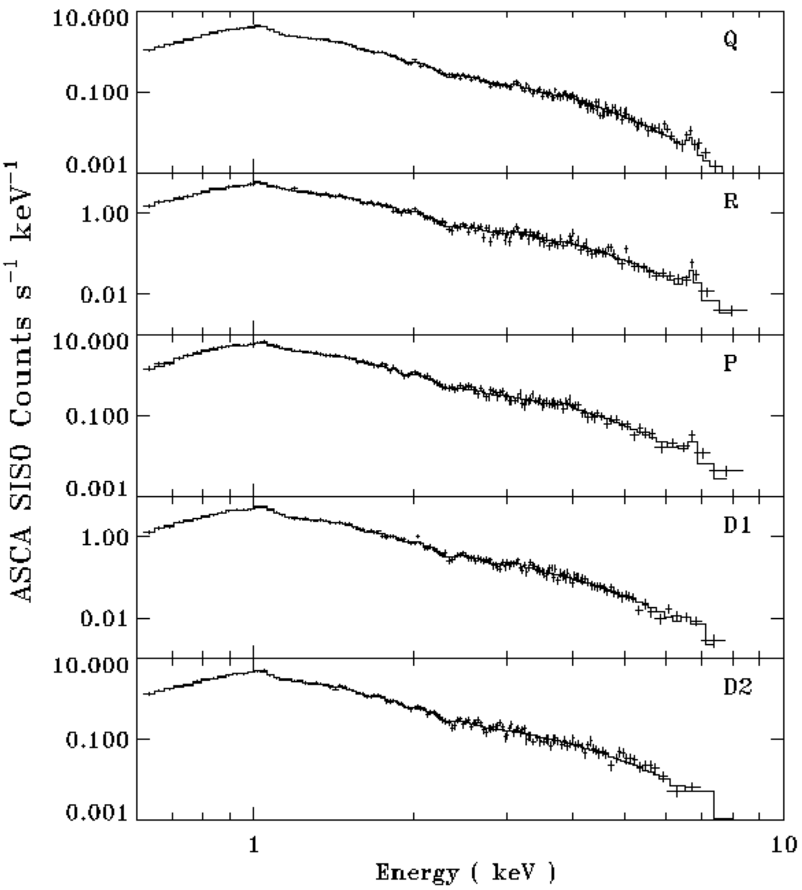

Fig. 20.— Time-resolved *ASCA* SIS0 spectra, along with 2T VMEKAL fits to data. Time intervals **Q**, **R**, **P**, **D1**, and **D2** are indicated in Figure 19. Column density N_H is held fixed at 1.35 10^{18} cm^{-2}; see text for details.

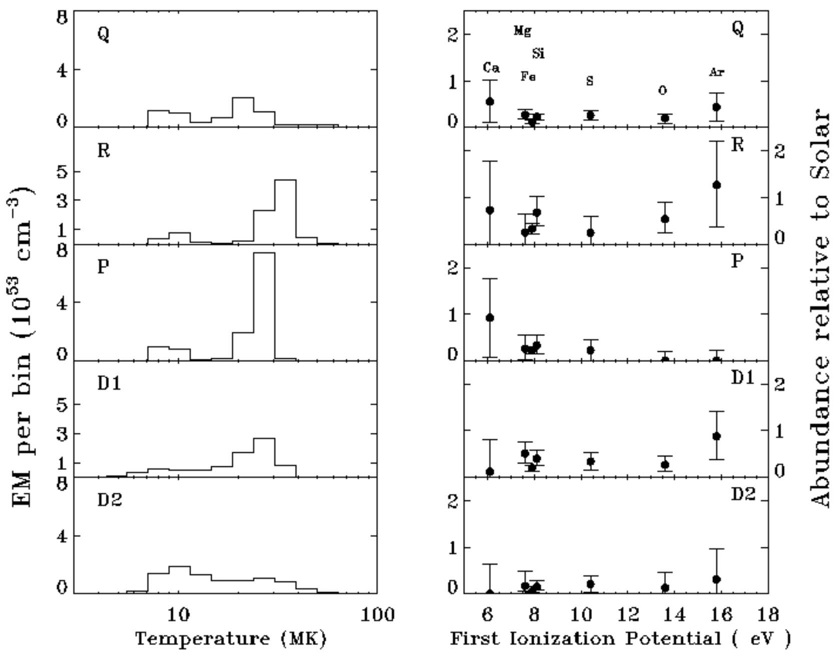

Fig. 21.— **(left)** Variation of the emission measure distribution determined from *ASCA* SIS0+GIS2 spectra over the course of the observation. Chebyshev polynomials of order 8–10 have been used. Abundances from 2T SIS0+GIS2 fits have been used in these fits. Time intervals are indicated in Figure 19. **(right)** Variation in the derived abundances from 2T VMEKAL fits over the course of the observation, plotted against the first ionization potential (FIP). Element identifications are shown in the uppermost panel. Error bars are 90% confidence intervals.

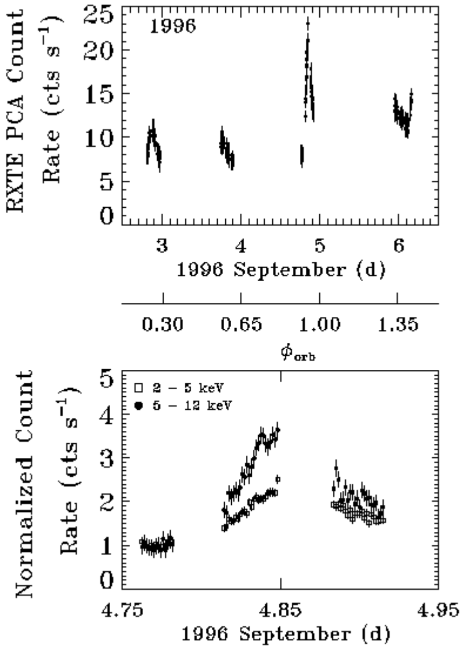

Fig. 22.— **(top)** *RXTE* PCA (2-12 keV) light curves from the 1996 and 1998 observations. The 1996 observation has 128 second bins, while the 1998 observation had 256 second bins. One sigma error bars are also plotted. Binary orbital phase during the observation is also indicated. **(bottom)** Close-up view of two flares in 2-5 keV and 5-12 keV bands. The light curves have been divided by the average count rates in each bandpass outside of the flare, to compare the relative output during the flare in the two bandpasses.

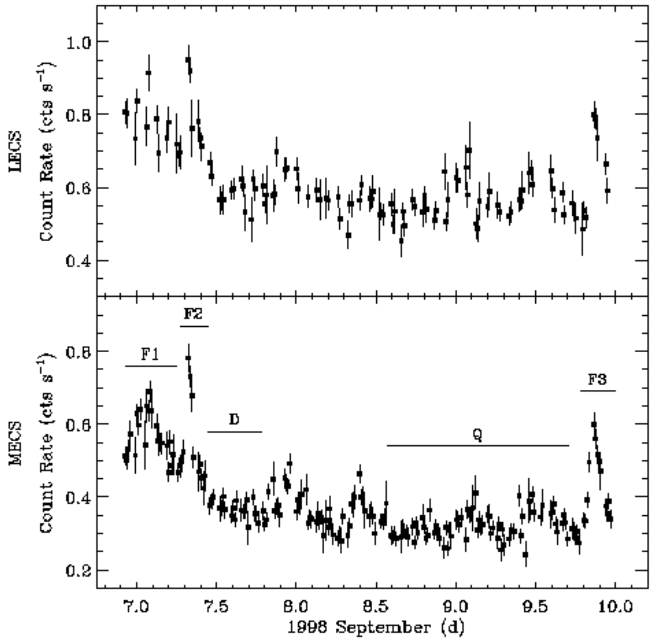

Fig. 23.— *BeppoSAX* LECS (**top**) and MECS (**bottom**) light curves during the 1998 observation. In the bottom panel the time intervals used for spectral extraction are indicated. Data are binned over 900 s; error bars are 1 σ.

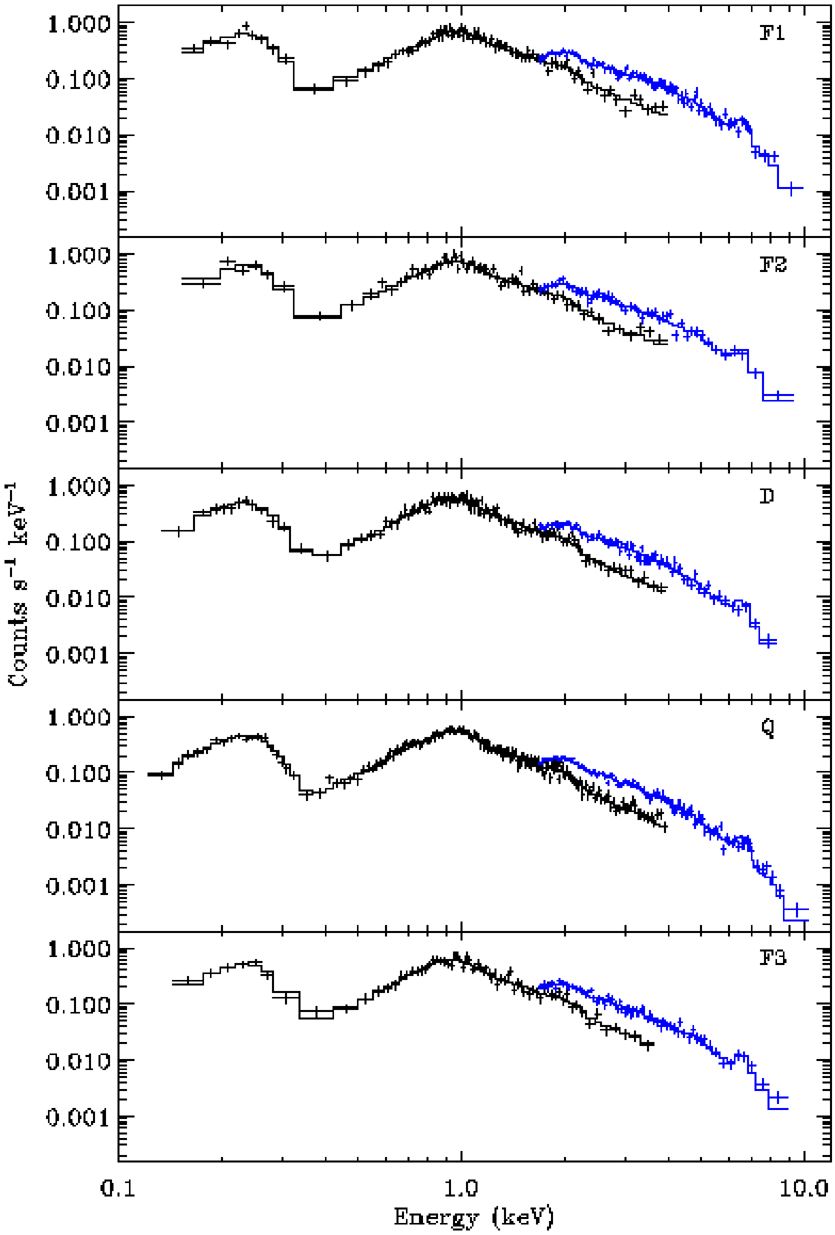

Fig. 24.— Time-resolved *BeppoSAX* spectra, along with 2T MEKAL fits to data. Time intervals **F1**, **F2**, **D**, **Q**, and **F3** are indicated in Figure 23.

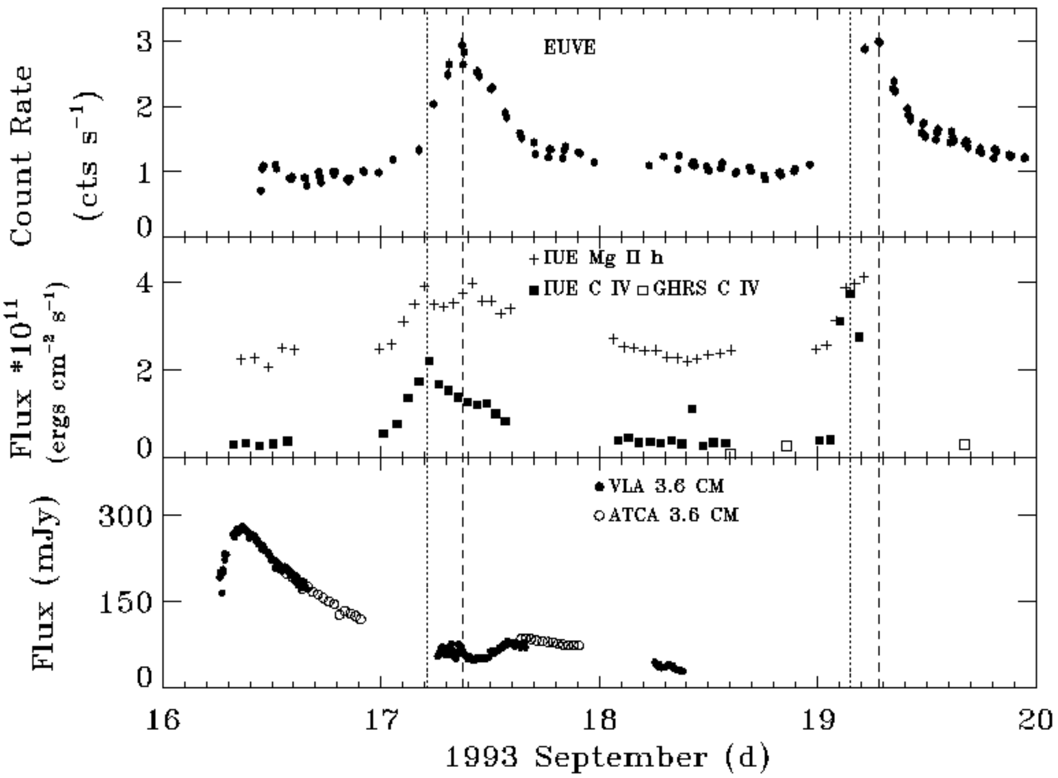

Fig. 25.— Plot of EUV, UV, and radio variations in 1993. Dashed lines indicate approximate times of peaks in the EUV radiation; dotted lines indicate times of maximum C IV emission.

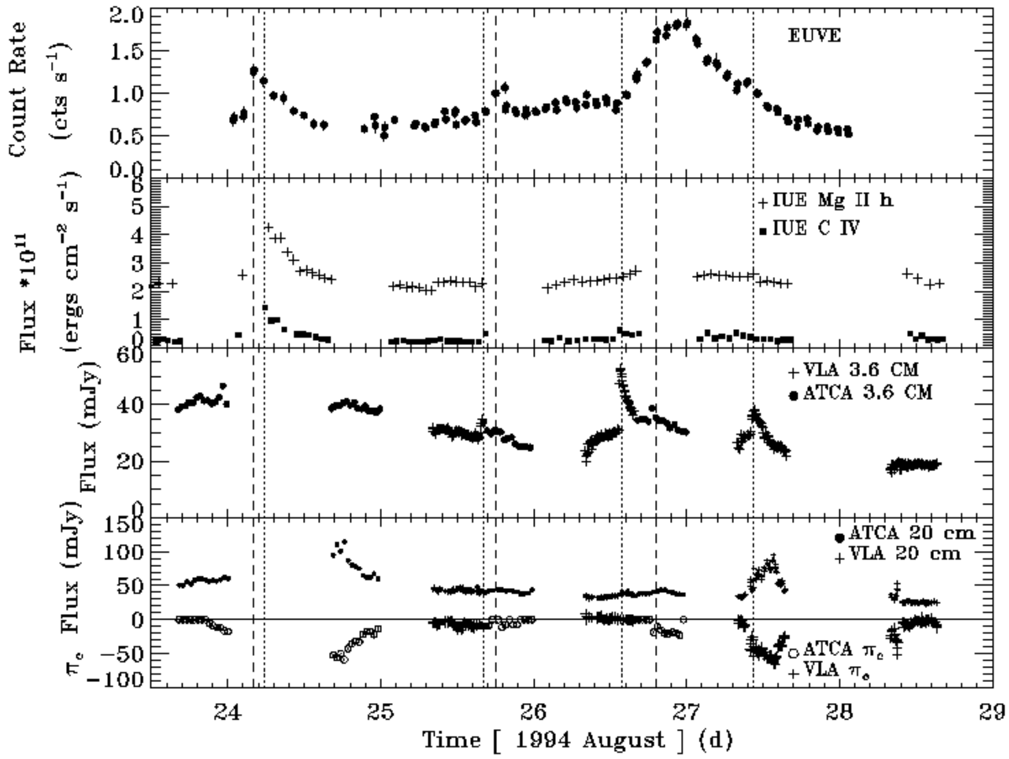

Fig. 26a.— (a) Plot of EUV, UV, and radio variations in 1994 August. Dotted lines indicate times of UV and/or 3.6 cm peaks; dashed lines delineate EUV peak times. (b)Plot of X-ray, EUV, UV, and radio variations over $\approx$ 20 hours on 1994 August 25. Dashed/dotted lines are same as for (a).

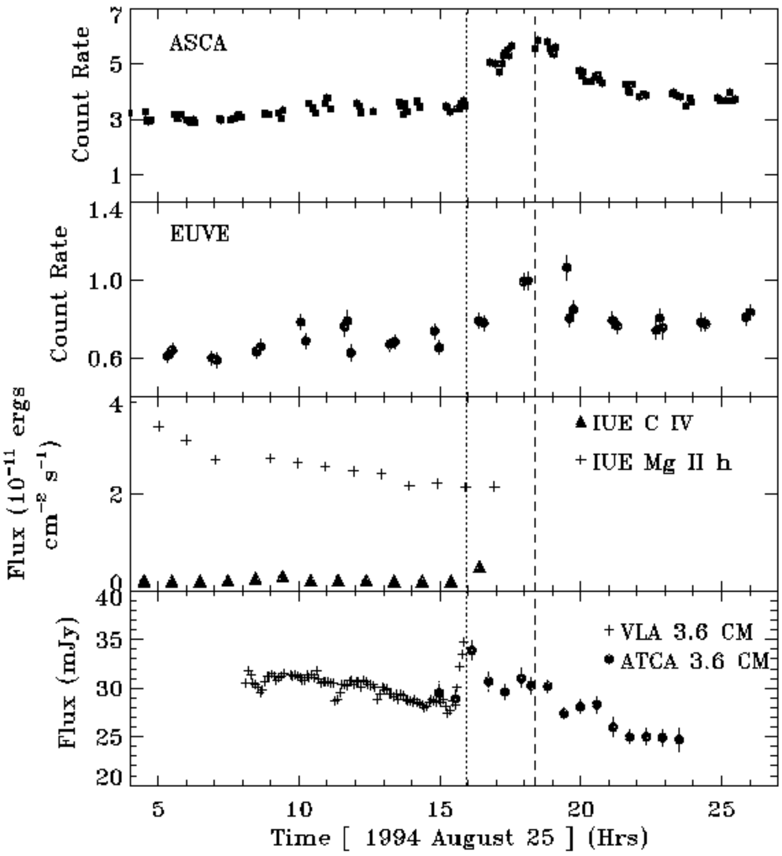
ASCA
Count Rate
EUVE
Count Rate
▲IUE C IV
+IUE Mg II h
Flux (10^{-11} ergs cm^{-2} s^{-1})
+VLA 3.6 CM
● ATCA 3.6 CM
Flux (mJy)
Time [1994 August 25] (Hrs)

Fig. 26b.—

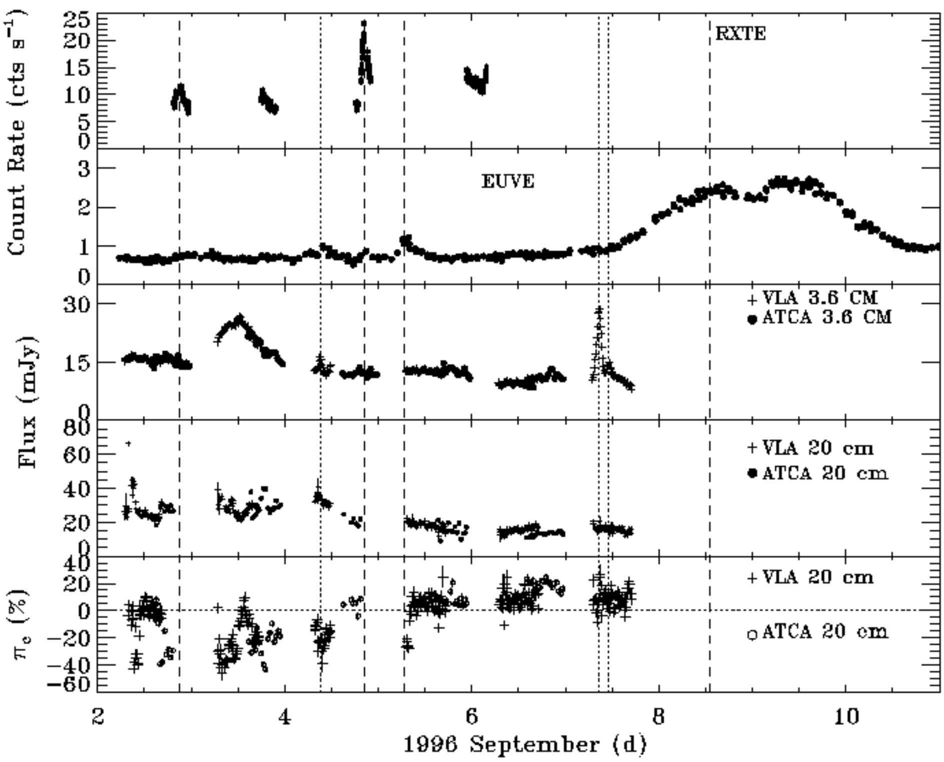

Fig. 27.— Plot of X-ray, EUV, and radio variations in 1996. Dashed lines indicate EUV/SXR peaks; dotted lines indicate radio peaks.

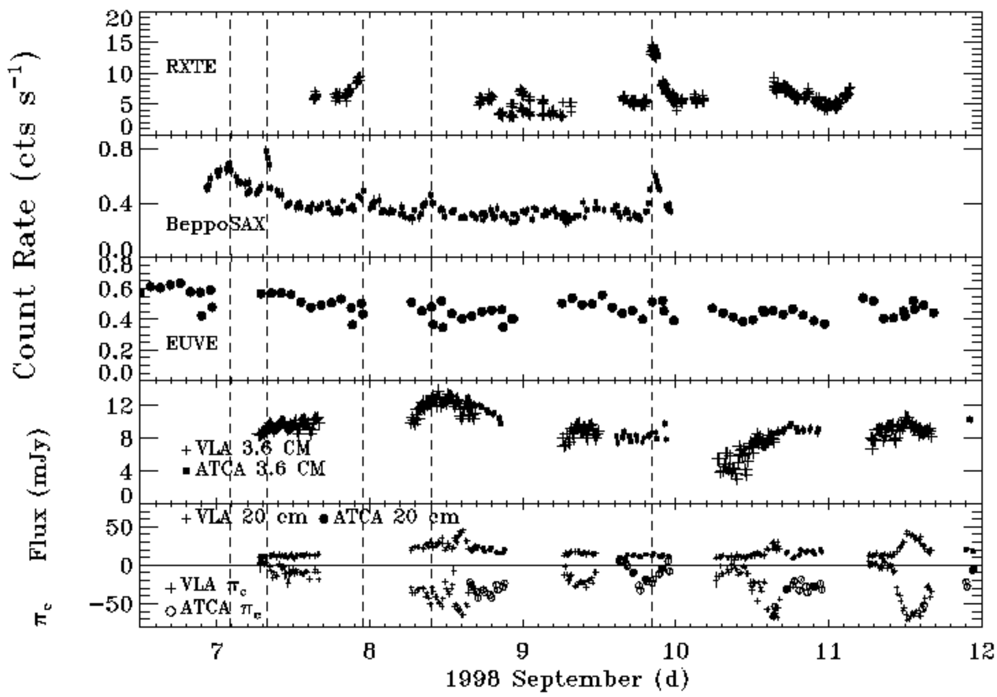

Fig. 28.— X-ray, EUV, and radio variations in 1998. Dashed lines indicate times of EUV/X-ray flare peaks.

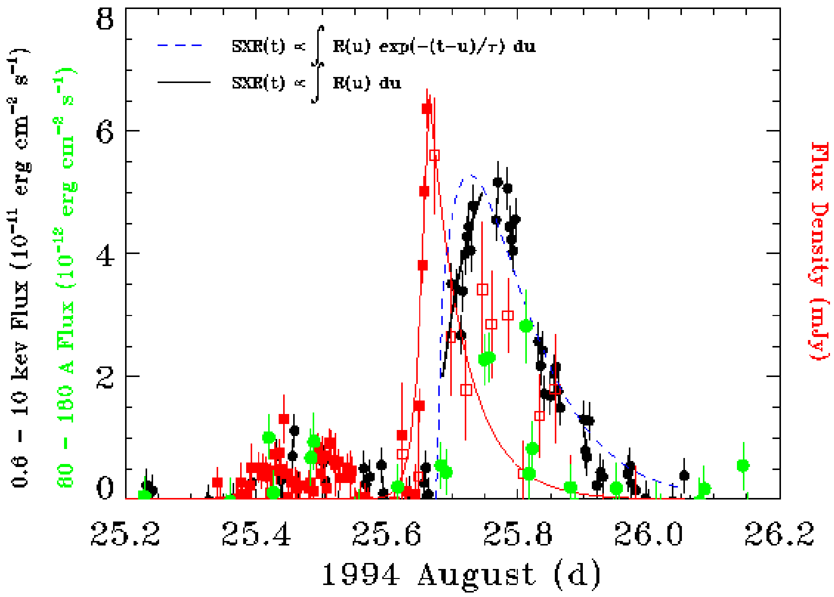

Fig. 29.— Example of the Neupert effect in a flare on HR 1099. Red squares are 3.6 cm radio flare fluxes (filled=VLA data, open=ATCA data), with an estimate of the quiescent emission subtracted; red curve is a fit to the data, using an exponentially decaying time profile. Black circles are *ASCA* 0.6–10 keV flare fluxes, green circles *EUVE* 80–180 Å DS flare fluxes; an estimate of the X-ray/EUV quiescent emission has been subtracted from these. Blue dotted line illustrates the convolution of the radio profile with an exponential function; τ is the radiative decay timescale, set to 6000 seconds, and appropriate for plasma at T$\sim 10^7$K, $n_e \sim 10^{11}$ cm^{-3}. This is the expected temporal trend of the luminosity of the thermal plasma responding to energy deposition as represented by the radio profile. The black curve shows the expected increase in luminosity if the radiative timescale becomes infinite; this approximation is only applicable to the rise phase of the X-ray flare.